AD-A245 203
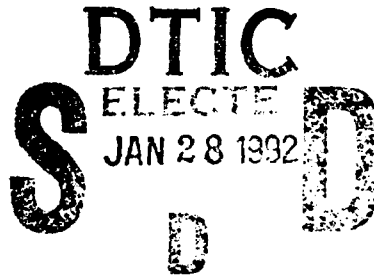
Development of the Next-Generation Electric Field (ELF II) Analysis Codes

Angel E. Rodriguez, et al.
Tetra Corporation
3701 Hawkins N.E.
Albuquerque, NM 87109

DTIC
ELECTE
JAN 28 1992
D
D

January 1992

Technical Report

92 1 27 009

92-02084

DISTRIBUTION LIST UPDATE

This mailer is provided to enable DNA to maintain current distribution lists for reports. We would appreciate your providing the requested information.

☐ Add the individual listed to your distribution list.

☐ Delete the cited organization/individual.

☐ Change of address.

> **NOTE:**
> Please return the mailing label from the document so that any additions, changes, corrections or deletions can be made more easily.

NAME: _____

ORGANIZATION: _____

OLD ADDRESS	**CURRENT ADDRESS**
_____	_____
_____	_____
_____	_____

TELEPHONE NUMBER: ( ) _____

SUBJECT AREA(s) OF INTEREST:

_____	_____
_____	_____
_____	_____

DNA OR OTHER GOVERNMENT CONTRACT NUMBER: _____

CERTIFICATION OF NEED-TO-KNOW BY GOVERNMENT SPONSOR (if other than DNA):

SPONSORING ORGANIZATION: _____

CONTRACTING OFFICER OR REPRESENTATIVE: _____

SIGNATURE: _____

CUT HERE AND RETURN

Director
Defense Nuclear Agency
ATTN: TITL
Washington, DC 20305-1000

REPORT DOCUMENTATION PAGE

1. AGENCY USE ONLY (Leave blank)	2. REPORT DATE	3. REPORT TYPE AND DATES COVERED
	920101	Technical 890920 –910921

4. TITLE AND SUBTITLE

Development of the Next-Generation Electric Field (ELF II) Analysis Codes

6. AUTHOR(S)

Angel E. Rodriguez and Kenell J. Touryan (Tetra Corp)
Patrick J. Roache and Kambiz Salari (Ecodynamics)

5. FUNDING NUMBERS

C   - DNA 001-89-C-0009
PE - 62715H
PR - SF
TA - SB
WU - DH053870

7. PERFORMING ORGANIZATION NAME(S) AND ADDRESS(ES)

Tetra Corporation
3701 Hawkins N.E.
Albuquerque, NM 87109

8. PERFORMING ORGANIZATION REPORT NUMBER

TR-91-014

9. SPONSORING/MONITORING AGENCY NAME(S) AND ADDRESS(ES)

Defense Nuclear Agency
6801 Telegraph Road
Alexandria, VA 22310-3398
RAEV/Beatty

10. SPONSORING/MONITORING AGENCY REPORT NUMBER

DNA-TR-91-145

11. SUPPLEMENTARY NOTES

12a. DISTRIBUTION/AVAILABILITY STATEMENT

Approved for public release; distribution is unlimited.

12b. DISTRIBUTION CODE

13. ABSTRACT *(Maximum 200 words)*

The ELF II program extended the Phase I codes to handle problems encountered in space pulsed power systems design, and applied the resulting next-generation ELF2 codes to numerically analyze electrical stresses which could initiate potential breakdown mechanisms in critical subsystems in a specific real application of interest to SDI. The ELF codes are uniquely suited to electric field analysis in the presence of arbitrarily-shaped conductors and non-homogeneous, nonlinear and time-dependent plasmas because of their unique boundary-fitted grid generation approach and their efficient finite-difference methods.

The chosen paradigm problem was the Space Power Experiments Aboard Rockets III (SPEAR III) payload. The challenges lead to a new grid generator which conserves boundary mode stretching and a new topological flexibility based on grid cut-outs. This report describes the approaches used and new capabilities developed, including user instructions.

14. SUBJECT TERMS

Electric Field Analysis Code   Boundary-Fitted Coordinate System
Finite-Differences   Computational Grid Generation

15. NUMBER OF PAGES

118

16. PRICE CODE

17. SECURITY CLASSIFICATION OF REPORT	18. SECURITY CLASSIFICATION OF THIS PAGE	19. SECURITY CLASSIFICATION OF ABSTRACT	20. LIMITATION OF ABSTRACT
UNCLASSIFIED	UNCLASSIFIED	UNCLASSIFIED	SAR

CLASSIFIED BY:

N/A since Unclassified.

DECLASSIFY ON:

N/A since Unclassified.

DTIC
COPY
INSPECTED
2

Accesion For	
NTIS CRA&I	✓
DTIC TAB	☐
U:announced	☐
Justification	
By	
Distribution/	
Availability Codes	
Dist	Avail and/or Special
A-1	

EXECUTIVE SUMMARY

Many system concepts being considered for the Strategic Defense Initiative (SDI) involve the use of pulsed power and high voltages. A significant problem which needs to be solved in developing operational spacecraft power systems is the management of electric fields within the spacecraft, the primary power supply and conditioning equipment, and the pulsed power system. The space plasma environment is hostile to high voltages because charged particles accelerated by the fields unimpeded by collisions will impinge on solid body surfaces, emitting other charged particles which are subsequently accelerated, leading to breakdown. The Electric Field Analysis Phase II (ELF2) program, described in this report extends the ELF I codes developed in Phase I to handle geometries encountered in space pulsed power systems, and applies the resulting next–generation ELF2 codes to numerically analyze electrical stresses which could initiate potential breakdown mechanisms in critical subsystems, in a specific application of interest to SDI. The application selected to demonstrate the capabilities of ELF2 is the Space Power Experiments Aboard Rockets (SPEAR). These experiments are designed to gather critical data on the operation of pulsed power systems in the near–earth space environment.

Traditionally, simple computer models have been used to analyze electric fields and to develop grading structures in order to prevent flashover during operation of the pulsed power system. These conventional computer analysis techniques have been adequate because of the ease of making modifications to an experiment when flashover does occur and the non–catastrophic nature of a flashover. However, for SDI, the development of pulsed power systems of unprecedented degree of reliability is a matter of great importance to the success of the program. The ability to analyze electric fields produced by arbitrarily shaped conductors in the presence of nonuniform time–varying plasmas will be an important part of pulsed power production and conditioning systems. In this report we extend the development of Tetra's ELF computer codes to include configurations necessary for the solution of problems encountered in space pulsed power systems analysis.

The ELF Phase II project consisted of four tasks. These were: (1) defining the physics, identifying geometries and selecting test cases; (2) developing the grid generators for 3D dielectric geometries and other topologies; (3) testing and code verification using the ANALYZ code; and (4) conducting demonstration field analyses for the SPEAR III launch payload.

The selection of the SPEAR III launch payload as the paradigm for developing ELF2 led to two challenges: the plasma sheath physics for a large Langmuir probe in space and the geometry of the SPEAR payload. The geometry presented over an order of magnitude variation in scale size and the boom bushing of the payload had a highly re–entrant configuration. This in turn posed two requirements for grid generation: (1) grid stretching, and (2) topological flexibility.

In order to generate the required flexible topology, we developed a user–modifiable grid topology for ELF2. When mapping the physical space onto a logical cartesian space, the user is now able to alter the logical connectivity of a regular grid by creating selected cut–outs in logical space. An instructions–driven input technique was implemented to enable the non–expert user to build most geometries of interest by piecing together elementary geometrical shapes, in any given combination.

The internal consistency of the ELF codes was checked with the Computer Sciences Corporation ANALYZ program. The latter is a source—code static analyzer which identifies many classes of logical, semantical, syntactical and linkage errors, thus significantly reducing debugging times. The new ELF2 codes were run through ANALYZ with excellent results.

Two problems were selected to demonstrate the capabilities of the new ELF2 code. The first was a field analysis of the SPEAR III launch payload. The second problem dealt with a 2D and a 3D floating body test case.

There were insufficient funds to write a fully integrated Users Manual. However, all new coding is fully documented internally. Specifically, the new user interface modules are documented internally to the level of a user's manual. Also, running the interactive mode of the new input technique serves as a training session. The new input techniques are sufficiently intuitive that a typical user may successfully use them merely by modifying an example instructions file.

CONVERSION TABLE

Conversion factors for U.S. customary to metric (SI) units of measurement

To Convert From	To	Multiply
angstrom	meters (m)	1.000 000 X E–10
atmosphere (normal)	kilo pascal (kPa)	1.013 25 X E+2
bar	kilo pascal (kPa)	1.000 000 X E+2
barn	meter^2 (m^2)	1.000 000 X E–28
British Thermal unit (thermochemical)	joule (J)	1.054 350 X E+3
calorie (thermochemical)	joule (J)	4.184 000
cal (thermochemical)/cm^2	mega joule/m^2(MJ/m^2)	4.184 000 X E–2
curie	giga becquerel (GBq)*	3.700 000 X E+1
degree (angle)	radian (rad)	1.745 329 X E–2
degree Fahrenheit	degree kelvin (K)	$t_K=(t°f + 459.67)/1.8$
electron volt	joule (J)	1.602 19 X E–19
erg	joule (J)	1.000 000 X E–7
erg/second	watt (W)	1.000 000 X E–7
foot	meter (m)	3.048 000 X E–1
foot–pound–force	joule (J)	1.355 818
gallon (U.S. liquid)	meter^3 (m^3)	3.785 412 X E–3
inch	meter (m)	2.540 000 X E–2
jerk	joule (J)	1.000 000 X E+9
joule/kilogram (J/Kg) (radiation dose absorbed)	Gray (Gy)	1.000 000
kilotons	terajoules	4.183
kip (1000 lbf)	newton (N)	4.448 222 X E+3
kip/inch^2 (ksi)	kilo pascal (kPa)	6.894 757 X E+3
ktap	newton–second/m^2 (N–s/m^2)	1.000 000 X E+2
micron	meter (m)	1.000 000 X E–6
mil	meter (m)	2.540 000 X E–5
mile (international)	meter (m)	1.609 344 X E+3
ounce	kilogram (kg)	2.834 952 X E–2
pound–force (lbf avoirdupois)	newton (N)	4.448 222
pound–force inch	newton–meter (N·m)	1.129 848 X E–1
pound–force/inch	newton/meter (N/m)	1.751 268 X E+2
pound–force/foot^2	kilo pascal (kPa)	4.788 026 X E–2
pound–force/inch^2 (psi)	kilo pascal (kPa)	6.894 757
pound–mass (lbm avoirdupois)	kilogram (kg)	4.535 924 X E–1
pound–mass–foot^2 (moment of inertia)	kilogram–meter^2 (kg·m^2)	4.214 011 X E–2
pound–mass/foot^3	kilogram/meter^3 (kg/m^3)	1.601 846 X E+1
rad (radiation dose absorbed)	Gray (Gy)**	1.000 000 X E–2
roentgen	coulomb/kilogram (C/kg)	2.579 760 X E–4
shake	second (s)	1.000 000 X E–8
slug	kilogram (kg)	1.459 390 X E+1
torr (mm Hg. 0°C)	kilo pascal (kPa)	1.333 22 X E–1

*The becquerel (Bq) is the SI unit of radioactivity: Bp = 1 event/s.

**The Gray (Gy) is the SI unit of absorbed radiation.

TABLE OF CONTENTS

LIST OF ILLUSTRATIONS

LIST OF ILLUSTRATIONS (continued)

SECTION 1
EARLY DEVELOPMENT OF THE ELF CODES

The Electric Field (ELF) analysis codes were initially developed as a tool for the design of electrodes for gas discharges, such as those in electric lasers and pulsed power switches (Ref. 1). The design of electrodes is well defined only for unrealistically idealized conditions. The frequently used Rogowski electrode shapes are "optimal" only in the sense of producing an enhancement factor of unity, i.e., the electric field strength is nowhere greater than the nominal value. More importantly, the solution is based on vacuum conditions and is not a complete specification, i.e., the Rogowski shape is not closed, and must be completed by some (usually arbitrary) closure, such as blending with a radius. The same is true of the Chang electrodes. In addition, vacuum calculations do not properly include the field distortion effects of plasmas or arcs. Finally, conventional E—field codes do not calculate the electric fields on conductive surfaces accurately, with errors typically from 10 to 30 percent at the surface (Ref. 2). The boundary—fitted coordinate system used in ELF makes possible very accurate analysis of electric fields on conductor surfaces. Comparisons with analytic solutions have yielded accuracy of better than 0.1 percent using only modest grid resolution.

The ELF computer codes address the realistic electrode design problem, including nonuniform plasmas and complete electrode specification including "packaging" constraints of overall size. Using efficient finite difference methods in boundary—fitted coordinates, the ELF codes make it practical to design the electrode geometry and operating parameters during interactive sessions on a VAX computer.

For example, the electrodes for the Radial CO_2 Laser (RCL) were designed by Tetra using the ELF codes as follows. The electrodes are essentially concentric cylinders between which current flows radially. However, the ends needed to be fluted in such a way that field distortions (especially enhancements) are kept under control. Numerical machining considerations indicated elliptical cross section curves would be cost effective. A series of 2D ELF calculations assuming constant conductivity quickly lead to the near optimal design illustrated in Figure 1, below. The plot labeled "RCL 1.5 × 2.5 Shaper" shows the E—magnitude contours for the final design. There is a maximum field at the inner electrode, but it is less severe than for ellipses with slightly higher or lower eccentricity. The accompanying engineering drawing in Figure 1 is a detail of the final blueprints for the RCL machine, which has been operational at Tetra's laboratory since January, 1987.

The code applications go beyond the electrode design problem, and have included analyses of pulsed electric CO_2 lasers, xenon flashlamps, glow discharge switches, and modeling of plasma streamers. For xenon flashlamp calculations and for streamer calculations, the code was modified to also calculate temperature at each node point by implicit time integration of an energy equation with nonlinear coupling to the E—field. These calculations have given insight into streamer formation and propagation in plasma discharges, electrode effects in self—sustained glow discharges, and lensing effects in glow discharges due to nonuniformities from external ionization sources. Also, the effect on conductivity of an externally applied magnetic field is included as a first order perturbation calculation.

For many cases studied, the electric field solutions differ significantly from vacuum calculations, indicating that the commonly used Rogowski solutions and Chang solutions for the electrode shapes are far from optimal for important classes of

1

problems. The true optimal geometry is, in fact, strongly dependent on the discharge kinetics and the operating conditions whenever significant physics are involved in the conductivity. Also, different devices may have different optimality criteria; e.g., an electron beam laser may be designed to give nearly uniform energy deposition in the cavity, whereas a self–sustained discharge may be designed to minimize the local extrema of the electric field strength, subject to external packaging geometry constraints, in order to minimize arcing and maximize the discharge stability.

A single code is used for all 2D calculations, both steady–state and time—dependent. Three–dimensional steady–state and time–dependent calculations are done in a separate code and are used to design the roll–off of the electrodes in the third dimension in order to minimize locally high electric fields due to edge effects.

In the 2D code, options are available for planar, axisymmetric, or radial electrode geometries. Boundary conditions and boundary shapes may be time dependent; in particular, an external circuit module is provided so that electrode potential may be calculated as part of the solution, dependent on the integrated current through the cavity, rather than being specified *a priori*. The geometry and conductivity calculations are modularized so that they may be readily modified by the user.

Automatic grid generation is performed interactively using elliptic generating equation techniques. As an option in the 2D code only, a solution adaptive grid generation technique is used to adapt the grid to the solution (either in the steady–state solution, or within an intra–time–step interation for a time–dependent problem) in order to increase the resolution of the maximum electric field strength (always an important design parameter) and enhance the accuracy.

The code accounts for externally controlled or self–sustained glow discharges or other plasmas, such as arcs, by modifying the nonlinear conductivity. The conductivity is obtained by time integration of the ordinary differential equations for electron number density at each mesh point in the 2D or 3D grid, coupled nonlinearly to the local E–field. The electron drift velocities and discharge kinetics coefficients are obtained by interpolation of tabular data obtained either empirically or from Boltzmann code solutions performed beforehand (i.e. noninteractively) for the particular gas mixture used.

The development of the codes has involved an interdisciplinary approach including gaseous electronics, laser physics, numerical mathematics, and software engineering. The computational techniques developed and embodied in the codes include the following areas: semidirect/marching methods for nonlinear elliptic equations, fully implicit methods for strongly coupled nonlinear time evolution equations, solution–adaptive boundary–fitted grid generation, computational farfield boundary conditions, gas conductivity modeling, parametric surface representations, super microcomputer operations, artifical intelligence (computer symbolic manipulation), code validation procedures, software engineering for interactive codes, and numerical machining considerations.

As described above, the ELF codes are potentially capable of handling the geometries that may be encountered in spacecraft pulsed power or power conditioning systems. However, the ELF codes did not include dielectrics. The physical description also needed to be modified to include time dependent space charge development.

2

In Phase I, the ELF codes were modified to include dielectrics, and the formulation to handle time–dependent space–charge effects was developed. In Phase I the 2D code was enhanced to include a dielectric body only for a simple familiy of geometries, and analyses were conducted to determine the feasibility of implementing dielectrics in extended geometries, including three dimensions.

For Phase II, Tetra proposed to develop the next generation ELF2 code. This new generation would expand the geometrical capabilities of the Phase I code, especially in 3D, including dielectrics. In the process, the code performance is improved, especially in the grid generation, and in the user interfaces to the code. At the completion of the Phase II program the ELF code will allow realistic modeling of particluar SDI–related problems, including analyses of the E–field environment for unusual geometries and of dielectric insulation in specific conductor geometries.

RCL 1.5 x 2.5 Shaper   E÷FIELD
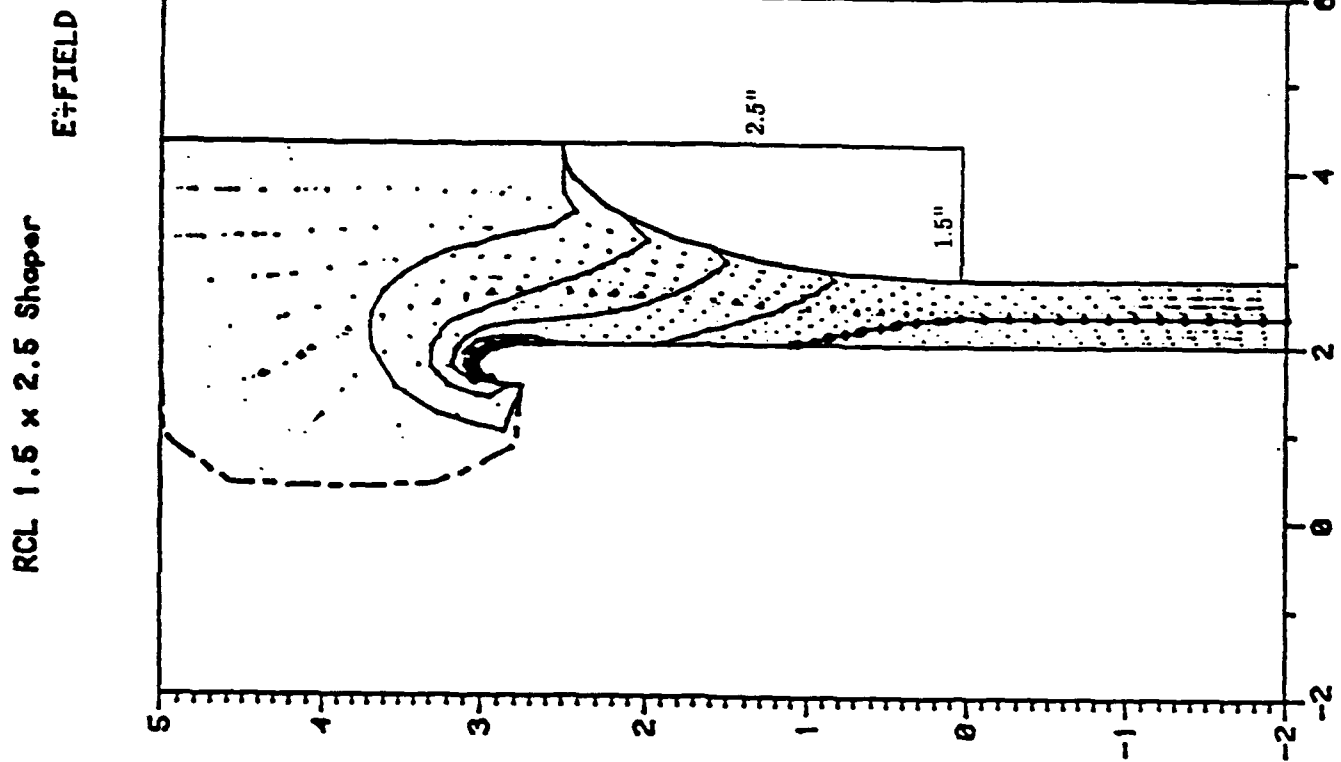
a.   E—magnitude plots produced by ELF.
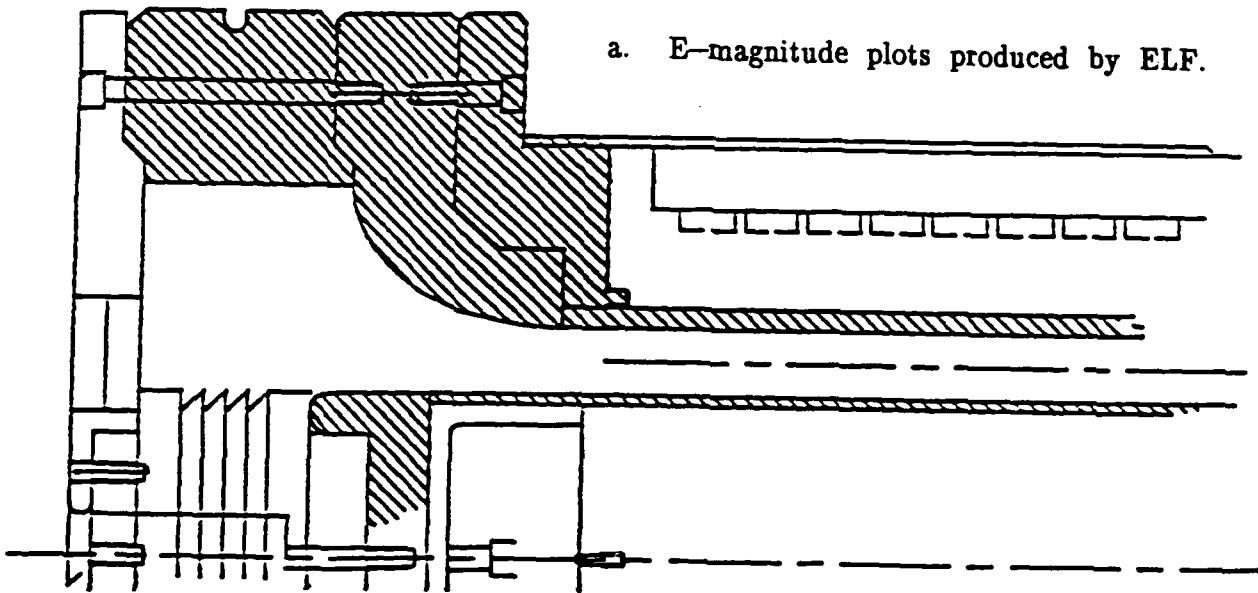
b.   Engineering drawings of final design.

Figure 1. RCL field-shaping electrodes design.

SECTION 2
PHASE II PROGRAM PLAN

2.1 OBJECTIVES.

The Phase I ELF code demonstrated the feasibility of powerful additional capabilities needed in the analysis and design of space pulsed power sytems. The Phase II program was proposed to significantly expand the ELF code capabilities, apply the resulting ELF2 codes to analyses of selected design details in a real space pulsed power payload of interest to SDI, and deliver a set of next—generation ELF2 codes useful for many applications in pulsed power sytem analysis and design, especially in space plasma environments.

The proposed extensions of the ELF I Code capabilities were focused on expanding the code geometrical capabilities. The Phase I effort demonstrated the feasibility of including dielectrics by implementing one specific topology in 2D, and was therefore limited to one class of topologically equivalent geometries. In Phase II, topologies were addressed to handle other geometries encountered in real device system and subsystem designs. Algorithms initially coded in 2D were generalized and implemented in 3D to model edge effects and to handle the complex geometries of real—life engineering design analyses required when SDI concepts are implemented in concrete prototype systems. In the process, the ability by third parties to use ELF codes is significantly increased by improvements in internal documentation and structure of user—modifiable modules, and facilitation of user input and output.

2.2 RATIONALE AND APPROACH.

Concepts being investigated under the Strategic Defense Initiative are stretching the state—of—the—art in many technologies. Most of them have ambitious pulsed power requirements which will necessitate significant advances in analysis and design tools, including electric field mapping. SDI battle station requirements for both continuous and burst power are significantly beyond our present engineering experience in space (Ref. 3). High voltage insulators in space are often limited by damaging surface flashover or sudden discharges after accumulations of injected charges.

The SPEAR program is a set of space plasma physics experiments designed to collect basic data on which to base high—voltage pulsed power engineering criteria for SDI space—borne systems. Tetra was invited to the SPEAR I Preliminary Design Review in Seattle, WA in mid—June, 1987, to see what contributions the ELF code could make to the program. The ELF2 codes would have ideally served the objective of risk management in the unknown space environment. The problems involve sophisticated plasma physics phenomena and complex geometries. The physics include a plasma sheath of thickness comparable to experiment sizes, non—local field dependent currents (due to long mean—free—paths), and possibly geomagnetic field effects. Geometrical complexities include many conductor rings in the plasma shield bushings, and asymmetries which make several problems strongly three—dimensional.

Unfortunately, the ELF2 code was not available to influence the SPEAR I design. The Phase I code's usefulness was limited to critical design details, such as the field distributions between the first (grounded) and second bushing rings and the HV cable for either "vacuum" conditions or a simplified plasma conductivity

5

model. The significant new capability for electric field numerical simulation, design and analysis resulting from the Phase II next–generation ELF program will provide valuable assistance in analyzing the design and results of the SPEAR experiments and many other pulsed power systems in the future.

The ELF codes are uniquely suited to electric field analysis in the presence of arbitrarily–shaped conductors and nonhomogeneous, nonlinear and time–dependent plasmas because of their unique boundary–fitted grid generation approach and their efficient finite difference methods. The approach used in Phase II has made maximum use of the numerical methodologies already in place in the existing ELF 2D and 3D codes. However, for realistic analyses of pulsed power sytem design details, it will be necessary to use special grid generation techniques for nontrivial 3D geometries, including dielectrics in 3D.

Except for truly difficult 3D geometries (e.g. linked toroids), extension of 2D algorithms to 3D is relatively straightforward, but very tedious. Before developing the non–dielectric (pre–Phase I) 3D ELF code, we estimated the algebraic manipulations would require over two man–years. That was considered infeasible not only economically, but also because of the great difficulty of assuring error–free performance by the programmer. The solution was found in use of the artificial intelligence based symbolic manipulation program MACSYMA^{TM} (Ref. 4).

In order to keep costs within the proposed level of effort, a few simplifications were necessary. The first simplification is to assume perfect vacuum conditions in space. This is an acceptable approximation for modeling the field distributions prior to the inception of insulator breakdown. This will provide useful insight into possible weaknesses (field stress points) which may lead to insulator breakdown. It also provides initial conditions for models of hypothesized breakdown mechanisms in space plasma environments. The significant physics limitations of this simplification is descirbed in this report along with possible optional extensions to remove some of these limitations.

The second class of simplifications involves geometries. The Phase I code was limited to one 2D topology: the dielectric body must cover one of the four boundaries and part of the two adjacent ones. While this served the Phase I purpose of demonstrating the feasibility of a dielectric ELF code, many practical applications require different topologies. Electron and ion sources usually have a third "focusing" electrode, which topologically comprises a "floating" body. Corona rings require a large number of floating conductors to be modeled, as do transformer windings, to design appropriate field shaping shields. Realistic modeling of spacecraft charging requires many conductor and dielectric bodies. Common difficulties in analyzing high voltage insulation materials are triple–point junctions, use of several insulation materials in layers, and unintentional voids in the insulation. All these applications require modeling topologies other than the one chosen for proof–of–principle in Phase I.

In order to perform complete analyses of such complex geometries, we proposed to extend the geometrical capabilities of the ELF codes. Specifically, we have extended the 3D geometries to handle complex structures commonly expected to affect field distributions near stress areas, including dielectrics in 3D. In Phase I, only one 2D topology was implemented, but many goemetries can be handled within that topological family. In Phase II, a significant level of topological flexibility was implemented in 2D and 3D, so the next–generation ELF2 codes will

6

be able to handle many more applications with more complex geometries, and the grid generation techniques implemented will be extendable to yet other geometries with limited additional effort.

2.3 TASK BREAKDOWN.

The Phase II program was divided into five tasks, and a number of sub—tasks.

2.3.1. Problem Definition.

a. <u>Define physics limitations.</u> The plasma physics conditions under which the ELF codes apply were carefully defined. Possible further extensions which could remove or ameliorate significant limitations at varying levels of effort were identified.

b. <u>Define geometries.</u> Tetra defined the classes of geometries to be addressed in consultation with both the Contract Technical Monitor to insure responsiveness to mission requirements, and with Ecodynamics to insure feasibility of the modeling.

c. <u>Identify test cases.</u> Test cases for final verification were defined jointly by Tetra and Ecodynamics.

2.3.2. Grid Generators.

Ecodynamics was responsible for algorithm development and coding required for modifications and extensions to the present ELF codes required to handle the specified classes of geometries. These extensions included the following:

a. <u>Implement dielectrics in 3D.</u> This implemented a 3D version of the Phase I dielectrics in 2D.

b. <u>Implement 3D families.</u> This extended the 3D codes to those families of geometries identified in Task 1.a.

c. <u>Extend topologies.</u> This extended the Phase I 2D topology to meet the specific requirements defined in Task 1.a.

2.3.3. Test and Verification.

a. <u>ANALYZ.</u> We tested all coding with support from CSC as needed using their proprietary ANALYZ codes. All detected errors were corrected.

b. <u>Test Error Convergence.</u> Algorithm correct coding was verified with systematic error convergence tests.

c. <u>Run Test Cases.</u> Test cases were run by Ecodynamics, and refinements made as necessary. Tetra ran some final test cases before final acceptance of verified code, providing feedback to Ecodynamics on user friendliness of input/output.

2.3.4. Demonstration Field Stress Analyses.

To demonstrate the power of the next—generation ELF2 codes, we chose to analyze critical subsystems in the SPEAR III payload. Specifically we analyzed the first two rings of the voltage—grading bushing, and the field enhancements they produced.

2.3.5.   Program Management.

a.   <u>General Management and Reporting.</u>   Tetra was responsible for general management and integration, including periodic progress reports, program management, insuring responsiveness to user needs as expressed in guidance from the Contract Technical Monitor, fiscal management and reporting, and technical integration of the effort.   Two formal Program Reviews were conducted for the Contract Technical Monitor and his designated representatives, consultants and advisors.   Written quarterly progress reports were submitted to report significant technical achievements and/or problems.

b.   <u>Final Code Documentation and Delivery.</u>   Internal documentation was concurrent with coding, and testing followed every major modification. Documentation of every option and conglomerate input/output specifications and running instructions will facilitate subsequent use of the deliverable ELF2 codes by scientists and engineers in government and industry.   A copy of the final code will be made available to any member of the SDI Space Power Consortium on request.

c.   <u>Final Report Preparation.</u>   This final technical report documents the Phase II ELF code extensions, including rationale, caveats and limitations, and the demonstration SPEAR II analyses, including ELF computation results and interpretation.

SECTION 3
PROBLEM DEFINITION

3.1 SPEAR PARADIGM.

The development of any large computer code like ELF is guided in practice by the needs or requirements of specific problems. In order to insure that the next generation ELF2 development would be responsive to real needs of the pulsed power community working on SDI research, we sought a model problem, or paradigm.

We chose the payload of the SPEAR third launch to provide that paradigm. The SPEAR program seeks to gather basic data on the low earth orbit plasma environment as it affects and limits pulsed power systems in space. This choice was driven by both the relevance of the mission, and the challenge to E–field computations. The mission is highly relevant, because most space–based SDI concepts require pulse power levels unprecedented in space, and careful field management may be critical to the success of many subsystems. E–field analysis of the SPEAR III payload is challenging in both the plasma physics and the geometries that must be modeled.

3.2 PLASMA SHEATH PHYSICS: THE FIRST CHALLENGE.

The main SPEAR experiment is essentially a large Langmuir plasma probe. A 20 cm conducting sphere is pulse–charged to a high voltage with respect to plasma ground, and the current drawn from the space plasma is measured at different voltages (up to 45 kV).

The dominant phenomenology involves the formation of a plasma sheath around the probe, which shields the bulk of the plasma from electric fields. To understand the phenomenology, consider a positive voltage, which attracts electrons and repels positive ions. Within an ion transit time, the sheath will have no ions at all, but the space plasma reservoir will continue feeding electrons into the potential well trap. The field distribution will be affected by the space–charge of the electrons. That space–charge density will vary significantly, since each electron in the collissionless plasma accelerates from the few eV characteristic of the ambient plasma to the tens of kilovolts applied to the current collector of the probe. The space–charge will be strongest near the edge of the sheath, where the electrons are slowest. That space–charge field causes the total E–field to end rather abruptly at a well–defined sheath edge. A steady–state is quickly established at the radius where the random thermal current from the ambient plasma exactly matches the space–charge–limited current from the sheath edge to the current collector, which remains at the same voltage V as long as the driving circuit can handle the collected current I. The measured I vs V curves provide the primary diagnostic, from which plasma parameters such as temperature and number density can be backed out.

This plasma physics regime presents a challenge for the ELF codes, because the field solutions are clearly driven by the space–charge distribution. The original applications of ELF involved collision–dominated plasmas, where the field solution is driven by the conductivity σ via the Laplace equation:

$$\nabla \cdot \sigma \nabla \phi = 0 \qquad (3.1)$$

9

This new situation is ρ-driven, via the Poisson equation:

$$\nabla^2\phi = -\rho/\epsilon_0 \qquad (3.2)$$

where ρ is the space-charge density and ϵ_0 is permittivity of free space. Mathematically, both are elliptical field equations, but the second is nonhomogeneous because the right hand side is non-zero. They are both nonlinear, because, in general, both σ and ρ depend on the fields we want to solve for. However, the nonlinearity can be handled with a computational loop, as long as the space-charge ρ can be calculated given an estimated E-field solution within each loop iteration in such a fashion that the numerical system converges.

If we ignore the unavoidable connection bringing the high voltage to the current-collecting sphere (and carrying away the collected current), the problem becomes one dimensional. The symmetry is that of concentric spheres, with the only independent spatial parameter being radius R. The analytical solution to the space-charge limited current between two concentric spheres was published by Langmuir and Blodgett in 1924 (Ref. 5). That analytical solution serves as the basis for a benchmark to test a 2D rho-driven E-field solver, as described in detail in Appendix A. However, the Langmuir-Blodgett Theory is just a starting point.

We eventually built a numerical solution based on the 1D ordinary differential equation

$$\frac{\partial^2\phi R^2}{R^2\partial R^2} = -\rho/\epsilon_0 \qquad (3.3)$$

with the solution at any specific radius R serving as initial conditions. We used the expression for calculating ρ/ϵ_0 used in the NASA Charging Analyzer Program for Low Earth Orbit (NASCAP/LEO) derived by I. Katz, *et al* (Ref. 6). This numerical 1D model was used not only to generate benchmark test cases for the 2D ρ-driven ELF code, but also to test other corrections to the basic Langmuir-Blodgett model. (See Appendix A for details.)

Implementation of a 2D ρ-driven ELF code required that the ρ calculation be a local calculation. (The alternatives, ray-tracing and particle-pushing, are computationally expensive.) The key is a local calculation of the current convergence factor. In 1D, that is trivial as long as the sheath radius R_s is known or can be estimated. The spherical convergence of current lines concentrates the space charge by a factor $(R_s/R)^2$, where R_s is the sheath radius. However, for a general 2D geometry it is not obvious that the convergence factor can be calculated or estimated from strictly local parameters. That problem was solved in the NASCAP/LEO model by an empirical fit for the convergence factor as a function of local fields E,ϕ derived by M. J. Mandell *et al* (Ref. 7) That fit is adequate for the purpose of estimating the total current collected by the probe. However, we found some inconsistencies when we applied Mandell's fit to the 1D spherical problem. Eventually, we came up with an alternative procedure based on our numerical solution to the basic differential equations. That alternative is fully described in Appendix B.

The complete algorithm was coded in module SPCHRG, which generates a custom convergence factor fit function during initialization, and subsequently calculates the space-charge ρ from the local fields E,ϕ. That module was integrated into a

special ρ—driven version of the ELF code. The nonlinearity is handled numerically by under—relaxation. Tests on a simple model problem indicated that convergence is readily obtained for the small perturbation effect of the SPEAR III conditions, as expected. However, the result does not display the correct plasma sheath behavior at the edge.

The problem is actually a Stefan, or free boundary, type of problem. Two approaches are possible. In the more accurate approach, the plasma sheath boundary would be set at the outer boundary of the computational grid, and solved by iteration. This approach requires a new grid generation at each outer iteration; besides being expensive, there are ambiguities involving the evaluation of the E—field such that both potential and the difference expression for E can be driven to zero at the same location. The other approach involves solution on a fixed grid, with the potential values between the sheath and the outer boundary being driven to zero. The difficulty here is in obtaining the correct behavior with the sheath edge not lying exactly on a node point.

These difficulties lie beyond the ELF2 scope, but could be addressed in follow—on efforts. Several applications to the SPEAR III mission are described in detail in Appendix C, with specific plans on how to modify the ELF codes to meet those needs.

Because these difficulties lie beyond the scope of the ELF2 level of effort, we did not integrate the ρ—driven option into the permanent ELF code but left it in a special—purpose version of the ELF code. Furthermore, the 1D calculations make it clear that the filed solution is not significantly different from the vacuum solution except near the sheath edge. Therefore, we proceeded with the geometrical challenges posed by the SPEAR model problem without the space—charge effects.

3.3 GEOMETRY: THE SECOND CHALLENGE.

There are actually two difficulties with the SPEAR III geometry. The first difficulty is that the geometrical scale size varies by orders of magnitude. The second is that the geometrical structure of the boom bushings is highly re—entrant. We dealt with these two difficulties in different ways.

Figure 2 shows the general layout of the planned SPEAR III payload. The focus of our interest is the conducting sphere at the end of the boom, at the top of the figure, and the plasma sheath it will create when a high voltage pulse is applied. The largest scale—size of the SPEAR III problem is given by the radius of the sheath. That varies with the applied voltage, but the order of magnitude is 10 meters. At the other extreme we have the 20 cm current collecting sphere. That gives a range of two orders of magnitude.

The idealized vacuum 1D spherical problem has a simple analytical solution. The spherical symmetry requires that ER^2 be constant; ϕR is constant if ϕ is referenced to $R = \infty$. Although the analytical solution is simple, this represents a relatively severe test for a finite differences code like ELF, since on linear axes the solution is not at all benign. In fact, it should be obvious upon reflection that a stretched grid is indispensable. We artificially caused the 2D ELF code to generate a grid where the constant—R grid—lines were equi—distributed on a log scale. The resulting grid is shown in Figure 3. Notice the constant aspect ratio of every grid cell.

11

However, even with an ideally stretched grid, we cannot expect ELF to produce the exactly correct field distribution. That is because the discretized numerical analogue of the differential equations are only an approximation of the continuous equations. Discretization errors in each cell will accumulate across the grid, so we cannot expect to get arbitrarily close to the exact solution merely be reducing the numerical tolerance. What we can expect is that the discrete solution will approach the analytical solution as the grid is progressively refined. Therefore, we first calculated an ELF solution with a sparse grid of only 33 constant–R grid–lines, and then with a refined grid of twice the resolution (65 lines). As shown in Figures 4 and 5, the 65 grid solution has about half the error of the 33–grid solution. Thus, ELF successfully passed the grid–convergence test.

Figure 6 shows a close–up of the planned current–collecting sphere and the voltage–grading bushing surrounding the high–voltage feed at the center of the supporting boom. The first step toward analyzing the field enhancements near the first bushing ring was to provide credible far–field boundary conditions. That was done by solving the field distributions between an idealized sheath edge and an idealized boom/sphere (Figure 7). That solution was imposed on the outer boundaries of the "close look" physical space shown in Figure 8. Notice that not only do we have another serious scale–size range problem, but also a problem with the highly re–entrant geometry of the busing rings (only two of which are modeled – the rest are idealized). This required the unusual logical computational space topology shown, with its cut–outs and extensions. The dashed lines represent grid control lines, required to insure appropriate stretching of the grid.

In summary, the unusual requirements of the SPEAR paradigm suggest two requirements for grid generation: 1) grid stretching, and 2) topological flexibility. In general, the user needs control over both areas. In the following chapter we shall describe the methods we implemented in the next generation ELF codes to provide the user with those capabilities.

12
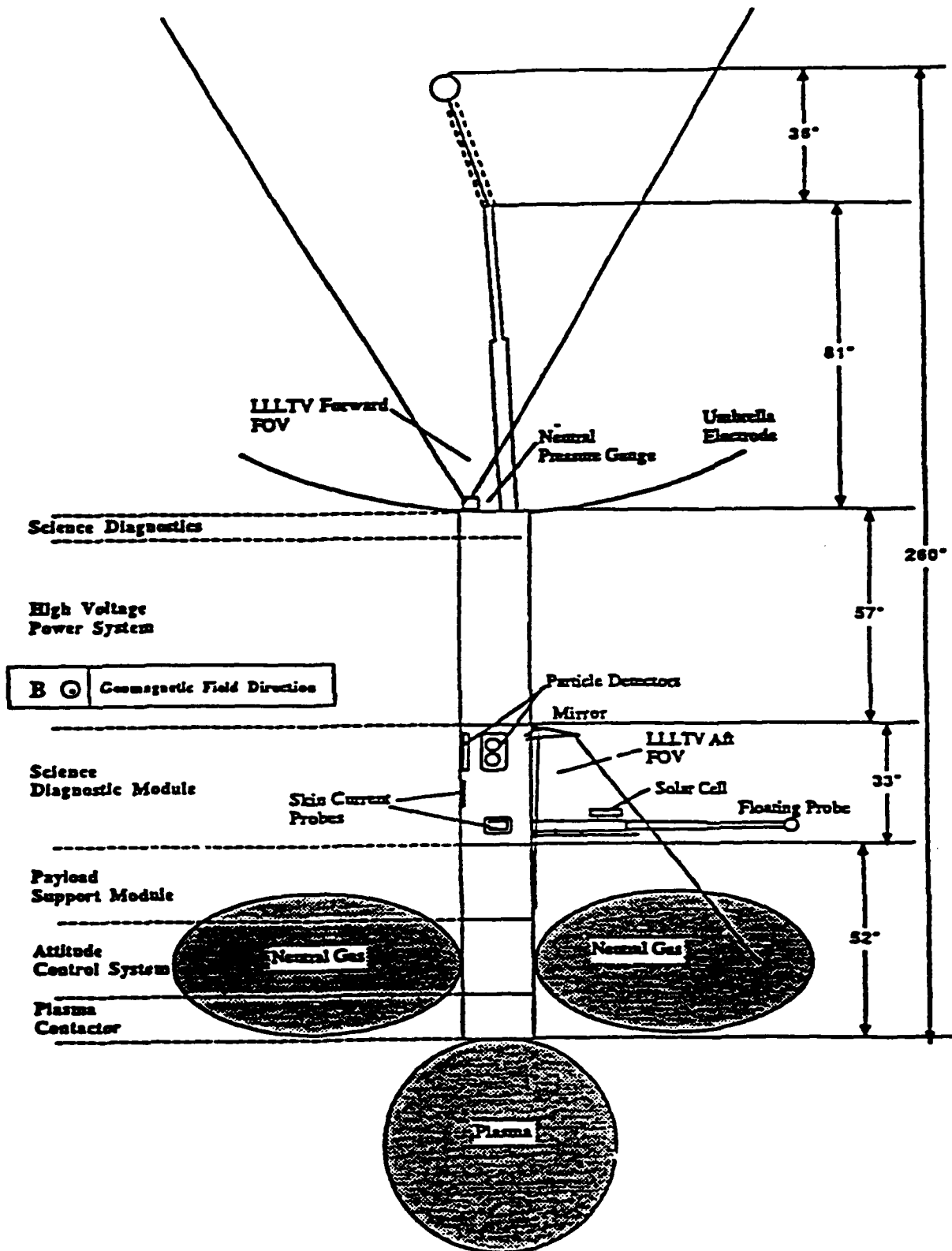
Figure 2. Conceptual design of SPEAR III payload configuration and orientation.

SPHERES IN VACUUM – LOG R GRID   R = 0.2 TO 10. METERS
GRID
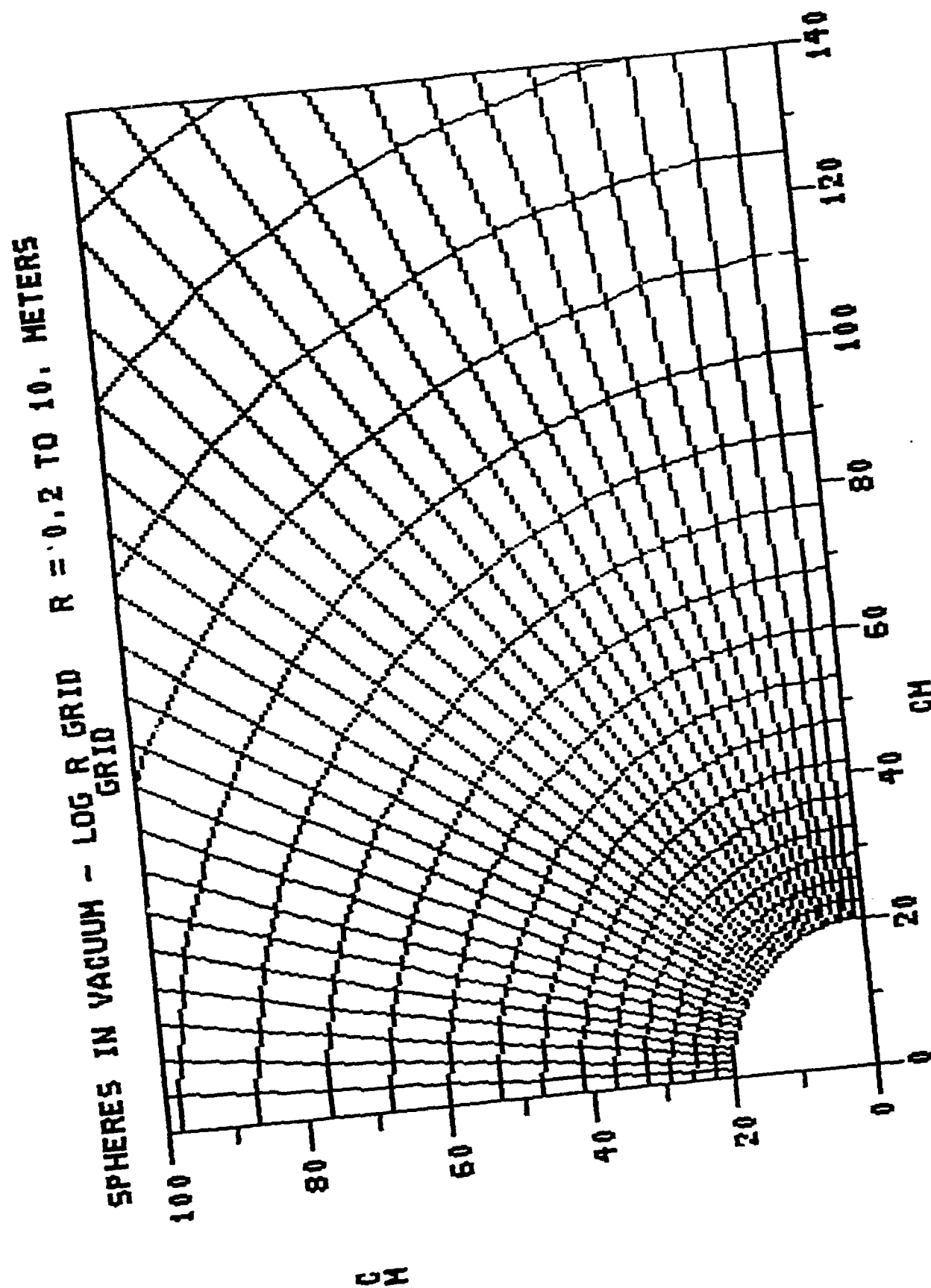
Figure 3. Detail of 33 × 33 log–R grid.

14
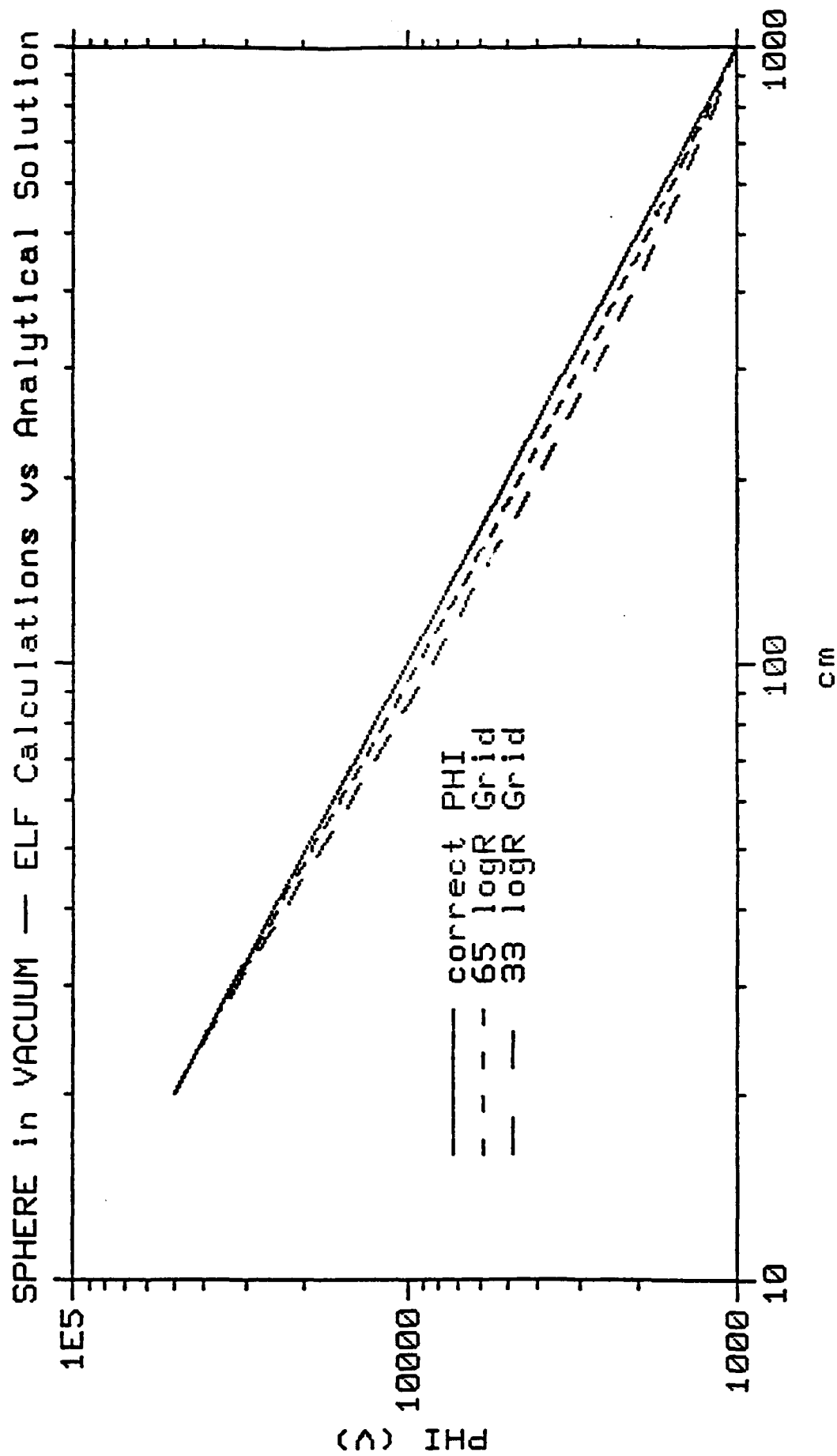
Figure 4. Comparison of exact electric potential ϕ solution to medium and low density grid numerical solutions.
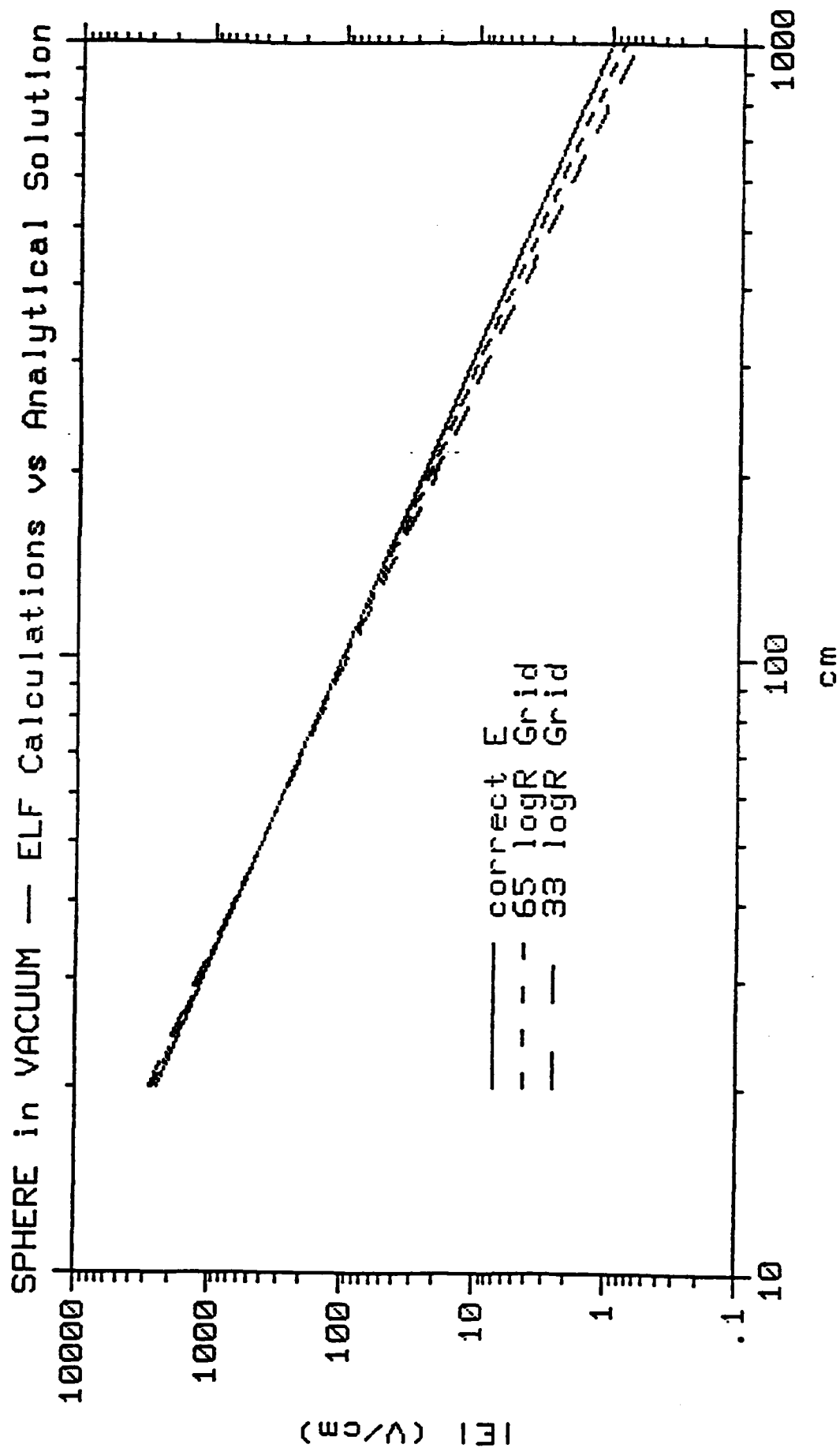
Figure 5. Comparison of exact electric field E solution to medium and low density grid numerical solutions.

7.874⁢ dia.

Collected
Current

50 kV

Enhanced
E–field

ΔV

ΔV

ΔV

ΔV
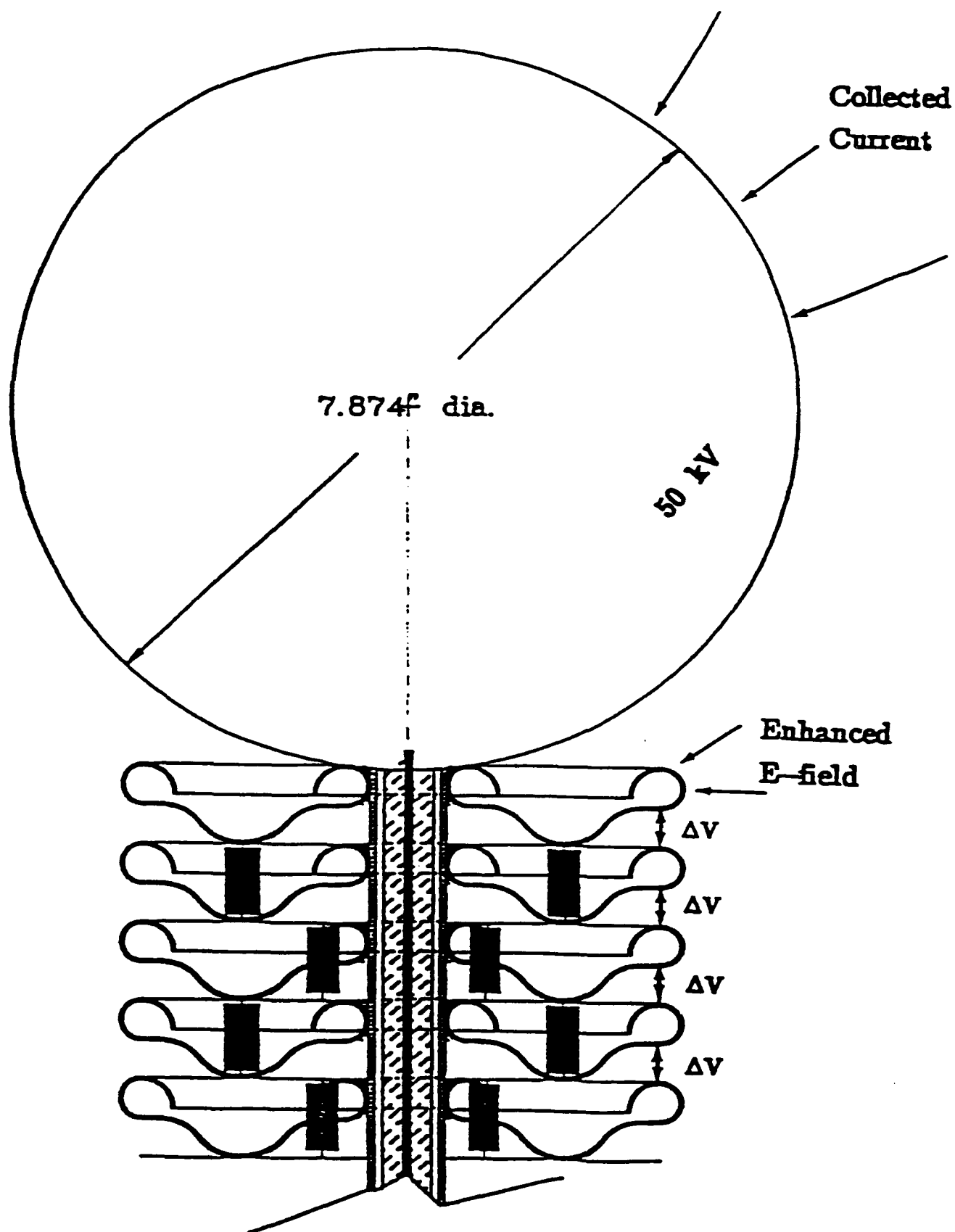
Figure 6. Close–look ELF analysis to determine current collected
by first bushing ring.

17
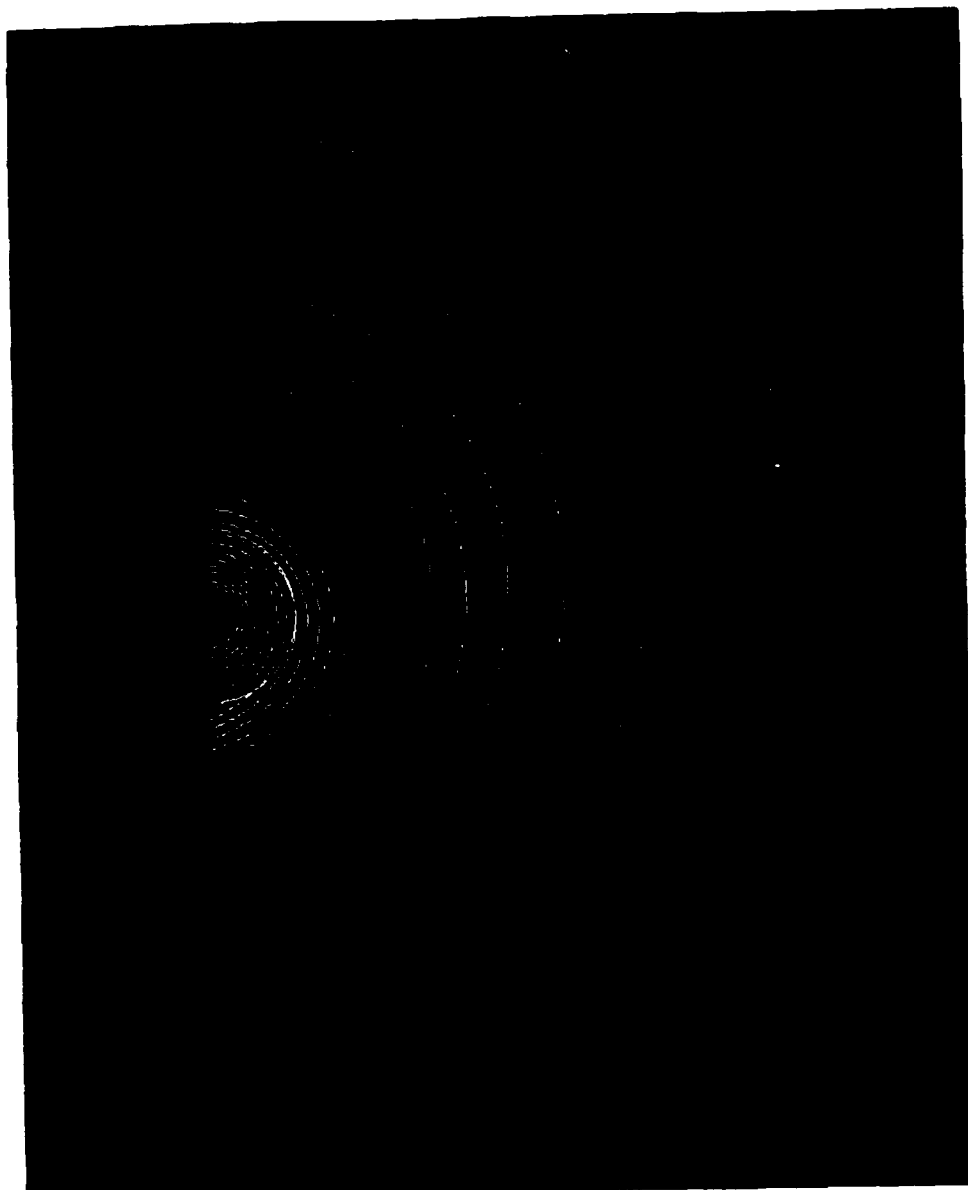
Figure 7. Field solution providing far-field boundary conditions for close look at SPEAR bushing first ring.

10

b) Computational Space
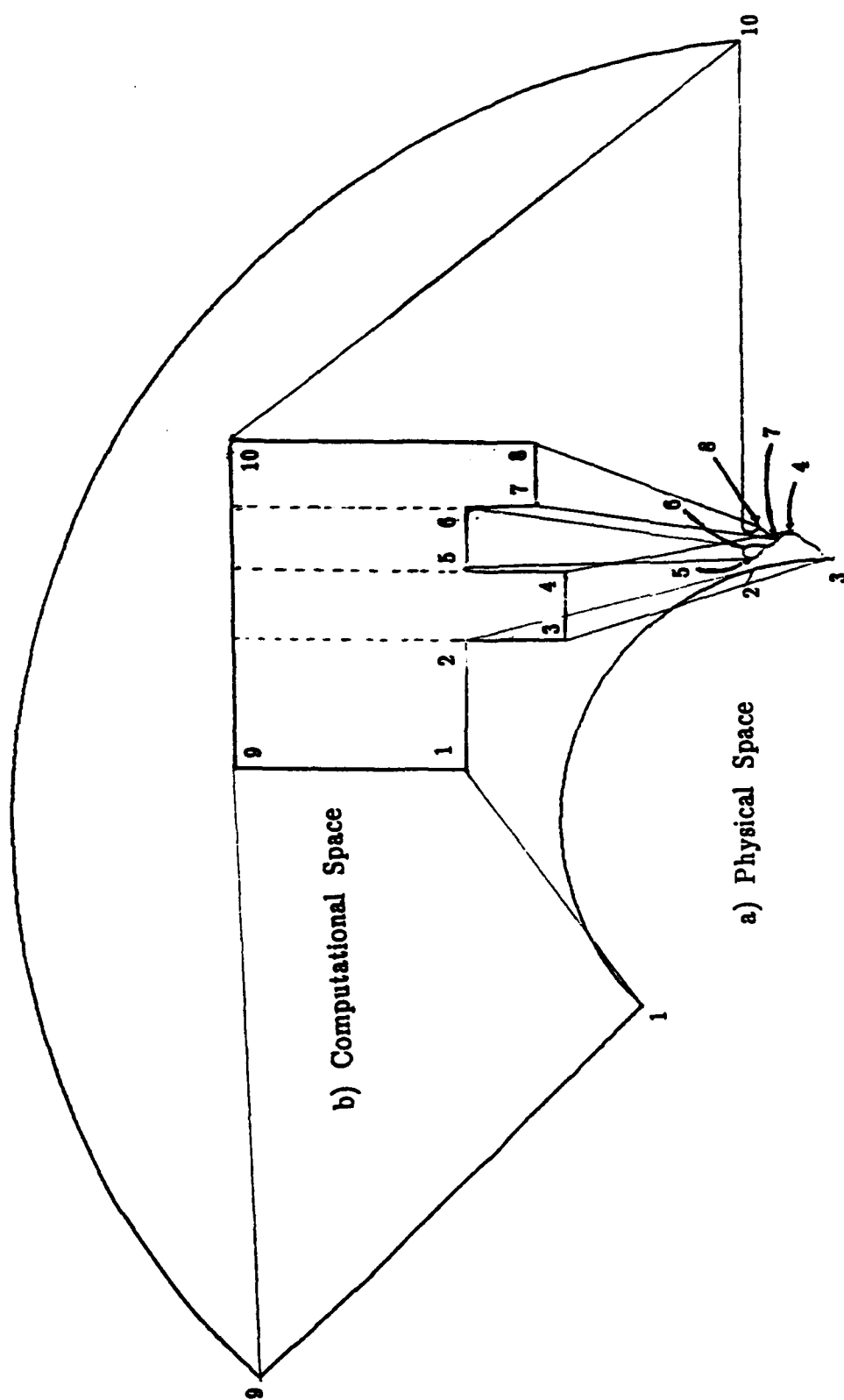
a) Physical Space

Figure 8. Relationship of SPEAR bushing close–look physical space geometry (outer) to logical computational space topology (inset).

SECTION 4
GRID GENERATOR

4.1 NEW FLEXIBLE TOPOLOGY.

One of the most significant developments of this effort was a technique to handle many difficult geometries with a user—modifiable grid topology. The basis of the ELF codes is a mapping of physical space to a logically cartesian space. In two dimensions, that logical plane is normally rectangular. Discretization of that rectangular plane results in a grid with the logical connectivity of a regular grid, as illustrated in Figure 9.

The user is now able to alter that topology by creating selected cut—outs in logical space. That is accomplished by "blanking out" certain rectangular areas of the grid, as illustrated in Figure 10.

The status of each node (intersection of two grid lines) is communicated throughout the code by the value in the corresponding position of an integer array called IBLANK. A value of 0 flags an inactive node; a value of 1 flags an interior node. Other values > 1 are reserved for special uses; for example, a boundary node is flaged by a value $\geq$ 6. Thus, a print—out of the IBLANK values arranged the same way the notes are related gives an immediate picture of the logical topology.

For many geometries, that is not enough, because left alone the grid generator would not provide adequate resolution of certain high—interest areas. For that purpose, the user may need to define control lines in addition to the interior boundaries created by the cut—outs. The actual positions of the nodes on a control line are subject to being changed by the grid generator, but the original spacing of the points on a control line will influence the grid generator, "pulling" grid lines toward regions of higher point density. In general, the stretching along a control line needs to be an exaggeration of the desired effect, but it must be smooth.

The spacing of the control line and boundary nodes is used to compute weighting functions Φ, Ψ at each active node by interpolation along grid lines. The weighting function calculation is performed internally by the code with no user intervention. However, the user needs to know that the control lines apply only for the Thomas—Middlecoff option (the default grid generation method), and he must understand the general effect of control lines explained in the paragraph above. Control line nodes are identified internally by a value 1<IBLANK<6.

4.2 NEW INPUT TECHNIQUE.

The capability to blank out selected areas of the logical—space grid significantly exceeds the requirements under Task 2, Grid Generator. However, it also created an unanticipated challenge to make this powerful new capability accessible to a non—expert user.

Therefore, we developed a module of coordinated utilities which allow the user to either interactively or in an instructions file do the following:

1.   Define the desired topology by "blanking" and "restoring" rectangular elements in any combination,

20

2.   Locate all boundaries and optional interior control lines, by combination of straight lines, segments of ellipses or superellipses, and distorted quadrants of superellipses, or specifying node location point—by—point,

3.   Set the boundary conditions by a default set (for most nodes), with exceptions specified node—by—node or by interpolation (by index, physical arc—length, X—only or Y—only).

This instructions—driven structure allows the user to build most geometries of interest by piecing together elementary geometrical shapes in any combination. The four elements on which he can build are described in detail in Appendix D. Other elements can be added in the future as needs arise with minimal additional coding.

The interactive mode on input is awkward for all but very simple geometries, since user errors are virtually unavoidable. Its primary use is for user training. In fact, a stand—alone program called INTBC was created specifically for user training.

The original input technique used for specifying boundary conditions required the user to specify the stencil values for the discretized differential equations. This requires an unusual degree of sophistication in the user's knowledge of numerical methods of solving elliptical differential equations. Rather than making the user set the boundary stencil values directly, it is preferable to let him operate at the higher level of abstraction of Neuman (specified potential) or Dirichlet (specified normal gradient) boundary condition types. Specifying potential is easy, as is specifying zero normal gradient in logical space. What is difficult is specifying a normal gradient in physical space, because derivation of the discretized normal gradient operator requires knowledge of the grid metrics. We developed the coding to automatically set the stencil for the first two cases: that is, the user can specify a potential distribution or a logical normal gradient. However, the physical normal gradient option was not implemented for lack of funding. That is left as an option for future development. Of course, an expert user may always specify the stencil directly.

Finally, we developed a general—purpose exterior boundary (no blanked areas) geometry and boundary condition definition module using the above user—friendly input techniques. That module is contained in the source code file ELECGEN.for. The ELECGEN module reads instructions to define the geometries of all four outer boundaries plus optionally a fifth surface for the dielectric body option. It also sets boundary conditions at the Neuman or Dirichlet level of abstraction, including the option to specify a physical normal gradient. That option is not operational only for interior boundaries created by blanked cut—outs.
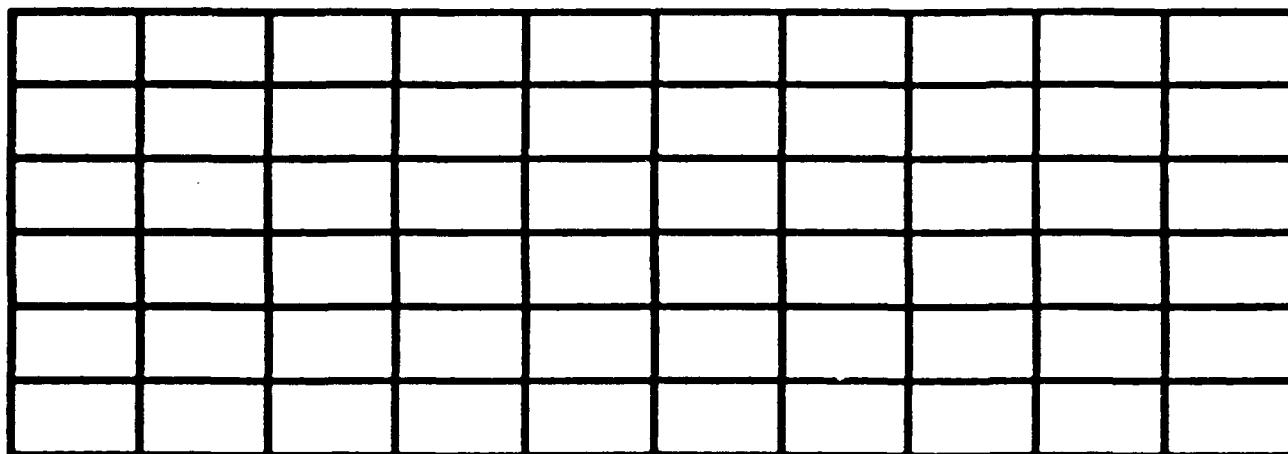
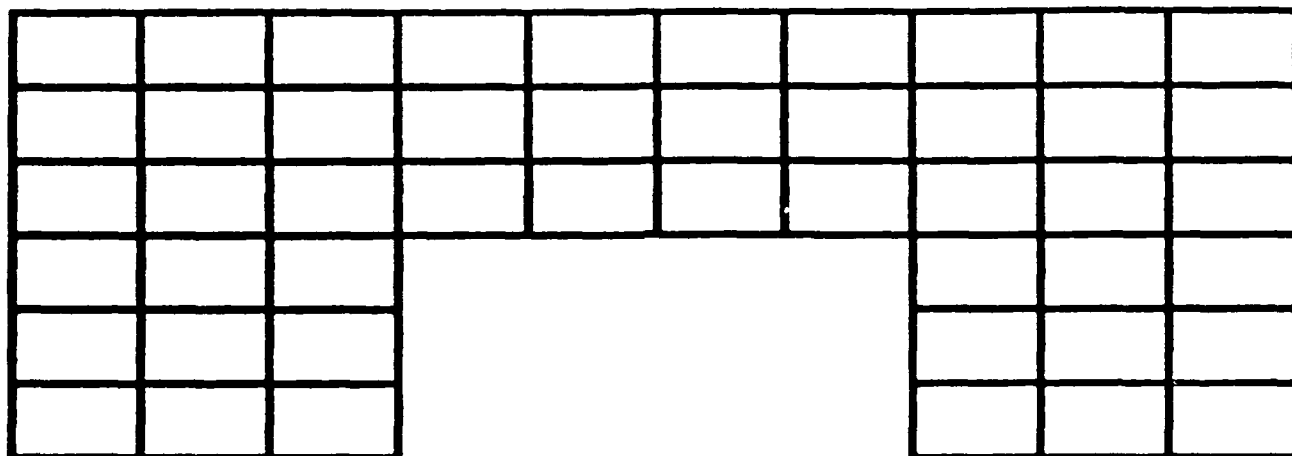Figure 9. Illustration of a full regular grid in logical space.

Figure 10. Illustration of a logical space grid with one blanked–out area.

SECTION 5
TEST AND VERIFICATION

5.1 CODE VERIFICATION.

The internal consistency of the ELF codes was checked with the Computer Sciences Corporation's (CSC) ANALYZ program. ANALYZ is a source—code static analyzer which identifies many classes of logical, semantical, syntactical and linkage errors (Ref. 8), and has been shown to significantly reduce debugging time in the development of codes much larger than the ELF codes (Ref. 9).

At the very beginning of the project, the entire existing baseline ELF source codes were run through CSC's ANALYZ Code. No serious errors were detected, but many diagnostic messages were generated. Most of those were only potential code transportability problems. Those diagnostics were ignored, since ELF2 development is limited to the VAX/VMS environment. The diagnostics from the ANALYZ code that may cause potential problems (although none of them serious) were fixed.

Toward the end of the project, after the main modifications to allow grid cut—outs, the new coding was run through ANALYZ again. The results were again excellent, with only warnings about code transportability issues. The recurring problems are as follows:

A. PRINT statements are used copiously throughout the codes. The problem is that the effect is environment—dependent. The intended effect is to write a message to the screen. In batch mode, most systems will divert the message to a LOG file. No easy fix is available that will work on all systems. A batch version of ELF in the future will require significant redesign of the input/output (i/o) and control structure in any event.

B. Mixed mode arithmetic is often used. This is considered undesirable because the effect is not clear. However, the FORTRAN 77 standard defines what the effect ought to be, and virtually every compiler on the market complies with the standard.

C. END DO statements are used in some of the new coding. Although not part of the F77 standard, this convenient extension is allowed in VMS Fortran and an increasing number of modern compilers. In other words, it is becoming standard practice *de facto.*

D. Tabs are used for aesthetic alignment, even in executable lines. Some systems treat tabs as single spaces, making some Fortran lines invalid. On other systems, like the Cray, tabs are unacceptable altogether. Should we need to port ELF to a Cray in the future, mechanical replacement of tabs is straightforward.

In addition to the two large ANALYZ runs, several small runs were made to test structural connectivity and internal consistency of modules. This "test by module" approach was especially useful in developing the INTernal Boundary Conditions (INTBC) module and the new ELFPLOT code described below.

The new ELFPLOT coding was tested extensively with the ANALYZ static FORTRAN source—code analyzer. This helped modularize the ELFPLOT code, and identified not only subtle coding errors but also the use of non—standard coding in

24

ELFPLOT. As a result, we are assured that the new ELFPLOT coding is not only free of language usage errors, but is also highly machine–transportable. We estimate that porting the new CGS–based ELFPLOT to any environment supported by CGS, such as Cray mainframes or Sun workstations, will take about 40 man–hours. Additionally, it should be possible to build an ELFPLOT program based on a totally new plotting primitives package (on a PC, for example) by replacing only the CGSCALLS module within about 80 man–hours.

5.2   USER–FRIENDLY I/O.

In anticipation of extensive testing of the ELF2 codes, a more user–friendly input/output technique developed by Tetra was implemented in the 2D ELF main program and the Tektronix 4010 version of ELFPLOT. Preliminary Beta–test user feedback was encouraging. The technique prompts the user with current (default) values for a group of related parameters in one–line tabular form; allowing him to enter changes only (under current values). The "changes only" technique is more efficient for both novice and experienced users. Some other modules requiring user i/o were changed to the same user–friendly format.

In addition, the ELFPLOT program was re–structured internally to group related plot types (surfaces, grid, functions vs. arc length, function contours). As a consequence, the new version has significant new capabilities. We now can plot any function in the output file, i.e. electric potential, power deposition, conductivity, temperature, or electron density, along any grid line (I = constant or J = constant) as a function of arc length. These changes will improve significantly the user's ability to examine the solution.

5.3   PLOTTING ELF SOLUTIONS.

Plotting has historically been a problem in the development of the ELF codes for various reasons. With any such code, plotting is the least transportable portion. Because the ELF technique intrinsically depends on arbitrarily stretched, non–regular grids, commercially available contour plotters do not apply. Those we are aware of assume regular, cartesian grids. Furthermore, the new capability to create cut–outs by "blanking" rectangular portions of the grid exacerbate the problem, making a custom plotting program a virtual necessity. The ELFPLOT code we have been using depends on the Tektronix PLOT 10 package running on a VAX under VMS, producing plots on a Tektronix 4010 graphics terminal emulator, with hard–copies made by a screen–dump to a dot–matrix or laser printer. While a laser printer output is crisper, the resolution was still limited by the emulator software. The resulting poor plots gave the incorrect impression that the calculations were not very accurate (see Figure 11). For all these reasons, we decided to make a concerted effort to develop high–quality graphical representations of the high–accuracy ELF solutions.

The first improvement came from use of a better graphics terminal emulator – SmarTerm 240 (Persoft, Inc., 465 Science Dr., Madison, WI. 53711). It provides for PC emulation of DEC VT220–340 terminals, including TEK401x–series graphics mode. More importantly, it provides hard–copy screen dumps with the full TEK–401x resolution, as seen in Figure 12.

Next we restructured the Tektronix PLOT10–based ELFPLOT to facilitate modifications, and expanded some of the capabilities. The new structure uses a Modular LOADSLN subroutine to load a solution (from a file written by the

25

companion SAVESLN subroutine called by the ELF program). From the main ELFPLOT menu, the user chooses one of four plot types, i.e., surfaces, grid, contours or function vs arc–length. For the latter two types, he chooses one of the solution functions (potential, E–magnitude, electron density, conductivity, temperature, power density and two new choices: Ex or Ey). The code for each plot type is a separate module. Finally, all PLOT10–specific coding was separated, except for certain parameter choices peculiar to PLOT10. Additional options now include: (1) some axis control which is important to avoid aspect ratio distortion for the first three plot types, (2) grid thinning for grid plots, (3) a log–Z scale for contour plots (see Figure 13), and (4) actual vs normalized arc–length in the fourth plot type. In addition, default labeling is more centralized, to minimize repetitive user changes. Most importantly, the basic algorithms and data structure were modified to accommodate the new "blanking" option (see Figure 14 for an example). All these new capabilities have been thoroughly tested.

In order to explore the use of color on screen and grey scales on hard copy, we modified ELFPLOT to optionally output plot data in a form readable by the PC–based GRAFTOOL program (3–D Visions Corp., 412 S. Pacific Coast Highway, Second Floor, Redondo Beach, CA 90277). This allowed us to experiment with the use of color and 3D to enhance solution plots, and even vector plots. This is not viewed as a replacement for the main ELFPLOT technique, since GRAFTOOL is slow to use, and not transportable to mainframes. However, the vector–based technique could be extended to produce CAD–readable files, so solution contour plots for example, could be plotted by CAD right on the design drawings, and perhaps even in 3D perspectives.

After much experimentation with use of color and 3D surfaces to visualize 2D solutions, we opted for a simpler approach, based on Los Alamos National Laboratory's Common Graphics System (CGS). It is public–domain software fully supported by LANL, and transportable across all computers and output devices supported by LANL today, and for future expansion work. We got all the documentation from LANL and designed and coded the new interface module, between ELF–specific coding and calls to CGS routines. Upon this CGSCALLS module which contains all calls to CGS routines, we built modified modules for the four plot types, and debugged the whole new ELFPLOT code in short order, demonstrating the soundness of this modular approach. In the future, changing to another package of plot primitives, such as DISSPLA, NCAR or even a PC–based system, could be accomplished by replacing only the CGSCALLS module. The CGS–based ELFPLOT code has all the significant capabilities of the PLOT10–based code, plus some new capabilities. Perhaps the most important is the option to write graphs to a metafile, from which LANL post–processors can produce full color slides, vu–graphs and prints as hard–copy output, some examples of which are used in Section 7, below. There are some significant limitations which include no true 3D capabilities and no true PC operating mode. However, CGS gave us more control over such things as axis ticking. The resulting ELFPLOT code is now considered the primary tool for graphically examining ELF solutions, although the PLOT10–based ELFPLOT is also retained for archival purposes.

26
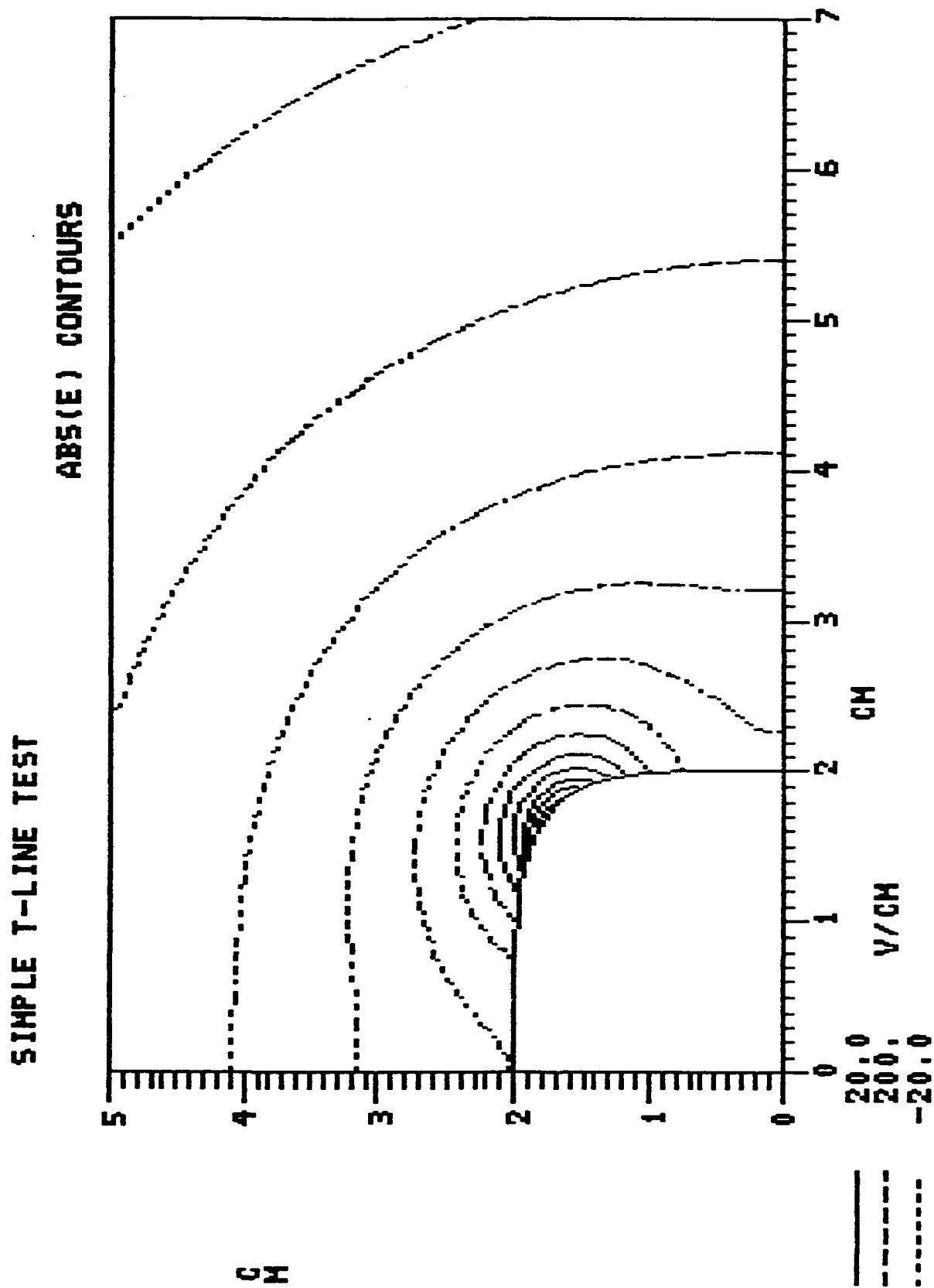
Figure 11. Sample plot at "CGA" resolution.

abs(E) contours
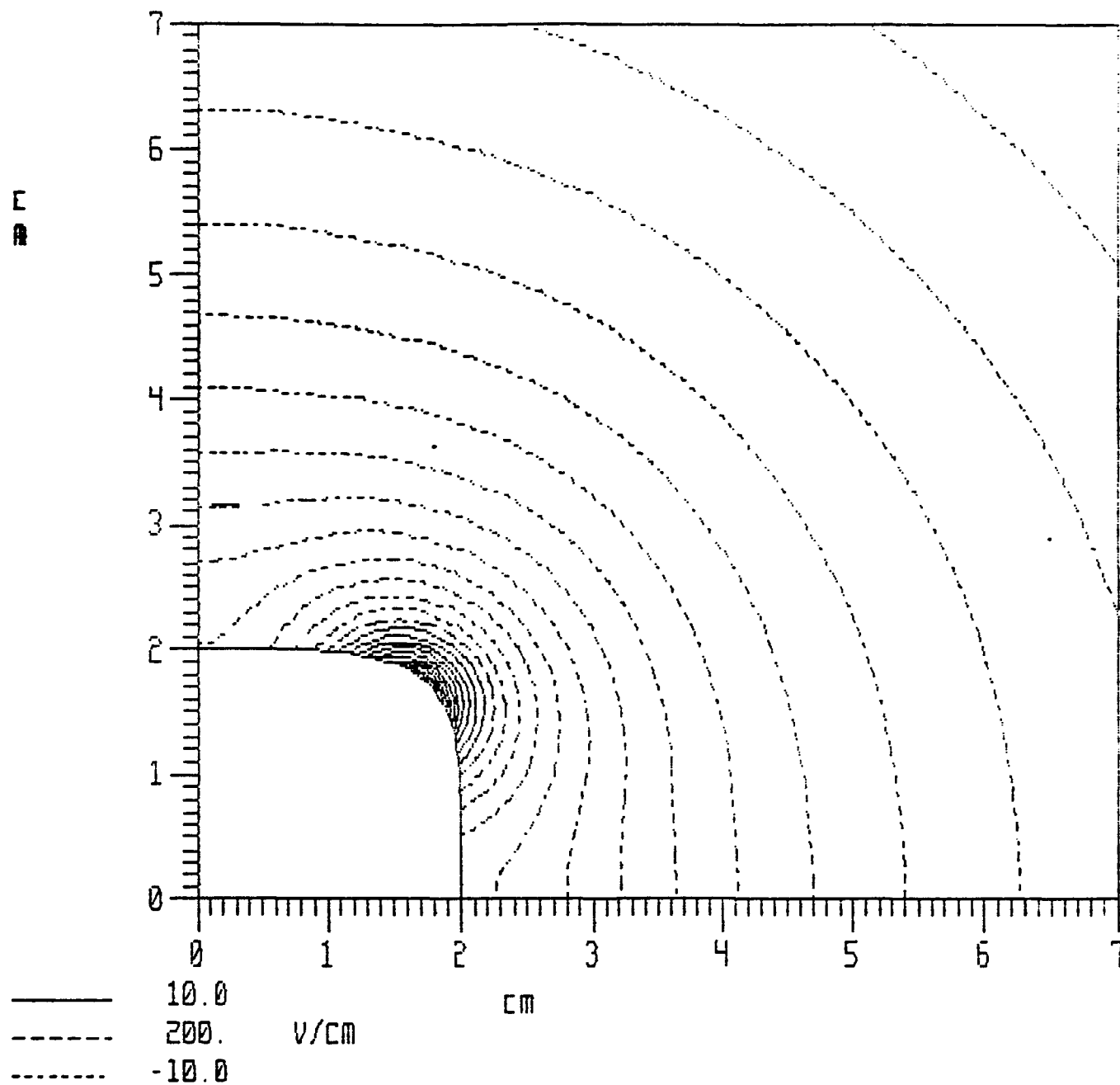
Figure 12. Sample plot at full TEK–4010 resolution.

SPHERE in VACUUM
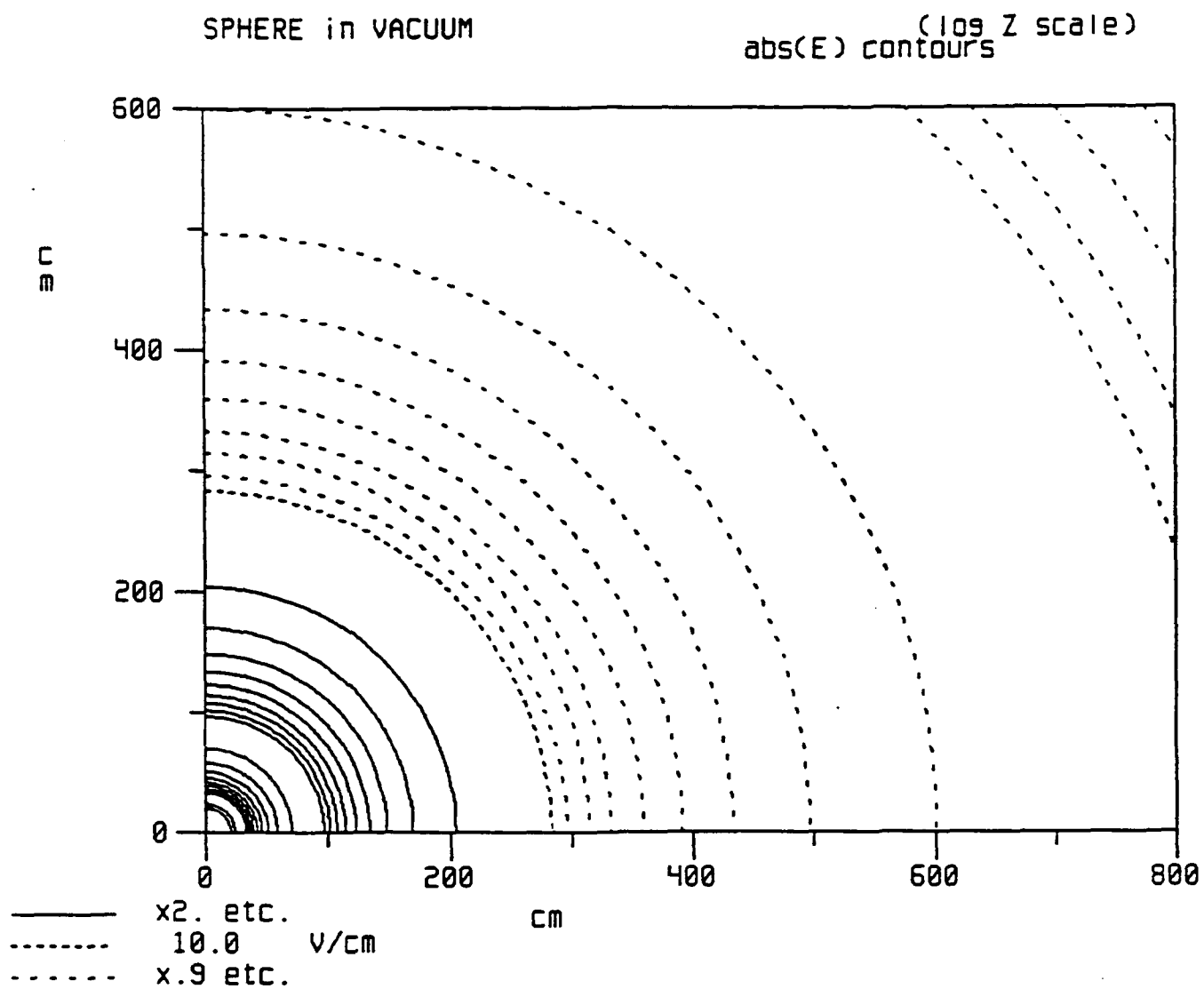
abs(E) contours (log Z scale)

x2. etc.

10.0   V/cm

x.9 etc.

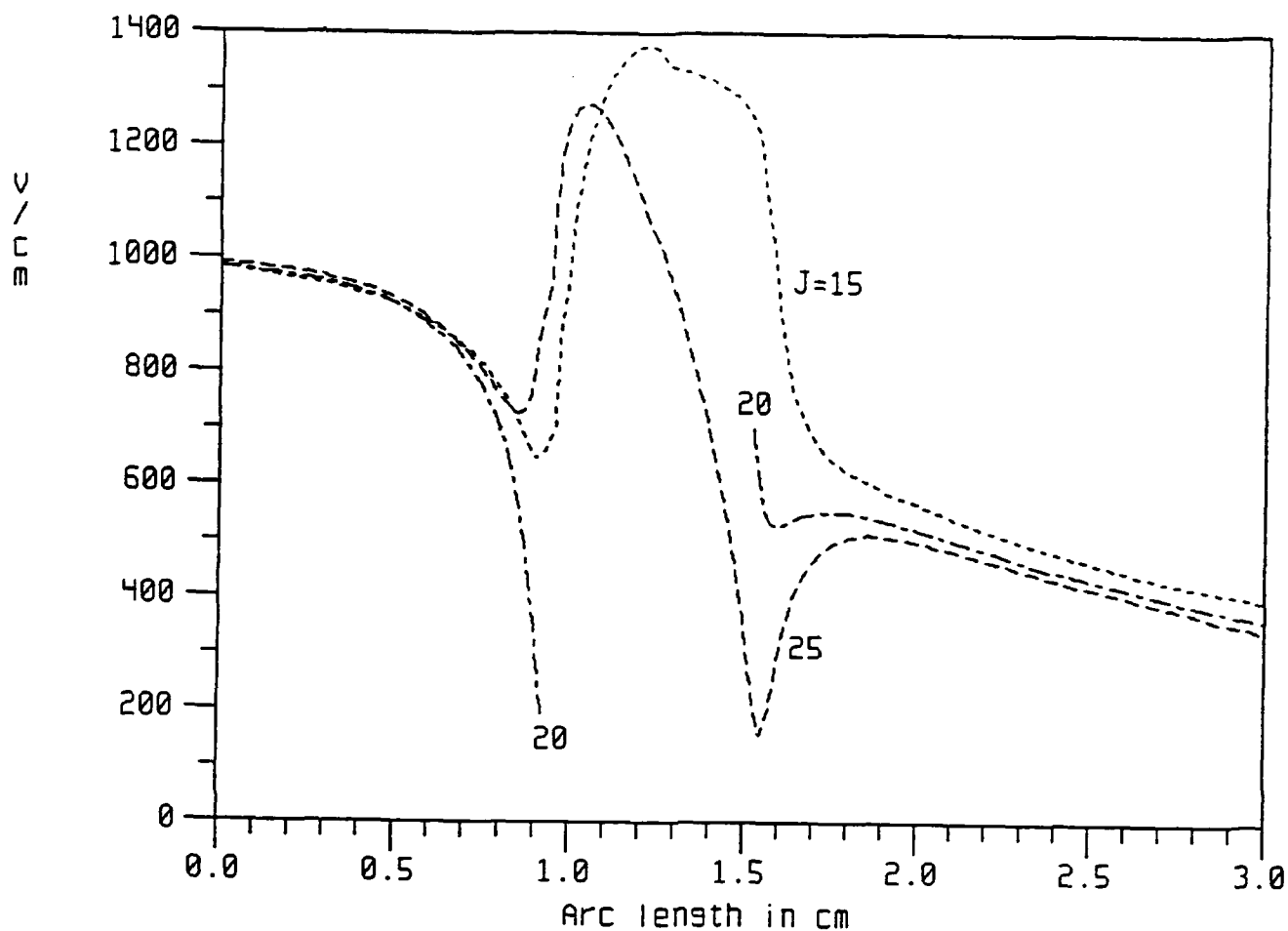Figure 13. Illustration of log–Z scale option.

Figure 14. Sample E as arc length plot showing a grid line (J=20) interrupted by a blanked area.

SECTION 6
DEMONSTRATION FIELD ANALYSES

6.1   SPEAR III.

The development of any large code like ELF is guided in practice by specific needs or requirements of real problems. In order to insure that the next—generation ELF codes would be responsive to real needs of the pulsed power community working on SDI research, we needed a model problem, or paradigm. We chose the SPEAR third launch payload. The general layout is illustrated in Figure 15. We chose to concentrate on the main experiment at the top of the figure, which is essentially a large Langmuir plasma probe.

The field analysis was divided into two scale sizes: a "big picture" and a "close look". The big picture simulated the plasma sheath which would form when up to 45 kV are applied to the 20 cm gold—plated sphere at the end of the support boom. One—dimensional analyses of the equivalent spherical symmetry problem demonstrated that the field distribution would not significantly differ from vacuum solutions except within a few cm of the sheath edge (see Section 4). Therefore, we ignored space—charge effects inside the sheath, and merely imposed zero voltage on a far—field boundary of approximately the correct size and shape. That shape is distorted from spherical into a cardioid shape by the voltage distribution imposed by the voltage grading structure on the support boom. That grading structure assures linear grading from the current—collecting sphere to a physically fixed point connected to spacecraft ground.

Thus, the boundary conditions for the "big picture" field analysis were as follows: 1) On the axis representing the idealized boom, a linearly graded voltage is imposed. 2) On the cardiod outer boundary, zero voltage is imposed. 3) On the current collecting sphere, full voltage is applied (nominally 45 kV). 4) On the axis of rotation on the other side from the boom, a symmetry condition is imposed (zero normal gradient). The challenge was the large difference in scale size between the sheath edge and the current—collecting sphere. That challenge was met with a new grid—generation method which conserves grid stretching imposed on the grid boundary nodes. The big picture solution is illustrated in Figure 16, which shows color—coded equipotentials. Unfortunately the quality of the Iris display eroded in transferrine the screen image to a color printer, and eroded even further by transferring .o olack and white. A close—up of the region around the sphere is shown in Figure 17. The white circle represents the sphere chosen as the outer boundary for the "close look" analysis.

The "close look" analysis examines the effect of the fine structure of the boom voltage—grading bushing on the electric field. A visual examination of the design, shown in Figure 18, shows that enhancements are to be expected at the ring edges, where a small radius of curvature is found. The highly re—entrant geometry of the rings was idealized in the cavities, since the primary interest was in the enhancements. Figure 19 shows the boundary geometry in physical space, and the mapping to the computational space with grid cut—outs.

The challenge with the close look analysis was to maintain the smoothness of the grid, so sudden changes in cell size would not distort the solution. In that regard, control lines, shown as dashed lines in Figure 20, were invaluable. The final resulting grid is shown in Figure 21a and b.

31

The boundary conditions were all of the specified–voltage (Dirichlet) type. Voltage grading beyond the second bushing ring was idealized, but the two rings modeled geometrically are at the correct voltages. The outer boundaries are at fixed voltage distributions obtained by bi–linear interpolation from the "big picture" solution.

The resulting field solutions are illustrated in Figure 22a and b. It shows contours of E–magnitude (not E–vector lines) over the computational grid in a close–up of the area near the rings. On the Iris full–color screen, the grid is in a subdued grey, and the contour lines in bright colors. The main field enhancements are at the ring rounded edges between rings, as expected.

6.2   FLOATING BODY.

A second problem used to demonstrate the power of the new ELF flexible topology capability in both 2D and 3D was the "floating body" test case. The original ELF paradigm assumes (only) two electrodes, mapped to opposing grid boundary surfaces (nominally 1 and 2), with orthogonal boundaries (surfaces 3 and 4) normally being symmetry or far–field boundaries. To review, the topological relationship of the boundaries is illustrated in Figure 23.

A true floating body would not touch any of the outer boundaries. The new ELF capability to blank out any selected area(s) of the grid was used to create a rectangular cut–out of logical space, which maps to an elliptical floating body. By imposing a fixed voltage on all nodes along the interior boundaries, the floating body simulates a cross–section through a long, rounded electrode between the main electrodes. Surface number 1 is a plane electrode, and surface number 2 is a Rogowski electrode. The logical plane relationship is shown in Figure 24. The mapping to physical space can be visualized in the plot of the computational grid in Figure 25.

The 2D solution field distributions are shown in Figures 26 and 27. The features to notice are the E–magnitude maxima on the top and bottom of the floating electrode, and the minima on the right and left. These are proper and expected features. It should be pointed out that the choice of the positions corresponding to the corners of the logical grid cut–out box, and the stretching of the grid to keep grid lines from pulling away from the floating body were carefully studied. Poor choices could result in poor grids with inadequate resolution in key areas, resulting in distortions of the solution. With the greater power of the new ELF capability to blank out areas of the grid comes greater responsibility on the part of the user to make wise choices.

When the grid "blanking" capability was extended to 3D, it was demonstrated with a 3D analogue of the 2D floating body test case. In essence, the 2D geometry was extended in the Z direction, like an extrusion, and then swept through a 90° rotation using surface number 3 as the axis of rotation. The result is that the floating body looks somewhat like a candy cane, and the outer boundaries resemble Figure 28. The E–field 3D solution is essentially the same as the 2D solutions for cross–sectional cuts anywhere along the linear extrusion. In the rotated region, the additional curvature in the other direction produced localized maxima on the "candy cane handle" surface. Unfortunately, we have no mechanism to make hard copies of the striking 3D full–color graphics used to examine the 3D solutions on the Iris workstation. The Reduced Instruction Set Computer (RISC) architecture makes it possible to animate 3D color views, giving

the illusion that the viewer is "flying" around the 3D object. This is a powerful 3D solution visualization technique. Unfortunately it is highly machine—dependent, and generalization of the technique is not within the ELF2 contract scope.
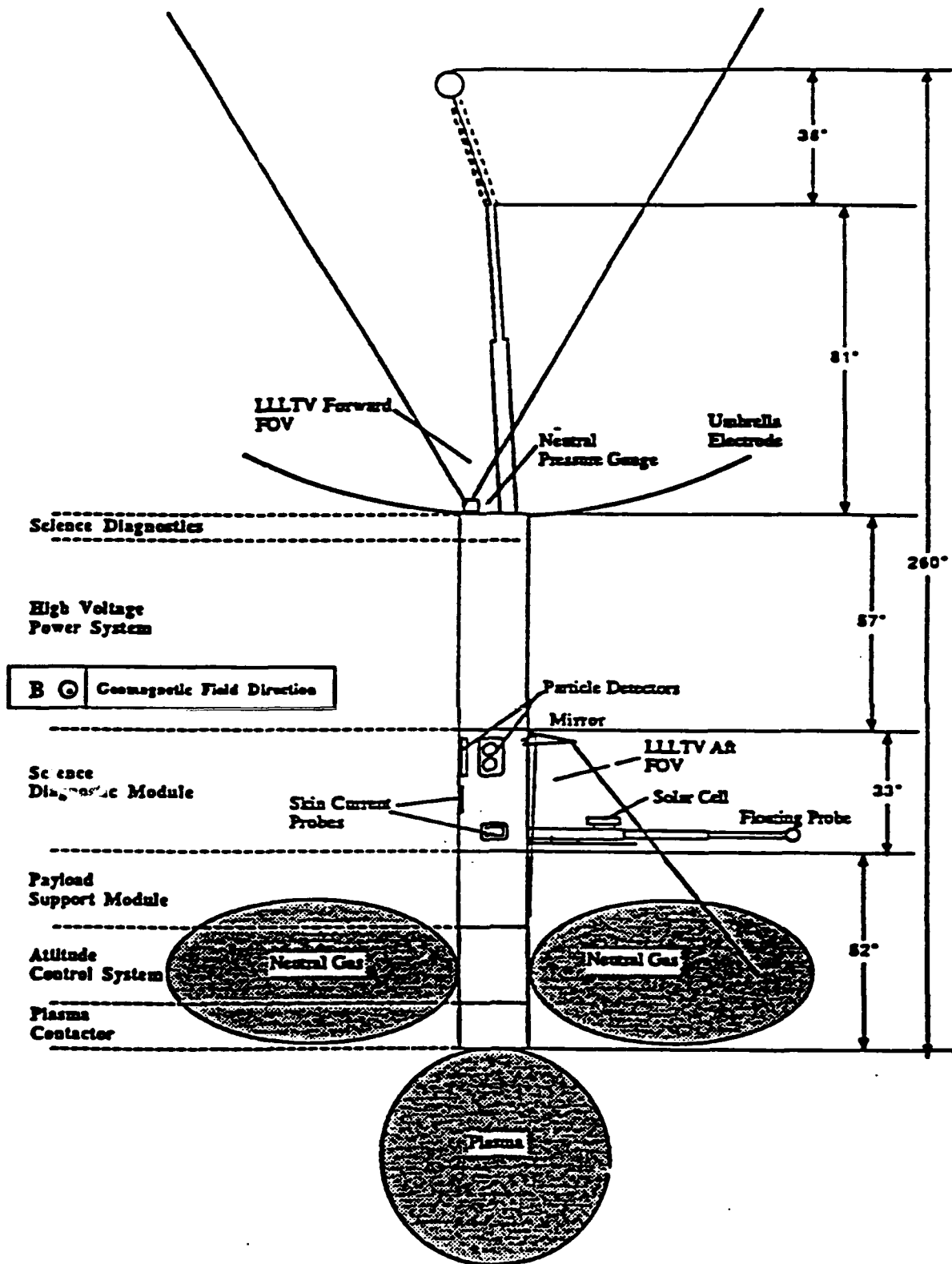
Figure 15. Conceptual diagram of SPEAR III payload configuration and orientation.
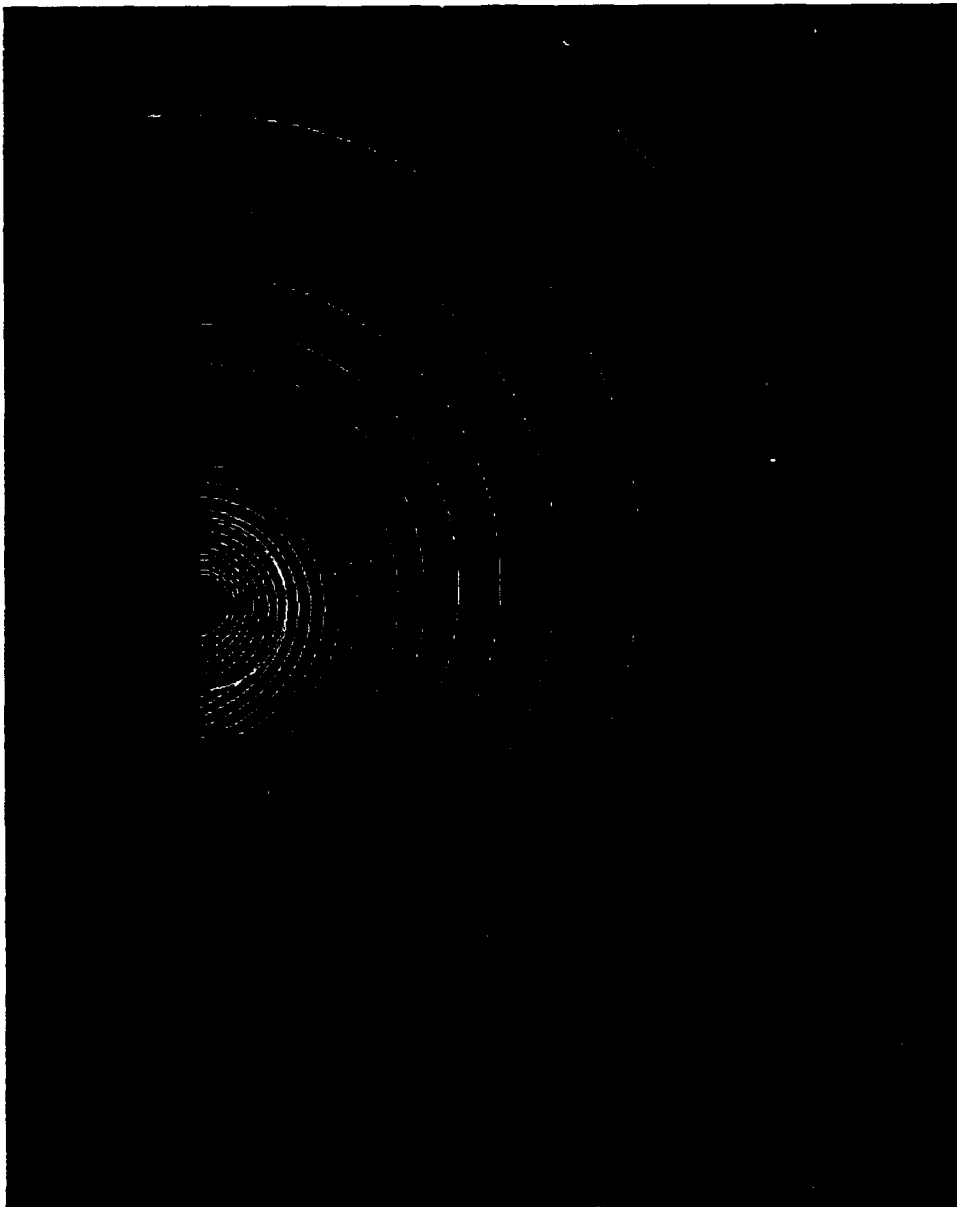
Figure 16. "Big Picture" solution equipotentials, showing cardioid–shaped outer boundary.
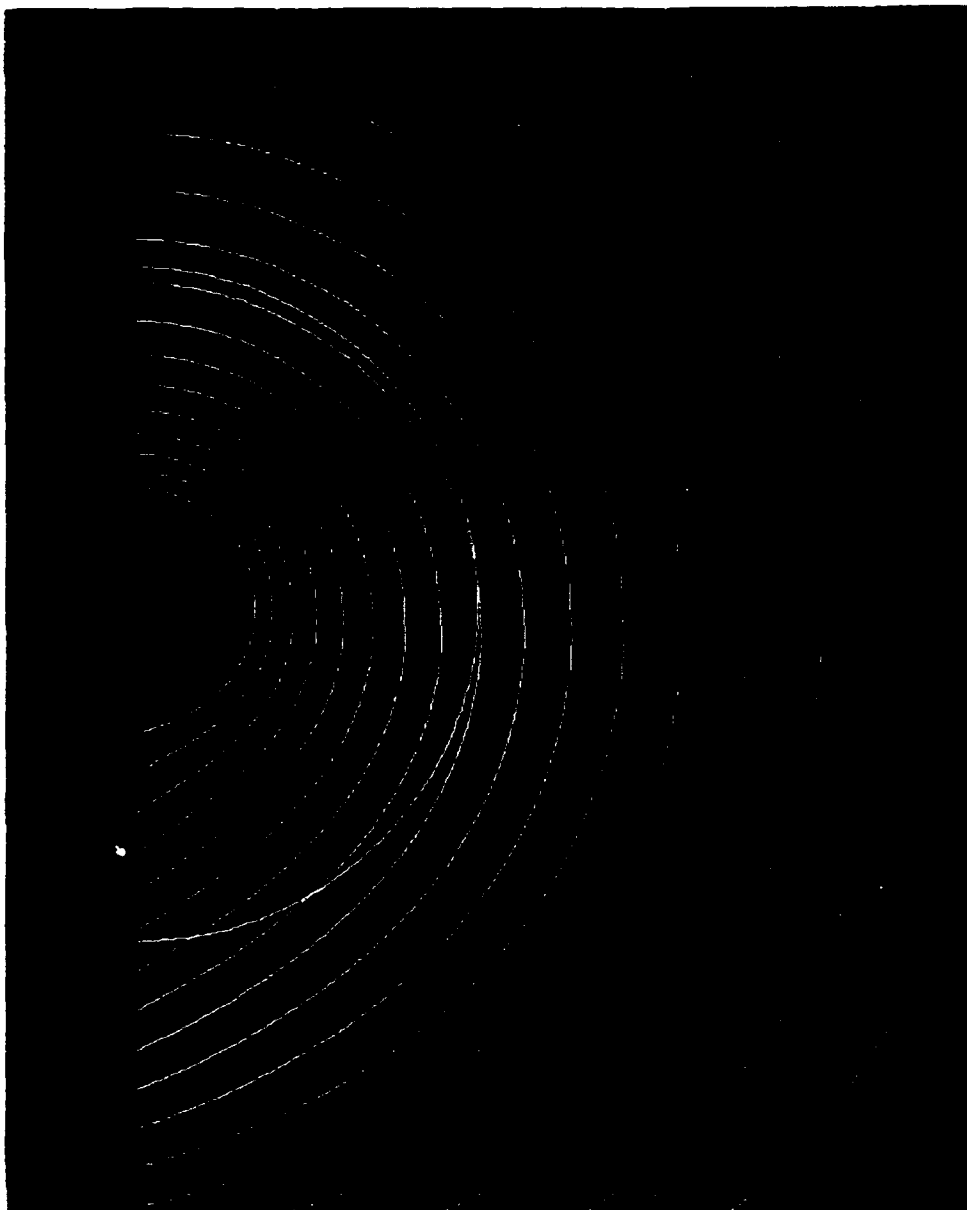
Figure 17. Close–up of "Big Picture" solution, with close–look
outer boundary inserted.

36

Collected Current

7.874″ dia.

50 kV

Enhanced E-field

ΔV

ΔV

ΔV

ΔV
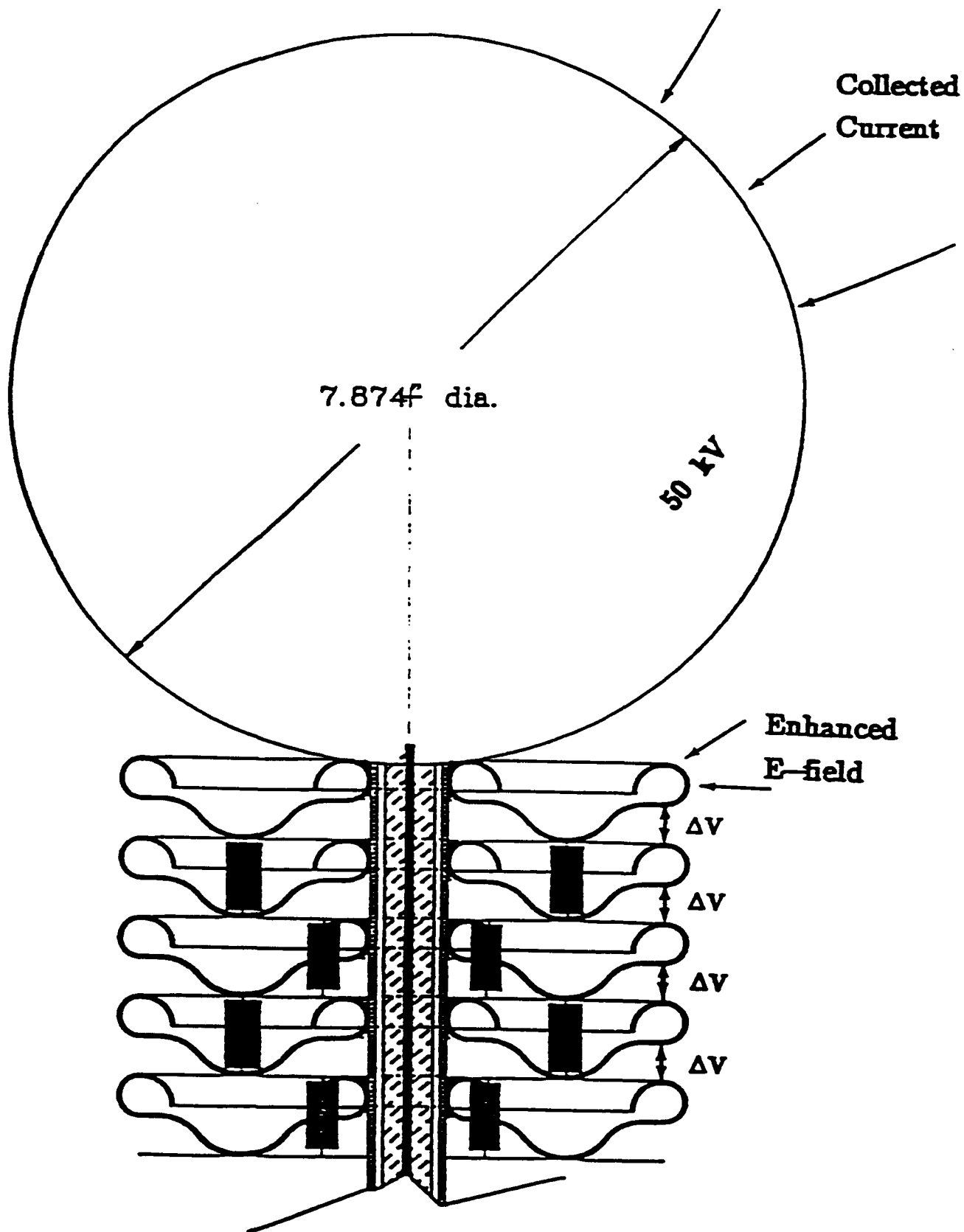
Figure 18. Close–look ELF analysis to determine current collected by first ring.

a) Computational Space
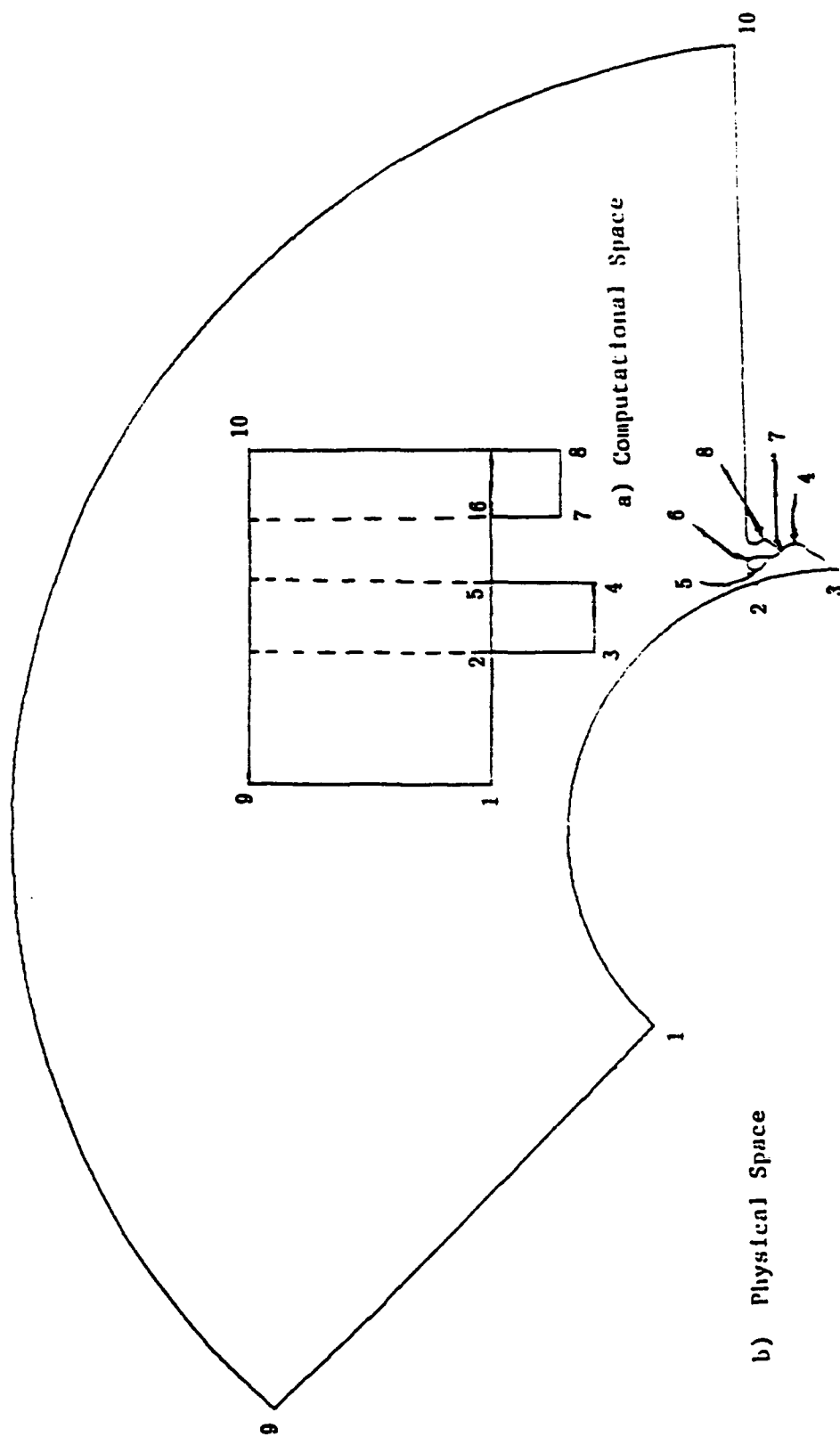
b) Physical Space

Figure 19. Physical space boundaries compared to Logical space topology with cut-outs.

a. Large View

b. Close—up of rings.
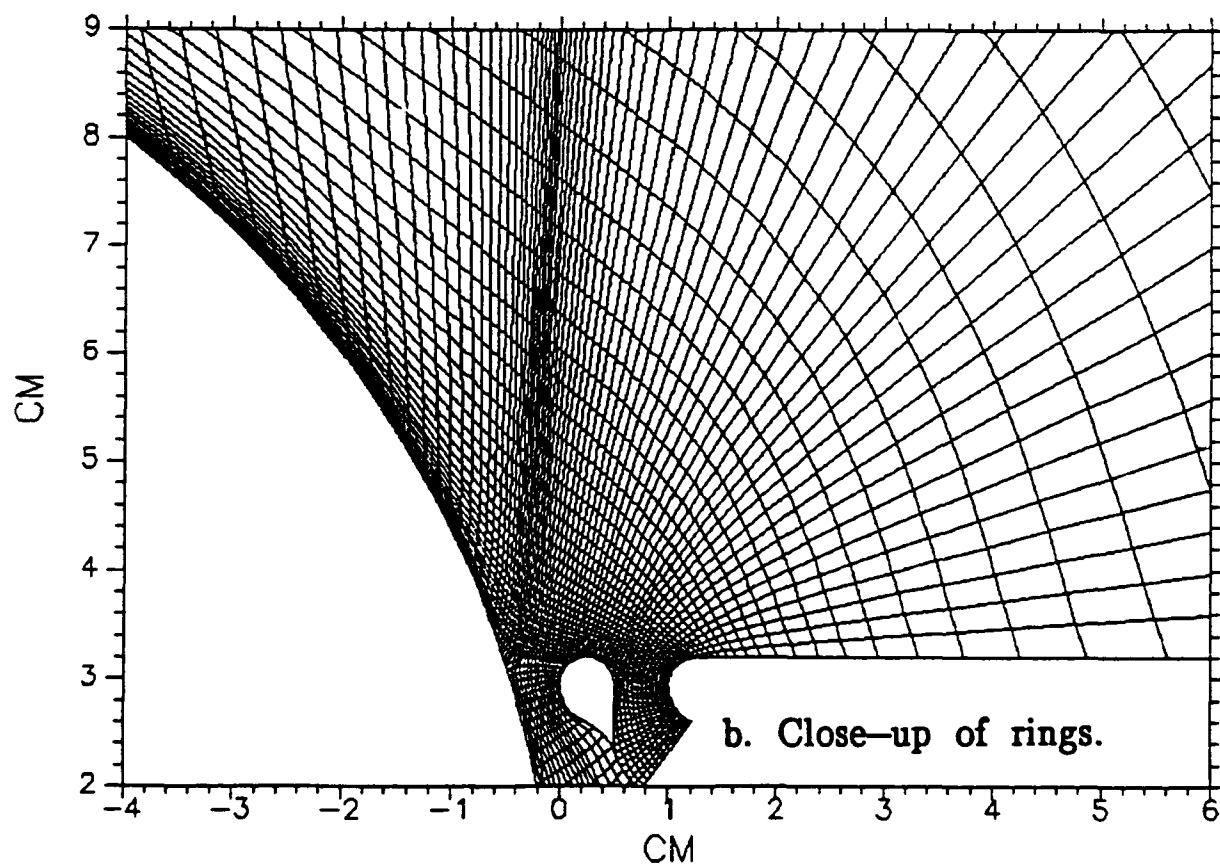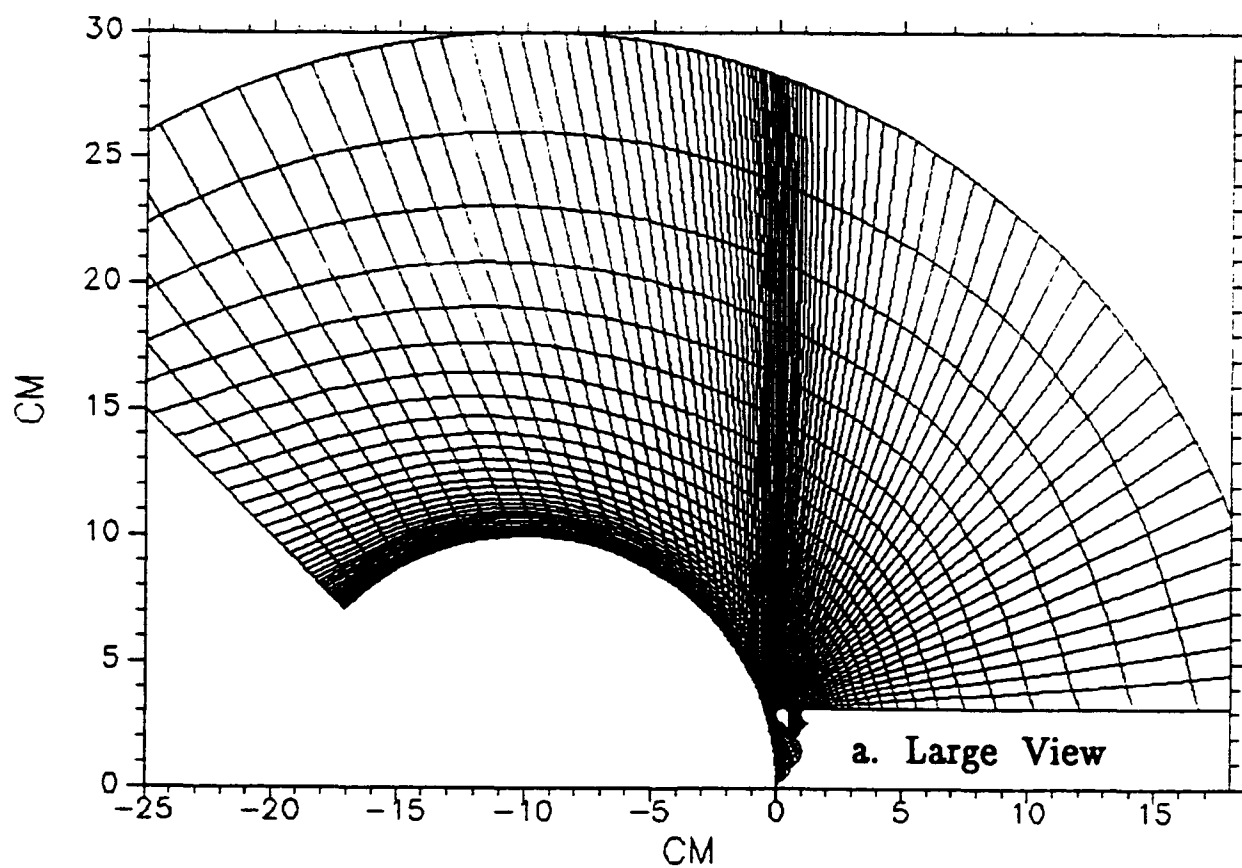
Figure 20. Final computational grid for close—look problem.
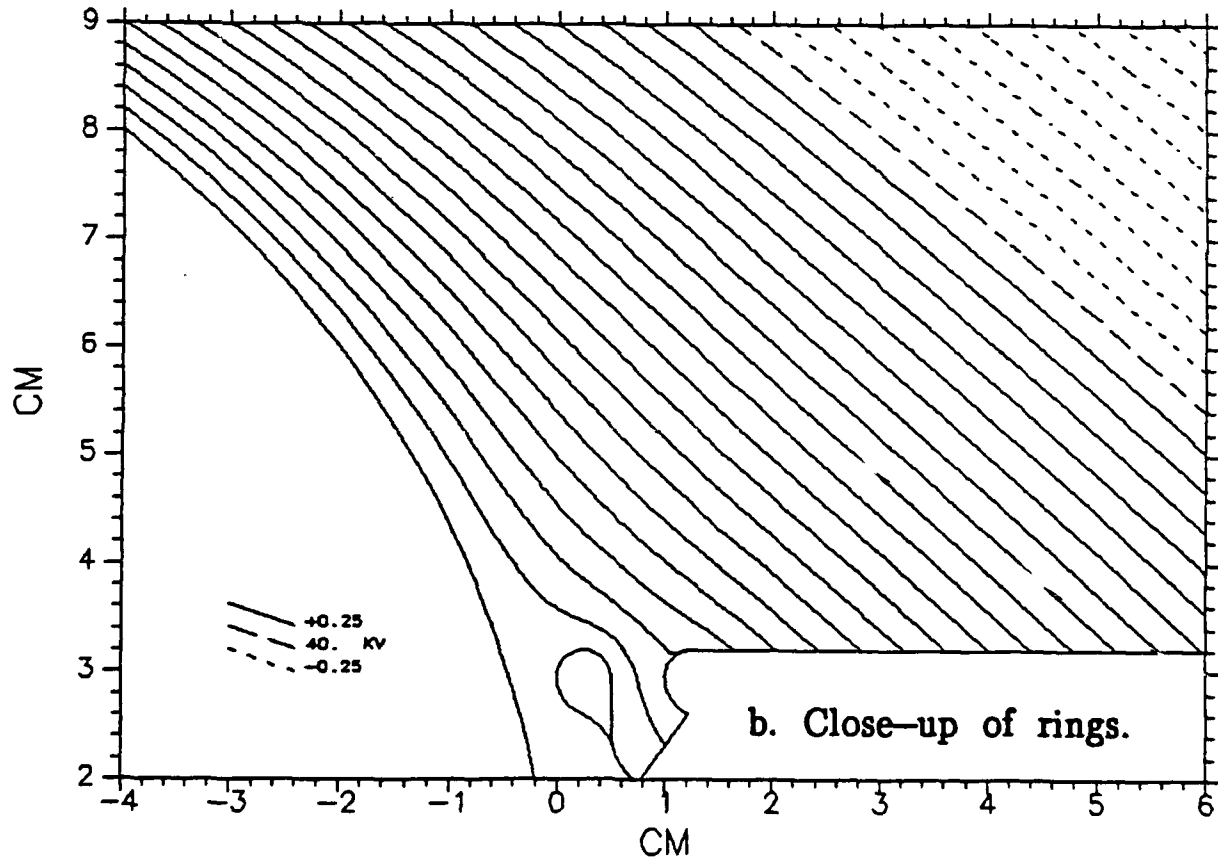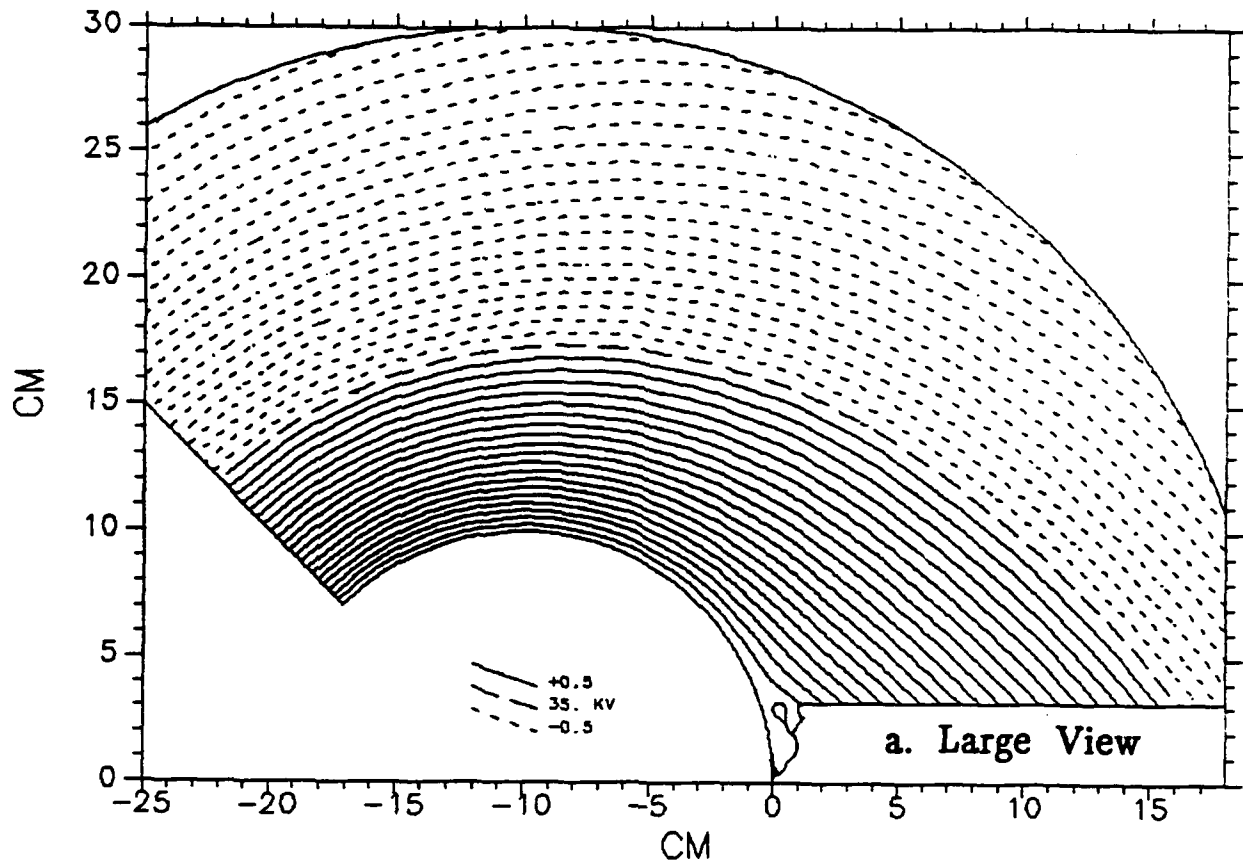
Figure 21. Close look solution equipotentials.
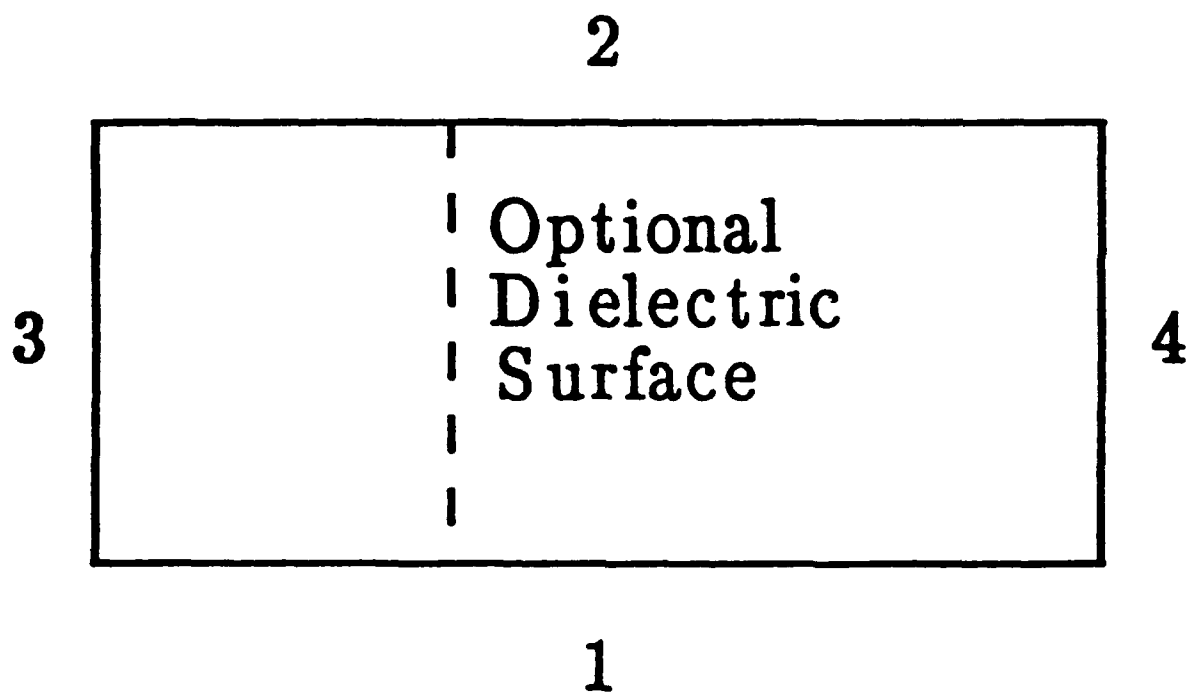
Figure 22. Topological relationship of nominal grid boundaries.
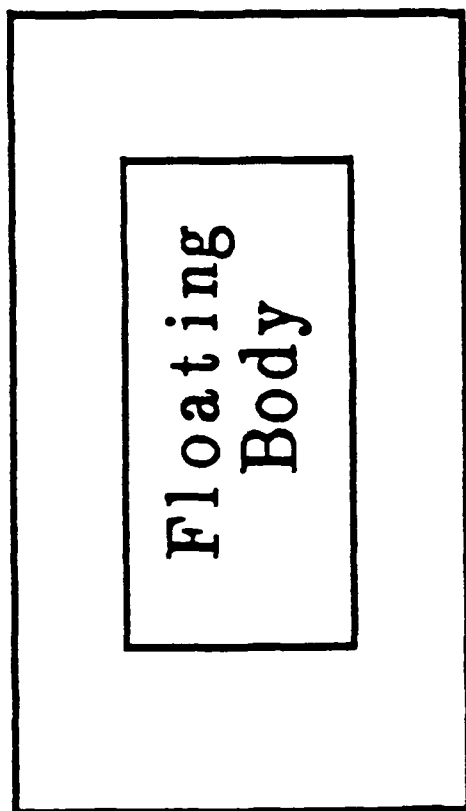
Figure 23. Topology of floating body test case.

ABS(E) CONTOURS

a. Large View

b. Close-up of rings.
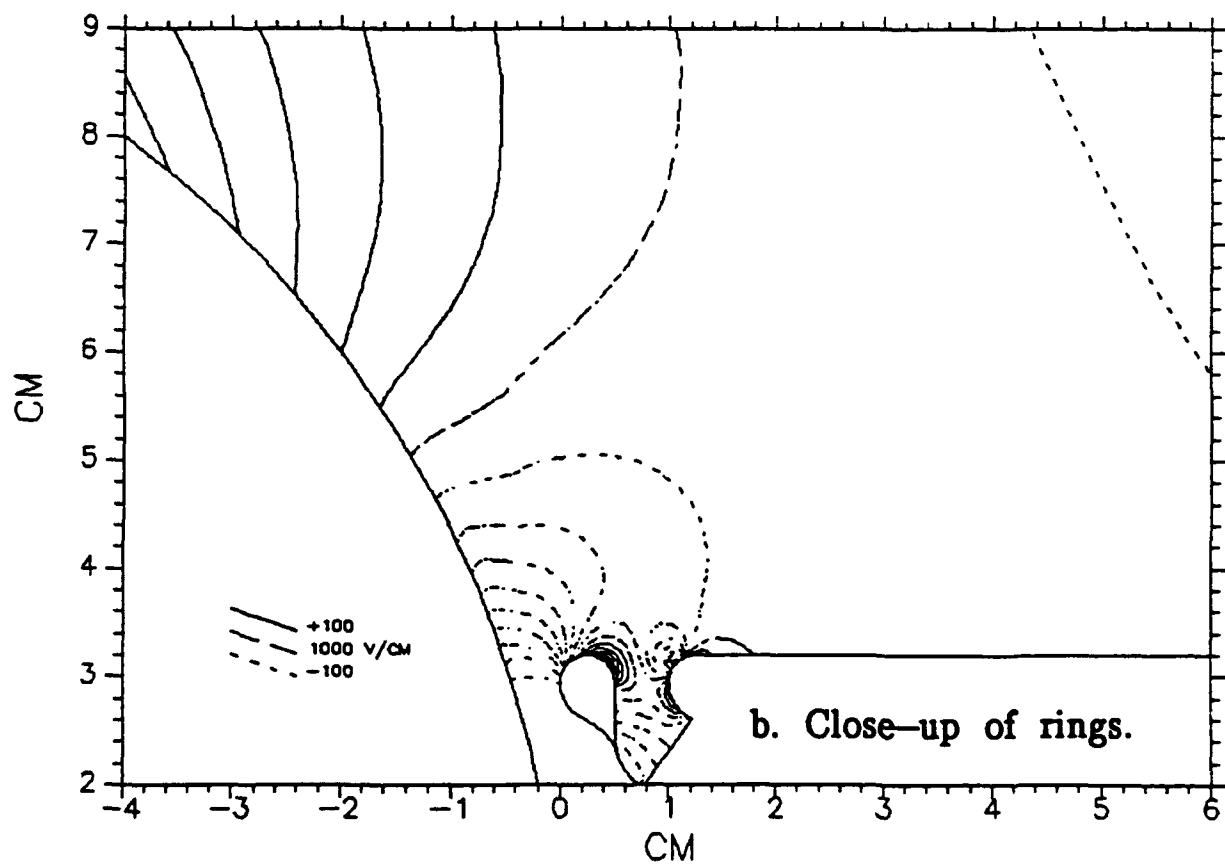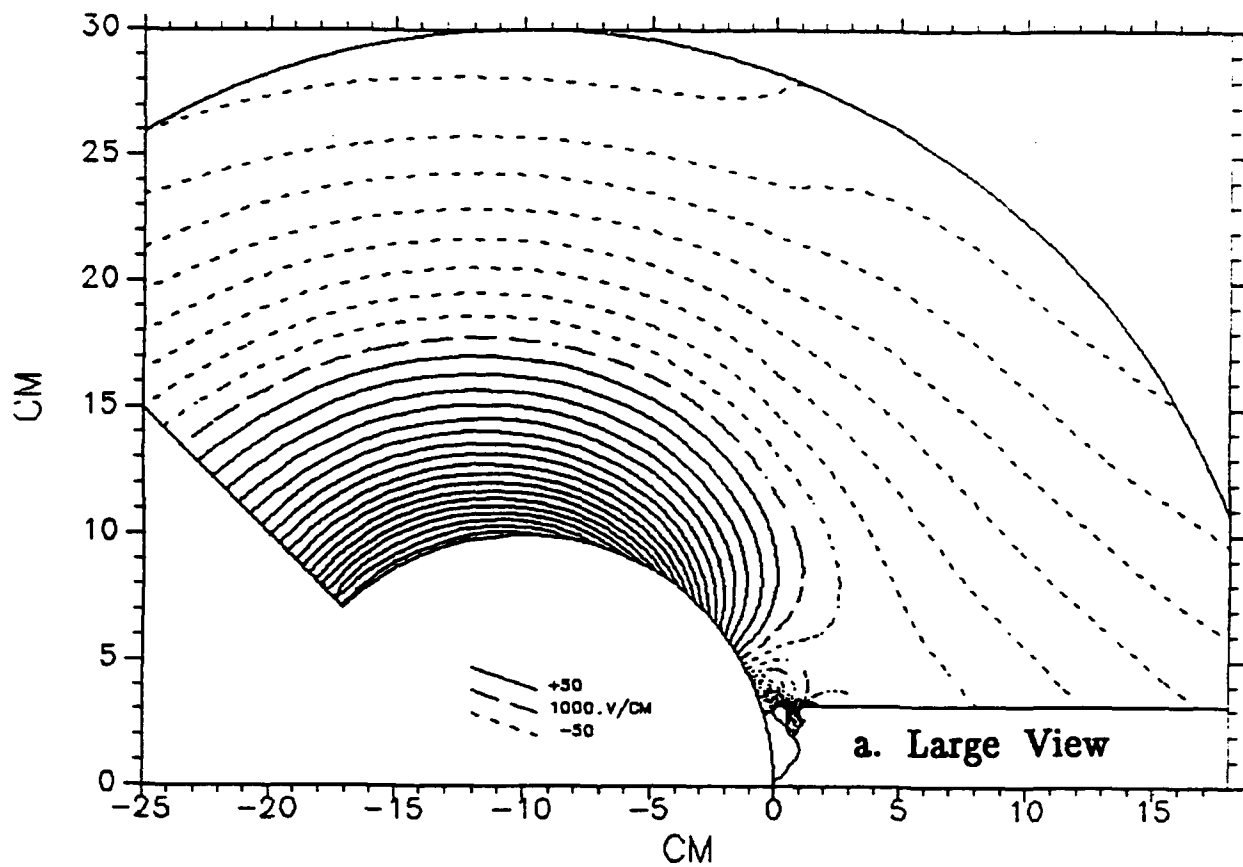
Figure 24. Close look solution E-magnitude.
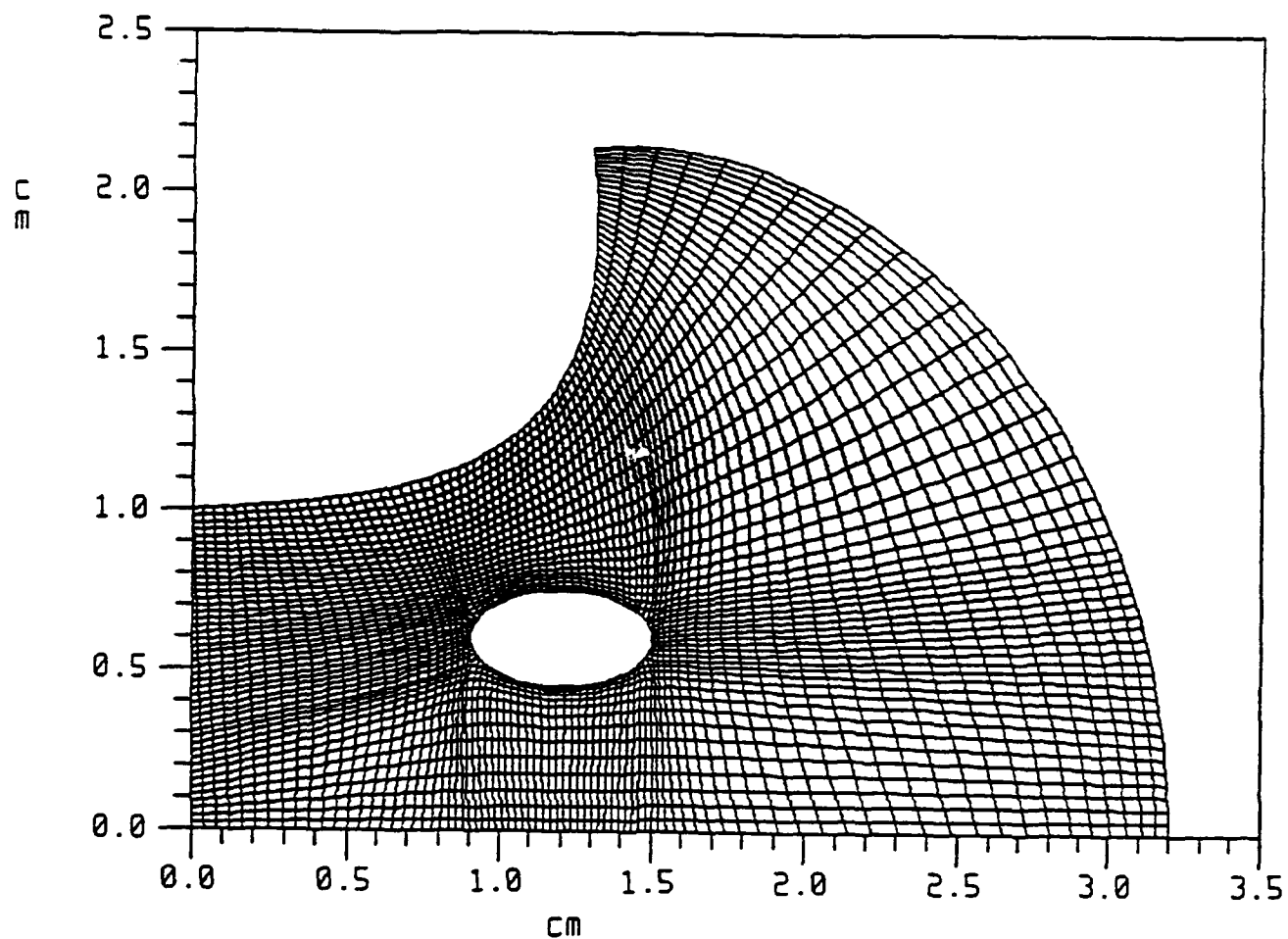
Figure 25. Floating body computational grid, showing blanked out area.

POTENTIAL CONTOURS
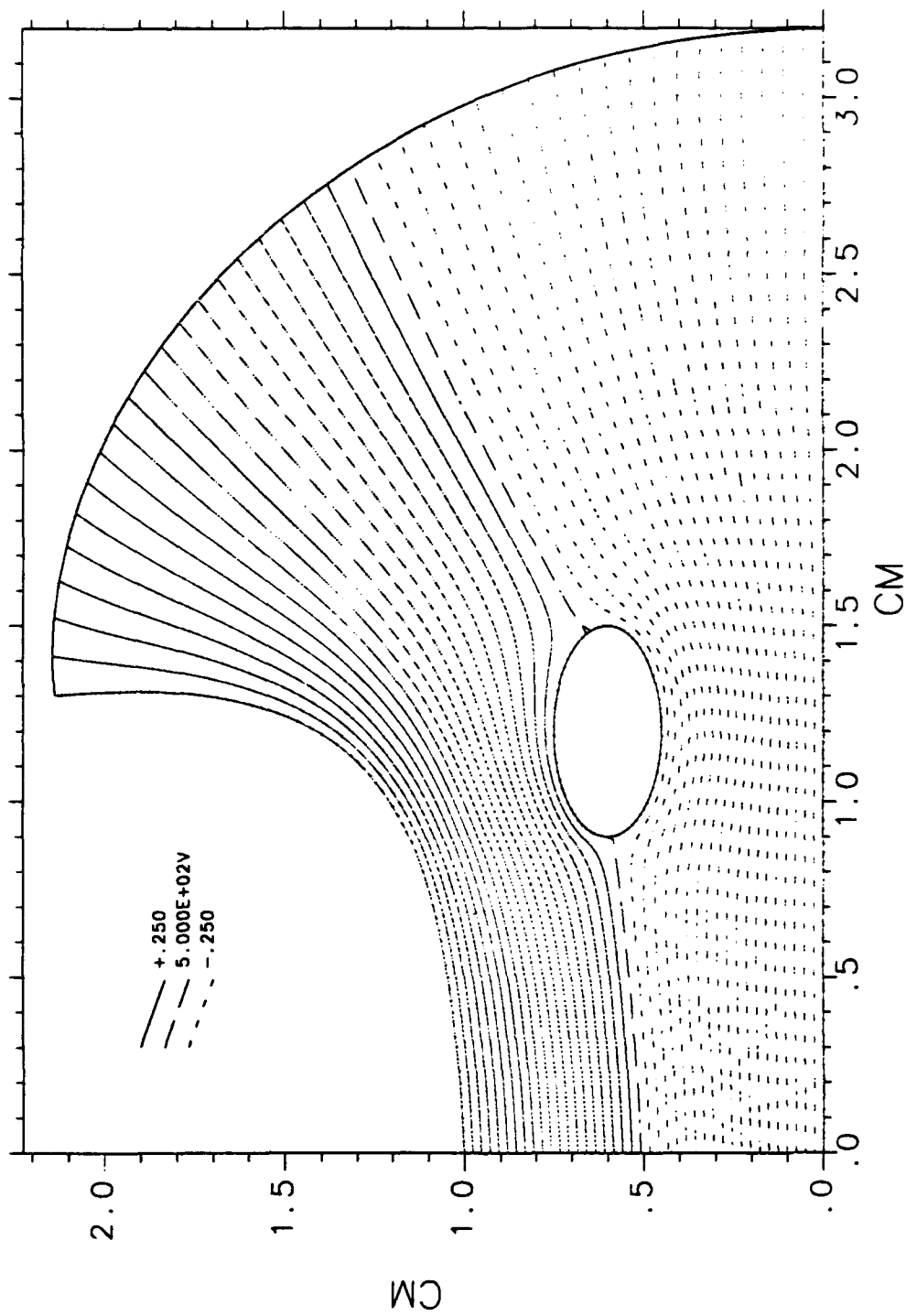
Figure 26. Floating body equipotentials.

45

ABS(E) CONTOURS

+ .050
1.000E+03V/CM
– .050

CM

CM
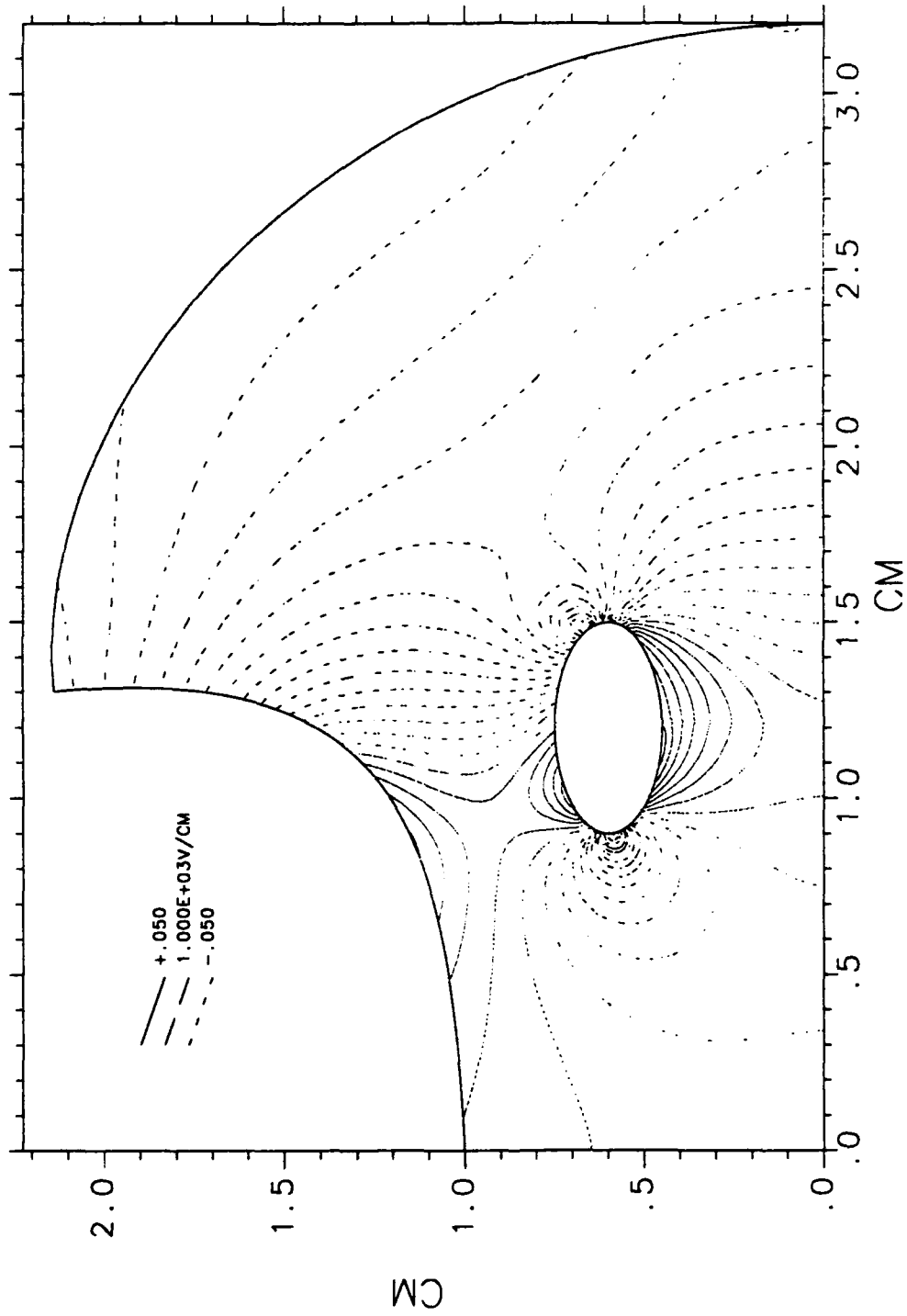
Figure 27. Floating body E-magnitude.

46
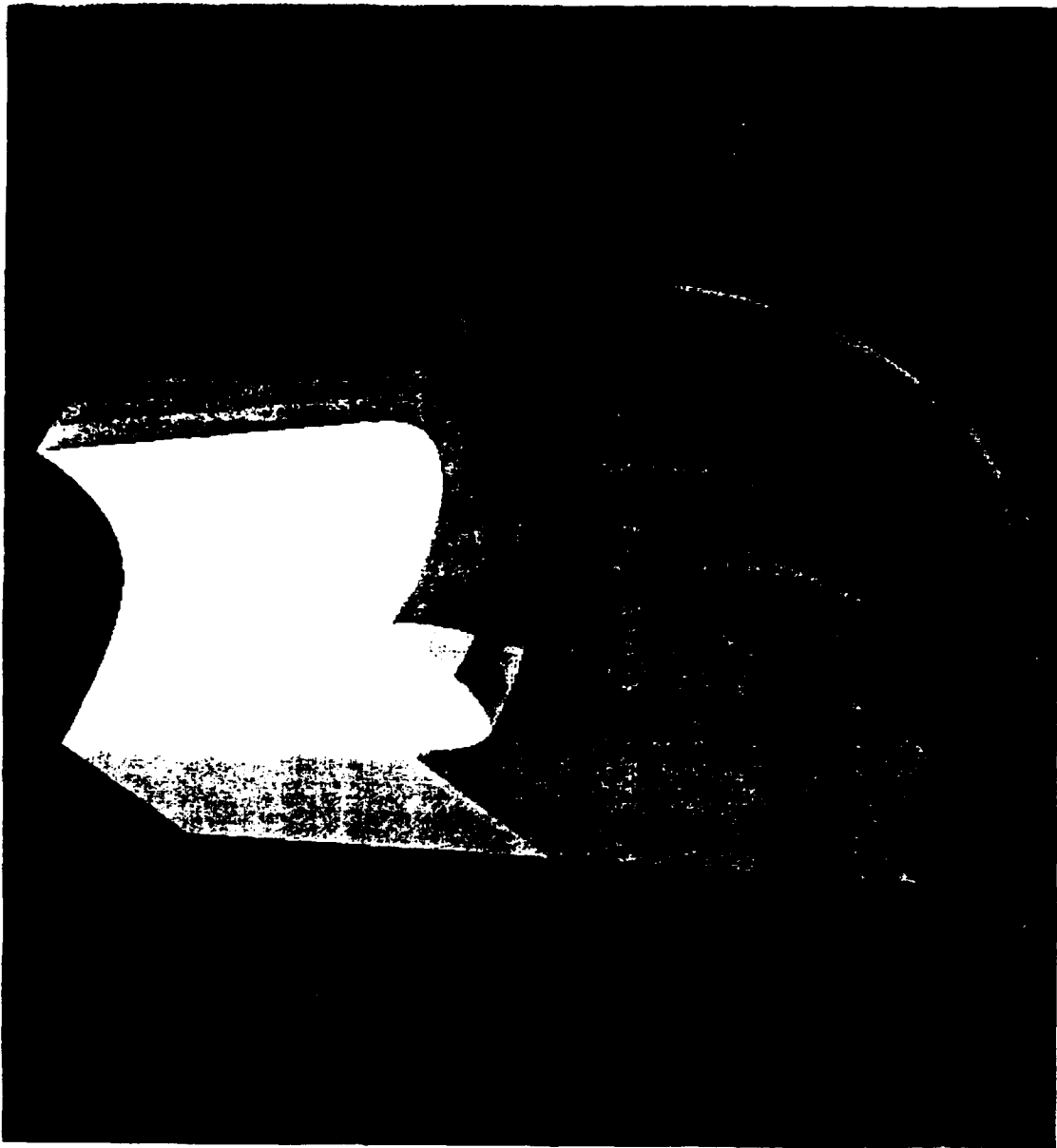
Figure 28. 3–D geometry generated by linear extrusion and 90· rotation.

SECTION 7
CONCLUSIONS AND RECOMMENDATIONS

7.1 ACCOMPLISHMENTS AND STATUS.

There are three specific accomplishments which can be considered noteworthy and one with mixed results. There also are limitations to the resulting new—generation ELF2 codes. In Section 8.1, we summarize the good, the bad, and the mediocre. In Section 8.2, we discuss recommended follow—on development to address the ELF2 code limitations.

The first significant development was the new grid generator. The ability to blank out selected portions of the grid provides a significant topological flexibility. This is an unexpected bonus. Our original plan was merely to extend the Phase I topology to a couple of variations. This new capability significantly exceeds that minimum requirement by giving the user the power to customize the grid topology to match the physical geometry. This is invaluable in dealing with complex geometries like the highly re—entrant bushing rings or floating bodies. In addition, the new (Thomas—Middlecof) grid generation algorithm's ability to conserve the boundary nodes' stretching characteristics is invaluable in handling situations where there is a great difference in scale—sizes of interest.

The second noteworthy success was in the area of user—friendly input, especially the new geometry input technique developed. The instructions—driven approach makes it possible for non—Fortran—literate users to build complex geometries from single elements (straight lines, ellipses, superellipses and distorted "quadrants"). The possible combinations are literally limitless, and other elementary shapes could easily be added to the "menu" by any competent Fortran programmer. Certain "exotic" shapes, such as blending of a sinusoidal "bump" on a superellipse, will require a Fortran—literate user to modify sample geometry routines. It should be noted that this new technique does not relieve the requirement that the user must be competent in the practice of analytical geometry. It only relieves him of the requirement of being Fortran literate. In addition, the general implementation of a "changes—only" input technique will significantly improve interactive input and the new user's learning curve. The succinct, plain—English prompts are not the same as extensive multi—level help utilities, but they are a step above mnemonic, but often cryptic, variable names. For example, "Axis of revolution = X, Y or 0 (neither)" is better than "MCYL = 0 for planar, 1 for axisymetric or 2 for radial". Furthermore, the coding is transportable, unlike pop—up menus, pull—down windows and other graphical input techniques. A significant degree of modularity was implemented, which will facilitate development of a batch mode in the future.

The third area of success was in output, specifically the plotting of solutions. As with input, greater weight was given to code transportability than to maximum aesthetic impact. That drove our choice of the public—domain Common Graphics System developed and maintained by the Los Alamos National Laboratory. The optional use of color makes it useful in interpreting graphical results, but not indispensable or required. Furthermore, the great degree of modularity implemented in the restructured coding will greatly simplify the task of adapting the ELFPLOT code to new graphics packages and environments in the future.

Mixed results are attributed to the space—charge—driven E—solver developed for the Low Earth Orbit plasma sheath problem. Our 1—D analysis of the physics led to a minor improvement in the methodology used in the NASCAP/LEO codes, but it

48

also showed that it makes little difference to fields near the current collector. The problems associated with locating the sheath edge within the ELF finite–differences structure were beyond the ELF2 scope, but not because the plasma physics nonlinearities could not be handled by the ELF numerics. A solution strategy was identified, but pragmatism caused us to continue with a vacuum analysis of the SPEAR III fine details.

With every increase in the power of a complex code like ELF comes increased responsibility for the user. The new flexible topology gives the user the power to tackle field analyses problems with challenging, complex geometries, but it also places a burden on the user to make wise choices. The new user–friendly input techniques implemented in ELF2 ameliorate the added difficulties, but ultimately there is an added requirement for user expertise that no clever user–friendly input techniques will replace.

Another limitation to the ELF2 achievements was in the areas of integration and documentation. The new grid generator was developed on an Iris RISC workstation, and the test cases were run on the Iris as well. The code was ported to the DNA VAX at Los Alamos as a means of delivering the final code, but it has not been exercised on the VAX. While that suggests the possibility of subtle compatibility problems, the ANALYZ results identified no code transportability issues which would cause problems in a VMS environment. Furthermore, although new i/o interfaces are well documented internally, we never integrated that documentation into a single users manual as we had hoped.

Finally, the ELF2 codes are limited to electric field analysis; no magnetic field information is calculated. There is an option in ELF to calculate the effect of a constant B–field on the conduction currents, but that is not the same as calculating B–fields. While the elementary magnetostatic field equations are similar (elliptical partial differential equations), they are more complicated in that they do not reduce to a scalar potential equation, but remain vector equations in any formulation.

In recognition of these limitations of the ELF2 codes, we offer the following recommendations.

7.2 RECOMMENDATIONS FOR FOLLOW–ON EFFORTS.

Foreseeing that the funded ELF2 tasks would not fulfill all requirements for electric (let alone magnetic) field modeling and analysis in the pulse power community engaged in SDI–related research and development, we included five specific pre–priced but unfunded options in the ELF Phase II contract summarized in Table 1.

This section lays out our recommendations for follow–on efforts both within and beyond the scope of those options. Rather than paralleling those options, we will discuss our recommendations here in the order of our perception of their priorities.

7.2.1. User Friendliness.

We use the term user–friendly to encompass moderate tasks which will significantly enhance the ability of a third party (any other SDI contractor or member of the Space Power Consortium) to effectively use the ELF2 code capabilities. One recommended action is to complete the integration and

check—out of the delivered codes in VAX/VMS (or any other chosen computational environment). Another recommended action is to integrate documentation on how to use the new capabilities and i/o techniques into the ELF Users Manual. Finally, we recommend implementation of a normal gradient boundary condition within the structure of the user—friendly interior boundary conditions (INTBC) input module. All three actions would cost about $30K, and do not directly fall under the scope of any one pre—priced option, although portions of these mundane, but necessary tasks could be accomplished under combinations of the ELF2 options, as we comment on below.

7.2.2. Generalized Geometries.

This falls under the scopes of Options 2 (2D) and 3 (3D). It is now clear that the best methodology for achieving maximum topological flexibility within the ELF finite—differences structure is to extend the grid blanking capability with the additional option of diagonal interior boundaries. Diagonal "cuts" will permit smoother matching to complex geometries, because a 45° bend in logical space represents a much milder discontinuity than a sharp 90° bend. To illustrate this, consider the conceptual boundary mapping of an Electro—Static Quadrapole (ESQ) geometry shown in Figure 29. Notice that all physical 90° corners map to logical 90° corners. This correlation between the grid logical connectivity and physical boundary conditions can be achieved for any topology with the diagonal cut option.

Generalizing to 3D involves more than sweeping 2D topologies in a third direction. In 3D there are various classes of diagonal cuts (110, 101, 011, 111 in Miller index notation). The 111 Miller index type of 3D diagonal has no 2D analogue, and will require special treatment.

Except for truly difficult 3D geometries (e.g. linked toroids), extension of 2D algorithms to 3D is relatively straightforward, but very tedious. Before developing the non—dielectric (pre—Phase I) 3D ELF code, we estimated the algebraic manipulations would require over two man—years. That was considered infeasible not only economically, but also because of the great difficulty of assuring error—free performance by the programmer. The solution was found in use of the artificial intelligence based symbolic manipulation program MACSYMA^{TM} (Ref. 10). Our approach to producing 3D versions of 2D codes will rely on MACSYMA to derive and code the very complex algorithms.

The pre—negotiated price of $82K on Option 2 (2D) will suffice to implement the concept, with some of the subtasks described in Section 8.2.1, above, included. The pre—negotiated price of $62K for Option 3 (3D) is just sufficient for implementation, but not for extensive documentation.

7.2.3. Input/Output Enhancements.

There are many computer solid modeling products which could define geometries for the ELF code. Much human engineering has gone into their design to make them very user—friendly. The huge commercial success of Computer Aided Design (CAD) programs, for example, is due as much to their ease of use as to their power. The question naturally arises, why not develop an interface for ELF to a commercial solid modeling package? The primary disadvantage is that such commercial packages have limited flexibility in the types of geometrical elements

50

that can be used: straight lines, circle arcs, and maybe ellipses in 2D; polyhedrons; pieces of spheres and maybe ellipsoids in 3D. The power of ELF to accurately analyze literally arbitrary shapes would be wasted without a mechanism for defining arbitrary shapes. If the shape can be defined with an analytical geometry formula, the formula can be coded in Fortran. However, as the new ELF2 interface input technique has shown, most geometries are made up of simple shapes, and much can be done with combinational techniques, so the user need not change a single line of code except on rare occasions.

We experimented with interfacing output to a commercial graphical program, and the vector—based technique can be adapted to produce CAD—readable output files. However, what we are more interested in here is interfacing input. Pre—priced Options 4 (2D) and 5 (3D) address interfacing ELF to the solid modeling code PATRAN.

PATRAN is a powerful geometry definition package for finite element codes. Because of its wide use, it is desirable to couple PATRAN to the ELF codes, so its powerful features can be exploited. However, since it is intended for use with finite element codes, there are many challenges in its application to a finite difference code like ELF, especially in 3D.

The PATRAN output is a collection of nodes (points in space) and elements (parametrically defined lines connecting nodes). The parametric definitions are well suited to the ELF geometry definition requirements in 2D. However, in 3D, ELF requires definition of surfaces enclosing the computational volume by means of logically cartesian grids. Not only must all the cells be quadrilateral (none triangular), but there must be exactly as many cells in each row (or column) as in every other. A general methodology for achieving this will be developed. Therefore these two options are costed assuming "cost plus fixed fee".

Under Options 4 and 5, Tetra and Ecodynamics will study the PATRAN data files, define the ELF requirements, and design and implement two interface programs (2D and 3D) to (a) read and interpret the PATRAN geometry files, and (b) generate the required boundary surfaces.

It is assumed and recommended that work on these options not be started until a decision has been made on Options 3 and 4. The ELF geometry definition requirements may be significantly different for the general geometry methodology implemented in Options 3 and 4.

The pre—negotiated costs for Options 4 and 5, $75K and $77K, respectively, are adequate to accomplish what's described above.

7.2.4.   Self—Consistent Magnetic Field Effects.

Option 1 (B—fields) would modify the ELF codes to include a self—consistent 3D treatment of external and self—generated B—fields.

There are many devices in SDI—related technologies where strong external B—fields play an important role, such as ion sources, Radio Frequency Quadrapole (RFQ) stages and Linear Accelerators (LINACs) for Neutral Particle Beam (NPB) weapons. Space plasmas are at such low pressures (<0.01 Torr) that charge transport is ballistic, rather than collision—dominated. Furthermore, it is believed that the geomagnetic field significantly affects spacecraft charging. The design of

space plasma shields may be affected by both phenomena. Many semiconductors and some insulators are non-isotropic. Externally imposed currents are critical in excimer lasers, free electron lasers, LINACs and other devices. Clearly, a tensor ELF code with self-consistent 3D magnetic field effects is needed for many SDI applications, and would be useful for many others, as well.

Under a contract with Sandia Corporation, Tetra and Ecodynamics implemented a scalar conductivity formulation of time-dependent space-charge effects, according to the formalism developed in Phase I. The application is for modeling fast streamers in laser-triggered gas gap switches. The "scalar" time-dependent space-charge ELF code will handle many other applications such as arcs and surface flashover. Corona discharges, outgassing, thermal instabilities, and mass movement can all be adequately modeled as long as scalar conductivity adequately models the currents. Corona discharges are probably critical limiters of space power distribution system performance. Outgassing, even though stabilized in hundreds of hours can significantly affect the space plasma environment of a "dormant" spacecraft if systems are heated just before activating the battle functions of the satellite. Thermal dependences of conductivity dominate in MHD generators, especially in the boundary layer of the MHD channel. In fact, the lower conductivity in the wall-cooled boundary layer causes most of the voltage drop to occur across that layer, limiting the MHD generator performance. All these phenomena can be analyzed with a scalar conductivity as long as components of the current vector transverse to the E-vector can be neglected.

If the J-vector could be guaranteed to be aligned in the same direction as the E-vector, we could always define a scalar conductivity $\sigma \equiv J/E$. A magnetic field causes a turning of the currents in the E×B direction. Thus, the conductivity becomes a tensor, just as in non-isotropic media. At low enough pressures, the electron's inertia can cause the currents to "lag" behind a changing E-field. Externally-imposed currents, like those from an electron gun, bear little relationship to the E-field at all. All these phenomena require reformulation of the ELF field solver.

An external B-field modifies the calculated current distribution linearly. That is, the modification does not affect the B-field used to calculate the effect. Self-generated B-fields, however, are nonlinear. The calculated current distribution determines the induced B-field, which adds to the linear external B-field. The total field affects the current. This nonlinear feedback loop adds to the computational complexity, but it is the same class of nonlinearity as already handled in the ELF codes. The combined nonlinear loop involves using estimated E and B fields to calculate the J distribution, then using the sensitivity of that to calculate corrections on the E and B fields.

For any physically realistic current model, the current distribution can be calculated from initial conditions and an estimated E-field. Assuming J is primarily local, we can numerically calculate a tensor differential conductivity, with which we can calculate correction terms for the E-field distribution. This method will converge on the field solution as long as nonlocal current sources do not dominate. This will be one of the limitations of the code produced in Option 1.

Another limitation is the assumption that the field time variations are slow enough (compared to the speed of light) that we can assume field information travels virtually instantaneously across the computational grid. This avoids the very tedious and costly procedure of numerically computing properly "retarded"

potentials. Within those limitations, the formulation will be based on the Poisson equation combined with the current conservation equation:

$$\vec{\nabla} \cdot (\epsilon \dot{\vec{E}}) = -\rho = \int \vec{\nabla} \cdot \vec{J} \, dt - \rho_{old} \tag{7.1}$$

and its magnetic analog:

$$\nabla^2 \vec{A} = \vec{J} \tag{7.2}$$

The driving function will be a user–modifiable current module, which will calculate $\vec{J}$ as a function of $\dot{\vec{E}}$, $\dot{\vec{B}}$, space, time and initial conditions. Boundary conditions will be incorporated for the magnetic vector potential $\vec{A}$ analogous to the Dirichlet and Neumman conditions on the scalar potential ϕ.

The resulting fully coupled Electro–Magnetic field code will include the effects of time–dependent space–charge. It will be tested with a sample kinetics model which will be extensible to collisionless plasmas.

Since the formulation of $\dot{\vec{B}}$–field effects is intrinsically three–dimensional, we will implement it in 3D directly, without a 2D phase first. However, a 1D prototype may be used to develop the algorithms and test the sample current module. These algorithms will then be generalized to 3D within the structures of the unsteady space–charge ELF code, making use of MACSYMA^{TM} for much of the code generation.

In order to insure an orderly progression, first only external B–fields will be considered, and then the self–generated B–field will be incorporated in a full nonlinear coupling. That is, the B–field induced by the current distribution will be included in calculating the effects of the total B–field on those currents.

Table 1. Phase II options.

1. **Self–Consistent B–field Codes.**

   Develop a self–consistent 3D treatment of magnetic fields within. The ELF boundary–fitted grid structure include external B–fields and nonlinearly coupled effects of B–field induced by calculated currents. Include time–dependent space–charge effects will be tested with a kinetics model.

2. **Generalized Geometries in 2D.**

   General geometry methodology which will allow a single 2D code to be used for virtually any 2D geometry.

3. **Generalized Geometries in 3D.**

   Implement the same methodology developed in 2D to a 3D general geometry ELF code.

4. **2D ELF Interface With PATRAN.**

   Develop an interface program to use geometry definition files produced by PATRAN to define the boundaries for the 2D ELF code.

5. **3D ELF Interface With PATRAN.**

   Develop an interface program to use geometry definition files produced by PATRAN to define the boundaries for the 3D ELF code.
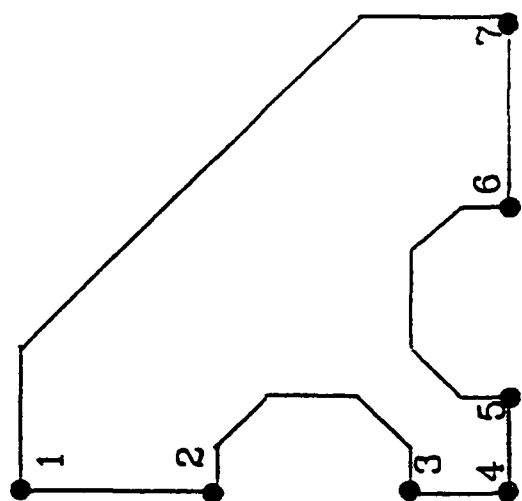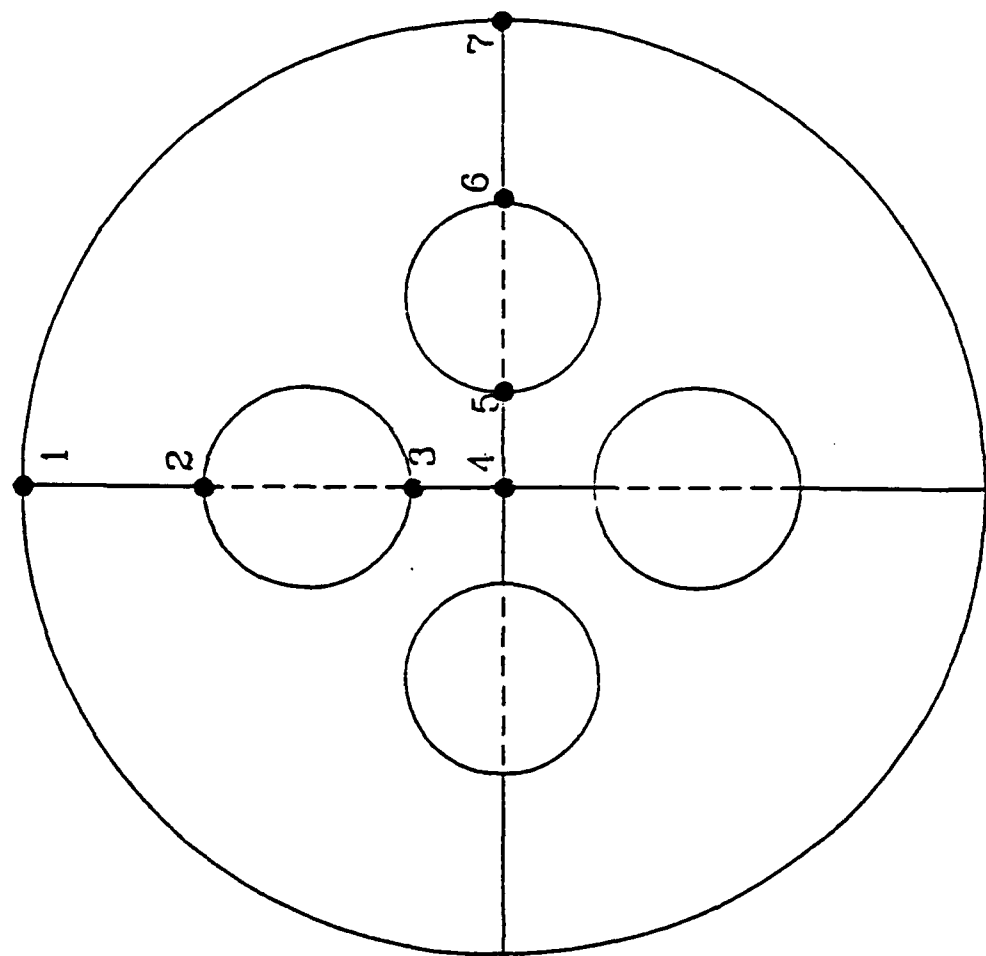
Figure 29. Mapping of ESQ cross-section to grid logical plane with diagonal cut-outs.

SECTION 8

LIST OF REFERENCES

1. von Dadelszen, M., W. M. Moeny and P. J. Roache, "Electric Field Calculations Using the ELF codes," **Proc. IEEE Pulsed Power Conference**, Crystal City, Washington, D.C., June 10–12, 1985.

2. Hsing, W. W., "Water Breakdown Review of Saturn", Sandia National Labs Memo to J. P. VanDevender, June 21, 1985.

3. Rose, M. F., "High Voltage Engineering in Space", IEEE Conference on Electrical Insulation and Dielectric Phenomena, Buffalo, NY, Oct. 1985.

4. Pavelle, R., and P. S. Wang, "MACSYMA from F to G", *Journal of Symbolic Computation* (1985), 1, 69–100.

5. Langmuir and Blodett, "Currents Limited by Space Charge Between Concentric Spheres," Phys. Rev. **24**, 2nd Series, 49, 1924.

6. Katz, I., *et al*, "Plasma Collection by High Voltage Spacecraft at Low Earth Orbit," J. Spacecraft 18 #1, Jan. – Feb. 1981.

7. Mandell, M. J., "Computer Modeling of Current Collection by the CHARGE–2 Mother Payload," unpub.

8. *ANALYZ FORTRAN Program Analyzer*, ASWIN #10, Computer Sciences Corporation.

9. Philliber, N. P., and G. D. Cable, *ANALYZ—A Tool*, Computer Sciences Corporation, January 1987.

10. Steinberg, S. and Roache, P. J., "Symbolic Manipulation of Computational Fluid Dynamics," Jour. Computational Physics, Vol. 57, No. 2, January 1985, pp. 251–284.

11. Katz, I., *et al.*, "Plasma Collection by High Voltage Spacecraft at Low Earth Orbit," J. Spacecraft, **18**, #1, Jan–Feb 1981.

12. Mandell, M.J. *et al.*, "Computer Modeling of Current Collection by the CHARGE–2 Mother Payload," unpub.

13. Katz, I., *et al.*, "Structure of the Bipolar Plasma Sheath Generated by SPEAR I," J. Geophys. Res., **94**, #A2, 1450, February 1989.

14. Langmuir, I., and K. Blodgett, "Currents Limited by Space Charge Between Concentric Spheres," Phys. Rev., **24**, 2nd Series, 49,1924.

15. Mandell, M. J., *et al.*, "Potentials on Large Spacecraft in LEO," IEEE Trans. on Nuc. Sci., **NS–29**, #6, 1584, December 1982.

16. Parrot, M.J., *et al*, "Theory of Cylindrical and Spherical Langmuir Probes in the Limit of Vanishing Debye Number," Phys. of Fluids, **25**, 2388, 1982.

17. Parker, L. W., and Murphy, B.L., "Potential Buildup on Electron Emitting Ionospheric Satellites," J. Geophys. Res., **72**,1631, 1967.

18. Katz I., *et al.*, "Plasma Collection by High Voltage Spacecraft at Low Earth Orbit," J. Spacecraft, **18**, #1, Jan–Feb 1981.

19. Mandell, M. J., *et al.*, "Computer Modeling of Current Collection by the CHARGE–2 Mother Payload," unpub.

20. Mandell, M. J., private communication, April, 1990.

21. Langmuir, I., and K. Blodgett, "Currents Limited by Space Charge Between Concentric Spheres," Phys. Rev., **24**, 2nd Series, 49, 1924.

22. Hindmarsh, A.C., "ODEPACK, A Systematized Collection of ODE Solvers," pp. 55–64, Scientific Computing, R. S. Stepleman *et al.*, ed., North Holland, Amsterdam, 1983.

23. Katz, I., *et al.*, "Space Plasma Induced Arcing on HV Solar Arrays," *IEEE Trans Elec Insul*, **25**, #2, pp.367–370, Apr 1990

24. Evans, R. D., *The Atomic Nucleus*, McGraw–Hill, 1955

25. Longmire, C. L., "On the Electromagnetic Pulse Produced by Nuclear Explosions," *IEEE Trans Antennas & Propag*, AP–26,#1, Jan 1978

26. Kieffer, L. J., and G. H. Dunn, *Rev Mod Phys*, **38**, 1, Jan 1966

27. Fano, U., *Annual Rev Nuc Sci*, **31**, 1, 1963

28. Katz, I. *et al.*, "Structure of the Bipolar Plasma Sheath Generated by SPEAR I," *J. Geophys. Res.*, **94**, #A2, 1450, Feb 1989

29. Hsing, W. W., "Water Breakdown Review of Saturn", Sandía National Labs memo to J. P. VanDevender, June 21, 1985

APPENDIX A

TEST CASE FOR SPACE CHARGE DRIVEN OPTION

A.1 SPACE–CHARGE FORMULATION.

The ELF electric field code can be used to calculate fields in the plasma sheath around a high voltage Low Earth Orbit (LEO) satellite by solving the nonlinear nonhomogeneous Poisson equation

$$\nabla^2 \phi = -\rho/\epsilon_0 \tag{A.1}$$

if the space–charge ρ is dominated by local dependencies. That, in fact, is the case for the steady–state solution (Ref. 1):

$$\rho/\epsilon_0 = \frac{-\phi}{\lambda_d{}^2} \left[\frac{(R_0/R)^2}{1 + \sqrt{4\pi} \, |e\phi/k\theta|^{1.5}} \right] \tag{A.2}$$

where $k\theta$ is the plasma temperature in eV (notice $e\phi/k\theta$ is unitless), and the Debye length is given by

$$\lambda_d{}^2 = \frac{\epsilon_0 \, k\theta}{n_0 \, e^2} \tag{A.3}$$

where n_0 is the background plasma number density.

The geometric convergence factor can be estimated for general geometries from the local potential ϕ and E–field by a fit to spherical diode results (Ref. 2) as:

$$(R_0/R)^2 = 2.29 \, |E \, \lambda_d \, e/k\theta|^{1.262} \, |k\theta/e\phi|^{.501} \tag{A.4}$$

For now, let us consider only a positive sheath, which expels positive ions and captures electrons. (The negative sheath can be treated similarly, as we shall show below.)

The calculation of ρ/ϵ_0 has been coded in subroutine SPCHRG, which initializes the plasma parameters $k\theta$ and n_0, and can be called by the main ELF program, much as a user—supplied conductivity module is now. Thus ELF can calculate field solutions equivalent to the NASCAP/LEO solutions (Ref. 3), through which a particle—pushing code can subsequently "push" electron orbits to calculate the current lost to open orbits (electrons that escape).

A.2 ELECTROSTATIC BENCHMARK.

The purpose of this Appendix is to derive an independent solution for a simple spherical geometry to serve as a benchmark for checking out the full 2D code. The space—charge—limited current between two concentric spheres was derived analytically by Langmuir and Blodgett (Ref. 4), and even generalized to infinite planes and cylinders. The analytical solution for concentric spheres is

$$i = \frac{4}{9} \sqrt{\frac{2e}{m}} \frac{\phi^{1.5}}{\alpha^2} \quad \text{in Electro—Static Units (ESU)} \qquad (A.5)$$

or

$$i = \frac{4}{9} \epsilon_0 4\pi \sqrt{\frac{2e}{m}} \frac{\phi^{1.5}}{\alpha^2} \quad \text{in International System of Units (ISU)} \quad (A.6)$$

We will use ISU in this Appendix. This analytical solution is not in closed form, however, since the unitless parameter α can at best be given by a series:

$$\alpha = \gamma - 0.3 \ \gamma^2 + .075 \ \gamma^3 - .0143182 \ \gamma^4 + .0021609 \ \gamma^5 \qquad (A.7)$$
$$-.00026791 \ \gamma^6 + ... \qquad (A.8)$$

where $\gamma = \ln(R/R_0)$; for our purposes, R_0 is the sheath radius, so γ is negative. Langmuir and Blodgett's Table II (attached) gives calculated values of α^2 for ratios R_0/R up to 500 (column labeled "$(-\alpha)^2$," for our purposes). For small ratios $R_0/R < 1.05$, the above series is more accurate than table interpolation.

The thermal current is given by the hemispherical directed flux across an ideal sharp boundary

$$j_{th} = n_0 \ e \ \sqrt{k\theta/2\pi m} \qquad (A.9)$$

However, since the Langmuir–Blodgett theory ignores transverse charge motion, we get the correct sheath size only by using the omnidirectional thermal flux across the sheath boundary (well–defined because $\lambda_d << R_o$):

$$\iota = 4\pi\ R_o^2\ n_o\ e\ \sqrt{k\theta/m} \qquad (A.10)$$

Combining both equations for ι (which must be independent of R to conserve current), we get

$$\frac{4}{9}\frac{\epsilon_0}{e}\frac{\phi^{1.5}}{\alpha^2} = R^2\ n_o\ \sqrt{k\theta/e} \qquad (A.11)$$

(Notice $k\theta/e$ is numerically the plasma temperature in eV.)

Expected ranges for low– to high–density LEO conditions (Ref. 5) are: $10^{10}/m^3$ < n_o < $10^{12}/m^3$, 0.3 eV > $k\theta$ > 0.1 eV, .04 m > λ_d > .002 m, and 10^{-4} A/m^2 < j_{th} < 10^{-2} A/m^2. The NASCAP/LEO calculations for a spherical collector of radius R_c = 10 cm charged to V_c = +45 kV showed a sheath of about 5 m radius (Ref. 3), using n_o = $5\times10^{10}/m^3$ and $k\theta$ = 0.1 eV. For R_o/R_c = 50, Table II gives $(-\alpha)^2$ = 395.3. Calculating R_o from

$$R_o^2 = \frac{4}{9}\frac{\epsilon_0}{e}\frac{1}{n_o\sqrt{k\theta/e}}\frac{\phi^{1.5}}{\alpha^2} \qquad (A.12)$$

and iterating on α, using interpolation on Table II values, we get R_o = 5.607 m.

Given the final interpolated value of $(-\alpha)^2$ for R_o/R_c = 56.07, we can calculate values of ϕ vs R from the tabulated values of $(-\alpha)^2$ versus R_o/R from

$$\left[\frac{\phi(R)}{V_c}\right]^{1.5} = \frac{\alpha^2(R)}{\alpha_0^2} \qquad (A.13)$$

The attached plots show the PHI versus R curves for various conditions. The first shows the nominal case (labeled "SPEAR I"), along with a family of curves for the same plasma parameters, but different boundary conditions. Notice any point along any curve represents an inner boundary condition (V_c, R_c) which is sufficient (with the implied outer boundary condition $\phi \rightarrow 0$ as $R \rightarrow \infty$) to define a

A–3

unique solution for given plasma parameters. The second plot shows the effect for the nominal boundary conditions (R_c = 0.1 m, V_c = 45 kV) of a range of plasma parameters (10^9–10^{12} e/m^3 and 0.1–0.4 eV).

We can calculate the E–field profile by finite differences, or by integration of the space charge. Poisson's equation in integral form for spherical symmetry becomes:

$$E_c R_c^2 - E_i R_i^2 = \int_{R_c}^{R_i} \frac{\rho}{\epsilon} R^2 \, dR \tag{A.14}$$

Since the field is nearly Coulombic except near the sheath edge, we shall assume between R–grid points that

$$\phi(R) \approx [\phi R]_{ave} / R \tag{A.15}$$

Substituting into

$$\rho(R) = n_o e \left[\frac{R_o}{R}\right]^2 \left[\frac{\theta}{2\pi\phi}\right]^{.5} \tag{A.16}$$

we get

$$E_c R_c^2 - E_i R_i^2 \approx \frac{n_o e}{\epsilon} R_o^2 \sqrt{\theta/2\pi} \, [(\phi R)^{-.5}]_{ave} \int_{R_c}^{R_i} R^{.5} \, dR$$

$$= \frac{n_o e}{\epsilon} R_o^2 \sqrt{\theta/2\pi} \, [1/\sqrt{\phi_c R_c} + 1/\sqrt{\phi_i R_i}] \, [R_c^{1.5} - R_i^{1.5}]/3 \tag{A.17}$$

Initializing the field at the collector to $E_c = V_c/R_c$, the above produces an estimate of the field at the first interior R–grid point. Applying the same relationship to any two neighboring R–grid points, we can calculate the E–field throughout the sheath by marching out to the sheath edge. The resulting E–field distributions, shown in the next plot for conditions corresponding to the first ϕ–plot, is compatible with estimates by finite differences.

Finally, if we use those E estimates in the Katz–Mandell algorithm, we get independent calculations of the space charge. The next plot compares the Katz–Mandell space–charge calculations to the direct Langmuir–Blodgett space–charge

$$\rho(R) = n_o e \left[\frac{R_o}{R}\right]^2 \left[\frac{\theta}{2\pi\phi}\right]^{.5} \tag{A.18}$$

Notice the disagreement near the sheath edge. The Langmuir–Blodgett approximation assumes a perfect discontinuity at the sheath edge (hard edge approximation) whereas the Katz–Mandell formula approximately accounts for the transition to a Debye screening region.

For the assumed n_0 and $k\theta$, the thermal current density is 4.238×10^{-6} A/m^2, giving a total collected current of

$$4\pi R_0{}^2 \ j_{th} \ = \ 167.4 \ \text{mA} \qquad (A.19)$$

compared with SPEAR I measurements of 51 mA (Ref. 3).

Parrot *et al* (Ref. 6) derive a correction factor of 1.45 for the above thermal current due to the effect of weak long–range fields. This does not increase the above current estimates by 1.45 directly, because the increased current increases the space charge, thus decreasing R_0. The effective R_0' can be obtained by using n_0' $= 1.45 \ n_0$, which produces R_0' $= 5.049$ m for 45 kV and the above conditions. The corrected current is then $4\pi \ (R_0')^2 \ 1.45 \ j_{th}$, which evaluates to 196.8 mA. The Parrot correction increases the Langmuir–Blodgett calculated current by somewhat less than a factor of 1.45. The discrepancy with SPEAR I experimental measurements in due primarily to the effect of the geomagnetic field.

A.3 GEOMAGNETIC FIELD EFFECT.

For the SPEAR I flight path, the geomagnetic field was B $= 0.4$ gauss ($= .4 \times 10^{-4}$ tesla). Parker and Murphy (Ref. 7) derive a limit on current collected by a conducting sphere in a constant, homogeneous B–field, assuming a Coulomb potential well. (Notice the Langmuir–Blodgett solutions are nearly Coulombic except near the sheath edge.) The Parker–Murphy collection radius is given by

$$\frac{R_{pm}{}^2}{R_c{}^2} \ = \ 1 \ + \ \sqrt{8V_c e/m} \ /(\omega R_c) \qquad (A.20)$$

where

$$\omega \ = \ B \ e/m \ = \ 7.035 \times 10^6/\text{s} \ \text{for} \ B \ = \ 0.4 \ \text{gauss} \qquad (A.21)$$

Thus, for the nominal case, R_{pm} = 1.894 m, and the Parker–Murphy current limit is:

$$2\pi \ R_{pm}^2 \ j_{th} \ = \ 9.552 \ \text{mA} \qquad (A.22)$$

The Parker–Murphy theory assumes that $\nabla \cdot E$ is virtually constant over a gyroradius. In fact, the gyroradius

$$R_g \ = \ V_e/\omega \ = \ \sqrt{2V_c e/m} \ / \ (Be/m) \qquad (A.23)$$

evaluates to 17.88 m for V_c = 45 kV. At some critical radius R^*, the gyroradius for the potential at that distance equals R^*. We can calculate that critical radius from

$$\phi^* R^* \ = \ V_c R_c \qquad (A.24)$$

$$R_g' \ = \ R_g \ \sqrt{\phi^*/V_c} \ = \ R_g \ \sqrt{R_c/R^*} \ = \ R^* \qquad (A.25)$$

$$\rightarrow \ (R^*)^{1.5} \ = \ R_g\sqrt{R_c} \qquad (A.26)$$

For the nominal conditions, R^* = 3.174. If we use that instead of R_{pm}, the modified Parker–Murphy current estimate is 26.83 mA.

If we assume the effective current–collecting sheath surface is distorted into an oblate spheroid (as if the Langmuir–Blodgett sheath were "pinched" in the direction normal to the B–field), we can estimate the collected current by using a geometric average radius. Using the modified Parker–Murphy radius

$$4\pi \ j_{th} \ R_o \ R^* \ = \ 94.79 \ \text{mA} \qquad (A.27)$$

Using the unmodified radius

$$4\pi \ j_{th} \ R_o \ R_{pm} \ = \ 56.55 \ \text{mA} \qquad (A.28)$$

That is close to the SPEAR I measurement of 51 mA, but that does not prove the above method is generally accurate. The attached plot compares the complete range of SPEAR I current vs voltage measurements to all five theoretical

calculations: Langmuir–Blodgett, Parker–Murphy, modified Parker–Murphy, and the two "oblate spheroid" formulas.

What this exercise really proves is that a complete calculation of the collected current is rather complicated, and no simple model can be expected to produce accurate results, even for a spherical collector. Is the Langmuir–Blodgett electrostatic field solution invalidated by the magnetic field effect? Consider the following argument.

To first order, since the magnetic force is energy–conservative, the velocity–differential effect on the space–charge distribution remains unaffected, except for the current obliquity (angle between electron paths and radial direction). Clearly a 17–m gyroradius near the collector has a negligible effect. The space–charge will be most affected by the B–field near the edge of the sheath, where the electrons entering the sheath are still nearly thermal. For 0.1 eV electrons in a 0.4 gauss B–field, the gyroradius is

$$R_g(min) = \sqrt{2kT_e/m} \approx 2.7 \text{ cm} \qquad (A.29)$$

which is comparable to the Debye length. A difference of a few cm in the sheath radius in the direction normal vs parallel to the B–field hardly invalidates the assumption of spherical symmetry. Even though the B–field drastically reduces the collected current, it does not significantly alter the Langmuir–Blodgett electrostatic field solution. The Langmuir–Blodgett ϕ distribution provides us with the benchmark we need to validate the coding of the space charge driven ELF2 option.

The Langmuir–Blodgett sheath calculations described have been coded in program SHEATH on the PC–AT. SHEATH can be used to generate benchmark ϕ vs R curves for validating the 2D ELF implementation with a simple concentric–spheres geometry. The appropriate outer boundary condition for the 2D case is $\phi = 0$ at a far–field sphere of radius $R_b > R_o$. The actual sheath boundary will fall out naturally from the 2D calculations, although it may not be as well–defined as in the benchmark model. That is because the space–charge does not vanish exactly until $\phi = 0$ exactly. In fact, this is physically correct; the sheath boundary is

"fuzzy" on a scale size of λ_d. In the 2D ELF code, we should define the sheath boundary as the 2D contour where the calculated potential is $\phi = k\theta/e$, which may be less than the calculational tolerance. Beyond this nominal sheath boundary, the potential drops off quickly with a scale length of λ_d. (The small fields beyond R_o lead to the Parrot correction).

4.4 NOTES ON THE NEGATIVE SHEATH.

The above derivation is for a positive (potential) sheath, which traps electrons and excludes (positive) ions. If we reverse polarity, a negative sheath forms which traps ions and repels electrons. The high energy ions impinging on the current collector will free electrons, creating a steady–state out–going flux of electrons. For conditions typical of the SPEAR I experiment, each ion will create about 10 electrons (Ref. 3). Therefore, the electrons will dominate the total current. However, due to their much larger mass, the ions will dominate the space–charge. This keeps the space–charge calculation the same (except for sign), since the particle mass does not enter in the formula for $\rho = fn(\phi)$ and cancels out in the benchmark calculation of ϕ vs R. Therefore, the positive sheath model and benchmark calculations apply to a negative sheath as well, with only a sign change on the potentials.

Notice the Parker–Murphy radius is very different for ions, due to their much larger mass. If we use an average of 15 amu (between N and O atoms), $m_i \approx 2.5\times10^{-26}$ kg. For B = 0.4 gauss, the ion gyrofrequency is only about 250/s, giving a gyroradius of about 3 km, and $R^* \approx 100$ m. Clearly, the geomagnetic field will have a negligible effect on the ion current collected by a negative sheath.

Table 2. a^2 as function of radius.

r_0 = radius of emitter; r = radius at any point P:
a^2 applies to case where P is outside emitter, $r > r_0$:
$(-a)^2$ applies to case where P is inside emitter, $r_0 > r$.

| $\frac{r}{r_0}$ or $\frac{r_0}{r}$	a^2	$(-a)^2$	$\frac{r}{r_0}$ or $\frac{r_0}{r}$	a^2	$(-a)^2$
1.0	0.0000	0.0000	6.5	1.385	13.35
1.05	.0023	.0024	7.0	1.453	15.35
1.1	.0086	.0096	7.5	1.516	17.44
1.15	.0180	.0213	8.0	1.575	19.62
1.2	.0299	.0372	8.5	1.630	21.89
1.25	.0437	.0571	9.0	1.682	24.25
1.3	.0591	.0809	9.5	1.731	26.68
1.35	.0756	.1084	10	1.777	29.19
1.4	.0931	.1396	12	1.938	39.98
1.45	.1114	.1740	14	2.073	51.86
1.5	.1302	.2118	16	2.189	64.74
1.6	.1688	.2968	18	2.289	78.56
1.7	.208	.394	20	2.378	93.24
1.8	.248	.502	30	2.713	178.2
1.9	.287	.621	40	2.944	279.6
2.0	.326	.750	50	3.120	395.3
2.1	.364	.888	60	3.261	523.6
2.2	.402	1.036	70	3.380	663.3
2.3	.438	1.193	80	3.482	813.7
2.4	.474	1.358	90	3.572	974.1
2.5	.509	1.531	100	3.652	1144
2.6	.543	1.712	120	3.788	1509
2.7	.576	1.901	140	3.903	1907
2.8	.608	2.098	160	4.002	2333
2.9	.639	2.302	180	4.089	2790
3.0	.669	2.512	200	4.166	3270
3.2	.727	2.954	250	4.329	4582
3.4	.783	3.421	300	4.462	6031
3.6	.836	3.913	350	4.573	7610
3.8	.886	4.429	400	4.669	9303
4.0	.934	4.968	500	4.829	13015
4.2	.979	5.528	600	4.960	
4.4	1.022	6.109	800	5.165	
4.6	1.063	6.712	1000	5.324	
4.8	1.103	7.334	1500	5.610	
5.0	1.141	7.976	2000	5.812	
5.2	1.178	8.636	5000	6.453	
5.4	1.213	9.315	10000	6.933	
5.6	1.247	10.01	30000	7.693	
5.8	1.280	10.73	100000	8.523	
6.0	1.311	11.46			

(Reproduced from Lansmuir and Blodgett, 1924)
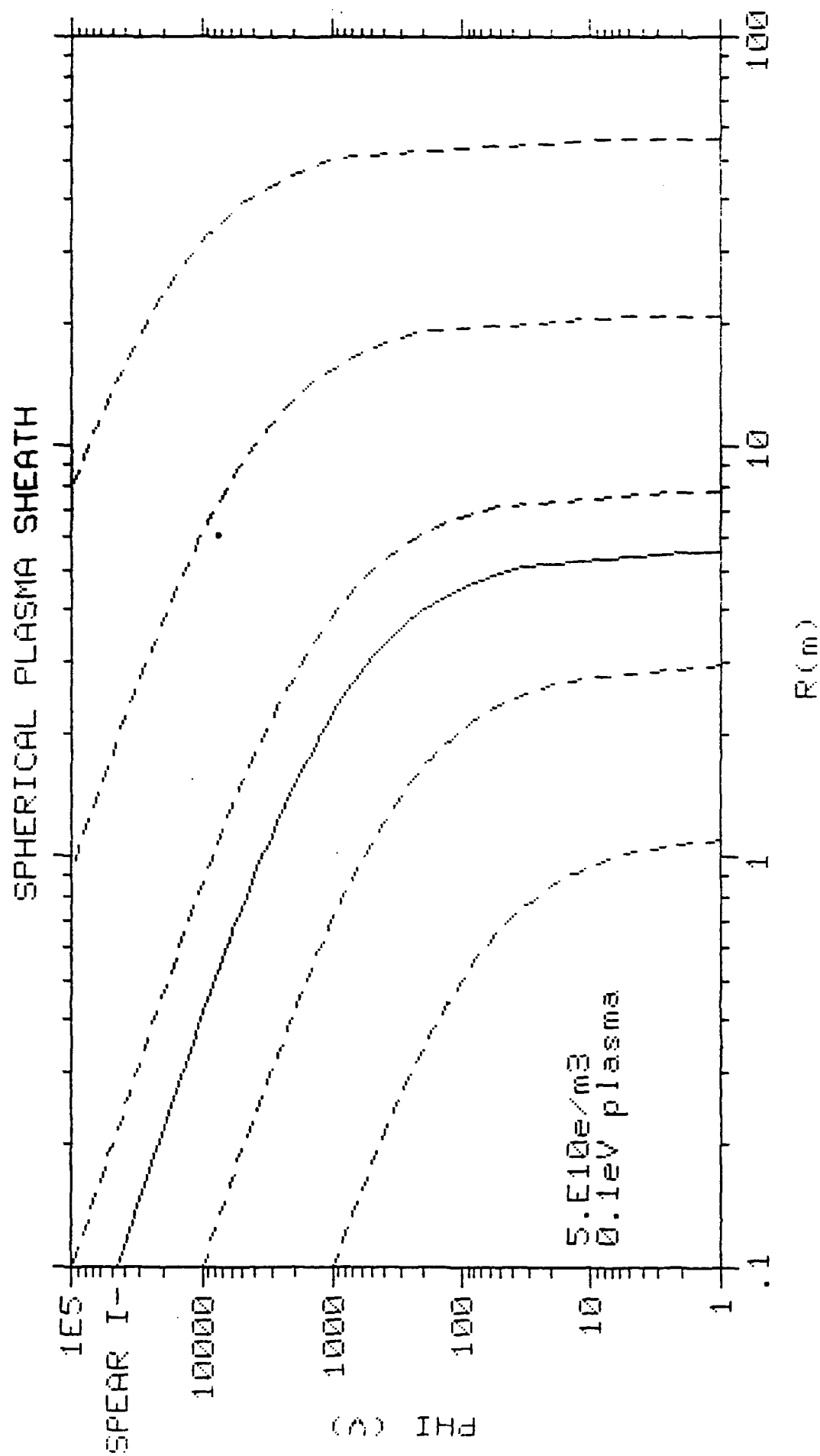
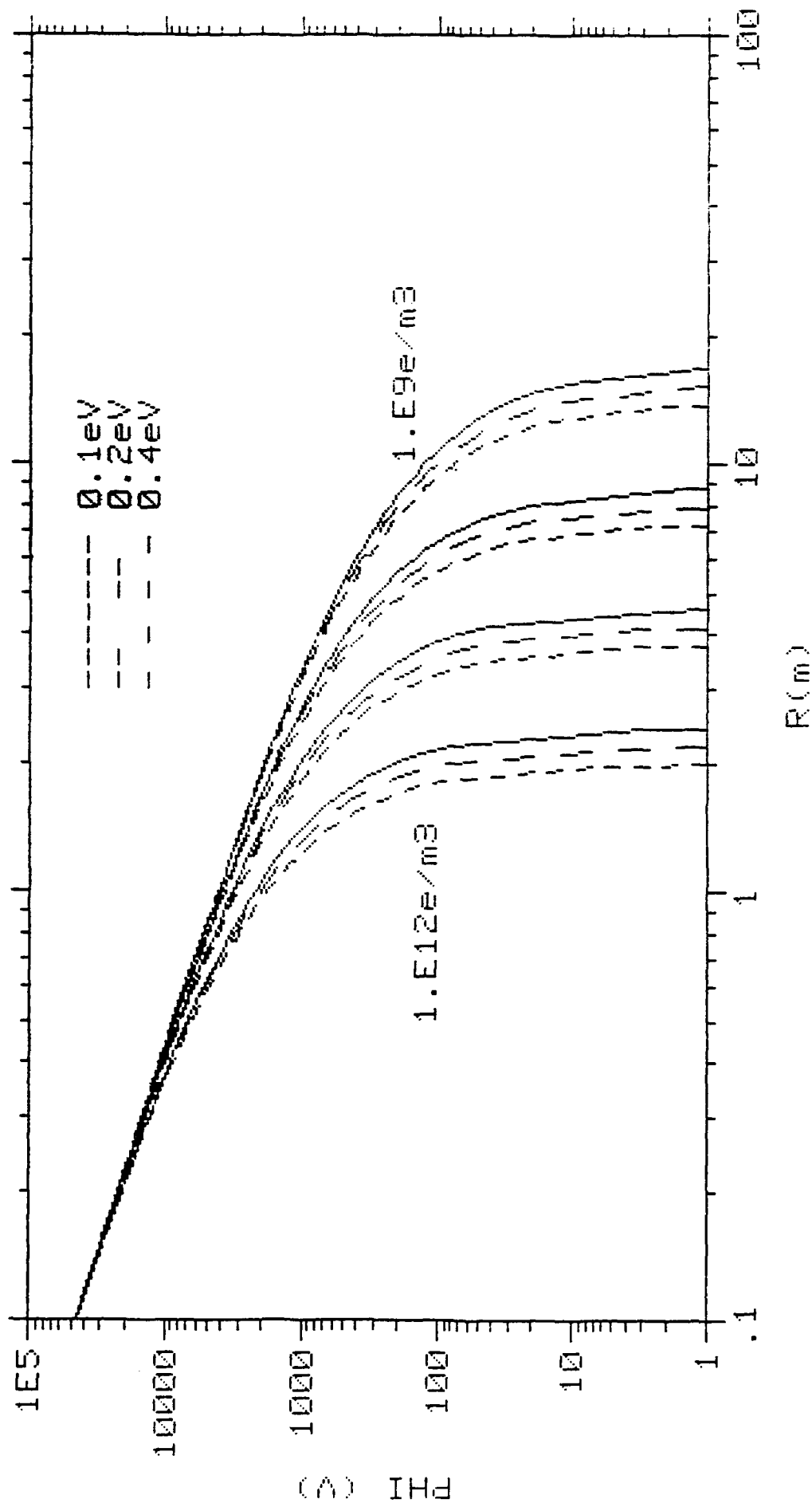Figure 30. Potential profile for various probe potentials.
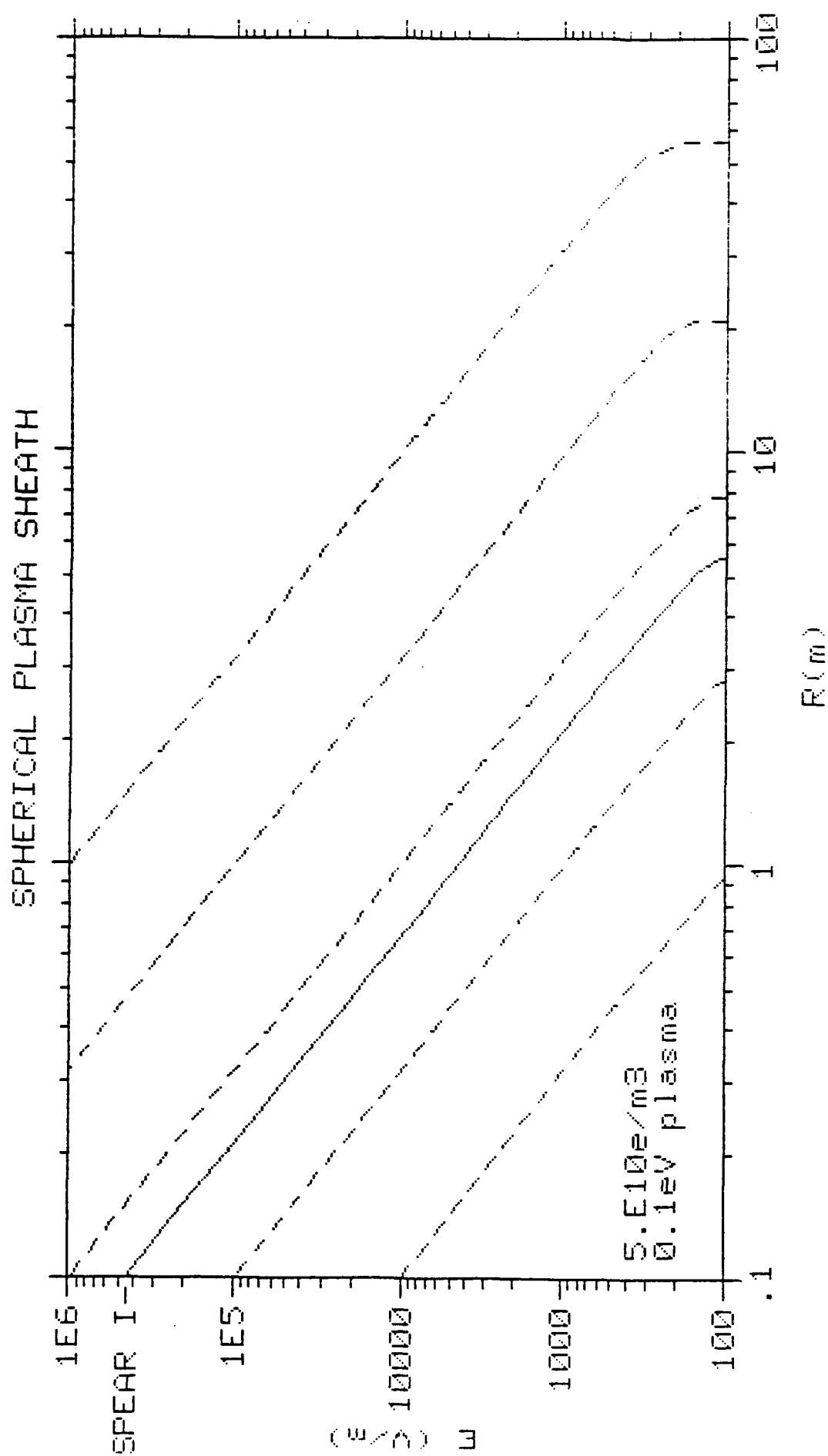
Figure 31. Potential profiles for various plasma parameters.

Figure 32. E-field profiles for various probe potentials.

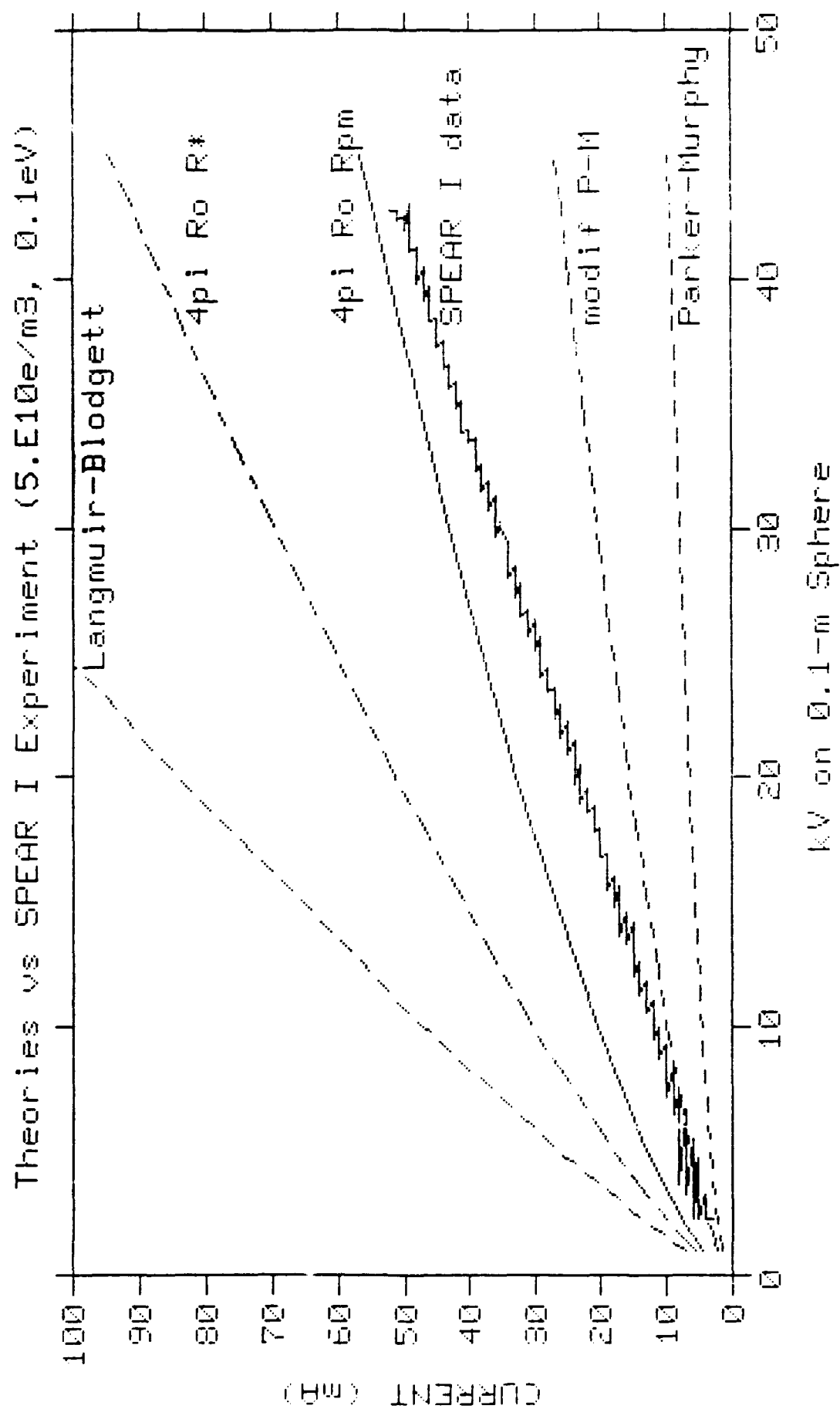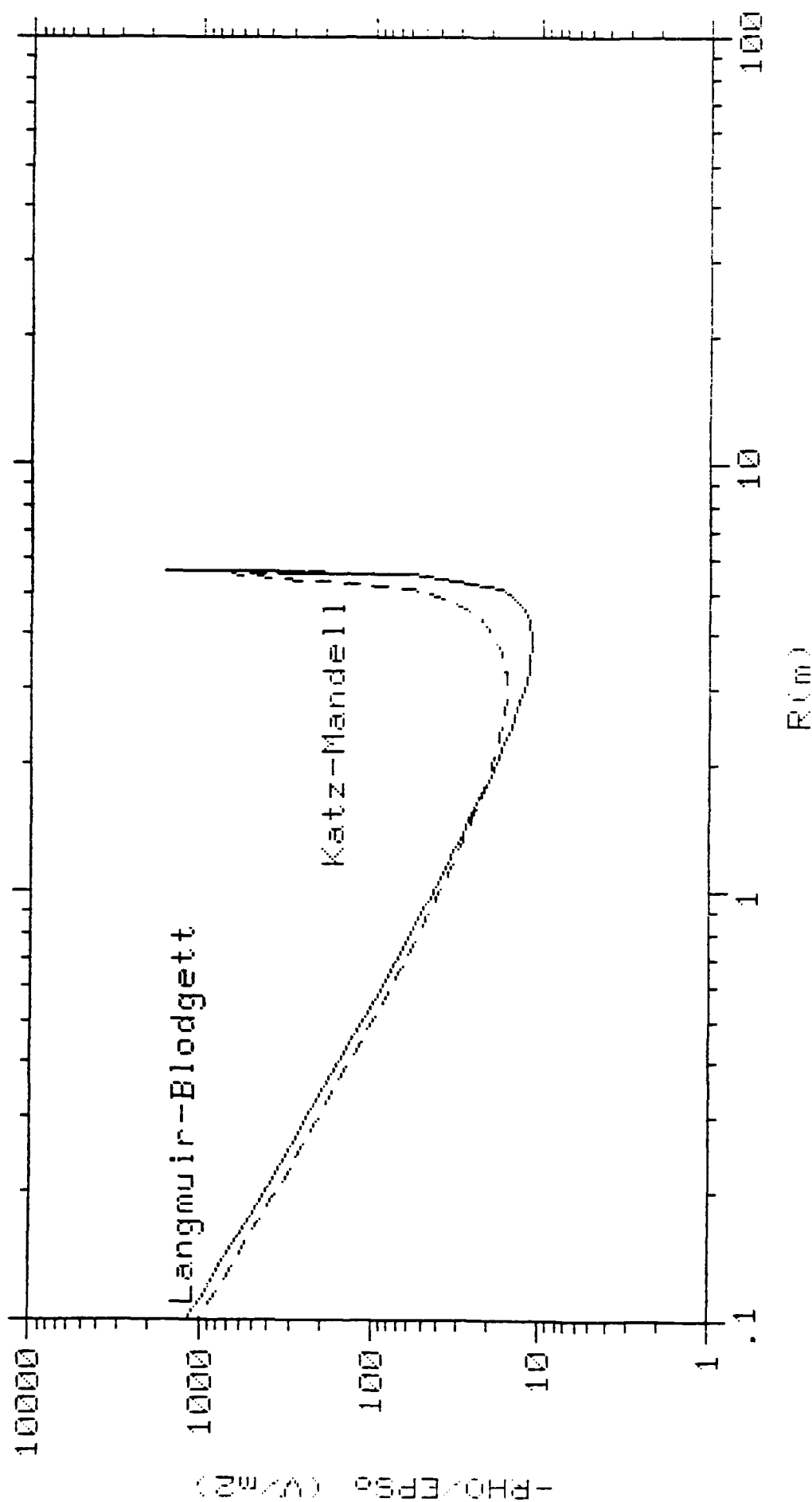Figure 33. Comparison of various theoretical I-V calculations.

Figure 34. Space-charge profiles by two methods.

A-14

APPENDIX B

ALTERNATIVE TO MANDELL FIT FOR CONVERGENCE FACTOR

The fields in a Low Earth Orbit (LEO) space plasma sheath are driven by the space–charge ρ, which is dominated by local dependencies in steady–state (Ref. 1):

$$\rho/\epsilon_0 = \frac{-\phi}{\lambda_d^2} \left[\frac{(R_0/R)^2}{1 + \sqrt{4\pi} \, |e\phi/k\theta|^{1.5}} \right] \qquad (B.1)$$

where $k\theta$ is the plasma temperature in eV (notice $e\phi/k\theta$ is unitless), and the Debye length is given by

$$\lambda_d^2 = \frac{\epsilon_0 \, k\theta}{n_0 \, e^2} \qquad (B.2)$$

where n_0 is the background plasma number density.

It is computationally convenient to estimate the geometric convergence factor $(R_0/R)^2$ for general geometries from the local potential ϕ and E–field. Mandell's fit (Ref. 2):

$$(R_0/R)^2 = 2.29 \, |E \, \lambda_d \, e/k\theta|^{1.262} \, |k\theta/e\phi|^{.501} \qquad (B.3)$$

purports to do just that. However, in trying to understand the detailed field distributions near the sheath edge, we found some apparent inconsistencies. Mandell (Ref. 3) explained that the fit actually comes from idealized spherical solutions of the Langmuir–Blodgett equations (Ref. 4). This Appendix documents an alternative to Mandell's fit based on a return to the basic 1D solutions.

The problem seems to be that Mandell's fit is sub–optimized over too wide a range of parameters. It specifically has trouble behaving reasonably in the region near R_0. The calculated R_0 values using Mandell's fit are not badly off, but there is a risk that the inconsistencies could cause subtle problems with more accurate field solvers, like ELF2.

If you assume spherical symmetry, the problem becomes 1-dimensional. It is then possible to numerically integrate the simple ODE system:

$$\frac{d\phi}{dR} = -E \quad \text{and} \quad \frac{d(ER^2)}{dR} = \rho R^2 \quad (B.4)$$

This becomes an initial-value problem if we have both E and ϕ defined at some value of R. We define the sheath boundary R_0 as the place where $\phi_0 = k\theta/e$ (plasma temperature in volts). If we guess $E_0 \approx \phi_0/\lambda_d$, and integrate out from R_0 using the Livermore Solver of ODE's (Ref. 5), we find that ϕ goes negative, indicating the initial E_0 guess is too high. If E goes negative, that indicates the E_0 guess is too low. A "high/low game" iterative procedure with a Newton–Raphson predictor quickly finds the correct E_0 value within machine precision. We then use that initial E_0 value to integrate from R_0 in to R_c to generate the "exact" solution.

That lead to the the following alternate methodology for estimating the convergence factor from local E, ϕ fields:

1. Define a "model" 1-D problem by choosing ϕ_c, R_c (and plasma parameters θ, n_0). From the Langmuir–Blodgett solution (Ref. 4), we can estimate R_0 by iterating on

$$R_0{}^2 = \frac{4}{9} \frac{\epsilon_0}{e} \frac{1}{n_0\sqrt{k\theta/e}} \frac{\phi^{1.5}}{\alpha^2} \quad (B.5)$$

where α is a function of R_0/R, interpolated from Langmuir & Blodgett's Table II.

2. The exact solution for that R_0 value provides a data base: E, ϕ, R arrays. The E_0 value calculated in the process defines the second boundary condition for the multi-dimensional Stefan problem of finding the sheath boundary; R_0 provides guidance for a first guess at locating the Stefan boundary. The key to the alternate method is using the 1-D test problem solution for piece-wise fits of the form

$$\left[\frac{R_0}{R}\right]^2 = \left[\frac{E}{E_0}\right]^{X_e} \left[\frac{\phi}{\phi_0}\right]^{X_v} \quad (B.6)$$

Notice Mandell's fit takes this form if $E_o = k\theta/e\lambda_d /2.29^{1/1.262}$. Only two data points are needed from the data base to define the fit coefficients x_e and x_v. The correct "neighborhood" is defined by the requirement that the actual E, ϕ values both be internal to the discrete array values used. The procedure is analogous to a table look-up and interpolation. The whole process is coded in module CNVRGC, which initializes the internal data base (E, ϕ, R arrays) and subsequently estimates the convergence factor $(R_o/R)^2$.

To test the methodology, we integrated the 1-D field equations for different R_o values exactly, and compare to the results using the CNVRGC module and using the Mandell fit. The attached plots show the results for a nominal $5 \times 10^{10}/m^3$, 0.1-eV plasma. The base case used to initialize the CNVRGC module is $V_c = 45$ kV, $R_c = 0.1$ m, for which $R_o \approx 8$ m. Notice the CNVRGC E, ϕ solutions are closer to the exact than the Mandell solutions, even though neither is bad. The Mandell solutions, if adjusted to exactly match the same V_c at R_c, would result in only a small error in R_o, and hence a small error in the estimated collected current, which goes as R_o^2. The difference between the CNVRGC and Mandell solutions is most marked in the "RHO" plots. The reason for the discrepancy is obvious in the "Calculated R_o" plots. Notice the CNVRGC model errors are much smaller than for the Mandell fit, and the latter exhibit a worrisome structure near R_o.

One word of caution: Attempts to use the CNVRGC model with different plasma parameters than those used to initialize the internal data resulted in larger errors. The CNVRGC model in effect produces a customized fit function for given plasma parameters which remains accurate for a wide range of geometries, but should be re-initialized if plasma parameters change. However, for given plasma parameters, the CNVRGC "customized" fit is clearly superior to the "universal" Mandell fit.

To prove that point, we repeated similar analyses for two plasma extremes: 10^9 and 10^{12} e/m^3, both at 0.2 eV (temperature makes litle difference compared to number density within resaonable LEO ranges). The next two sets of three plots show the results. Notice in both sets the CNVRGC function provides very good agreement even for problems far from the "calibration" model problem, and always better than the Mandell fit.
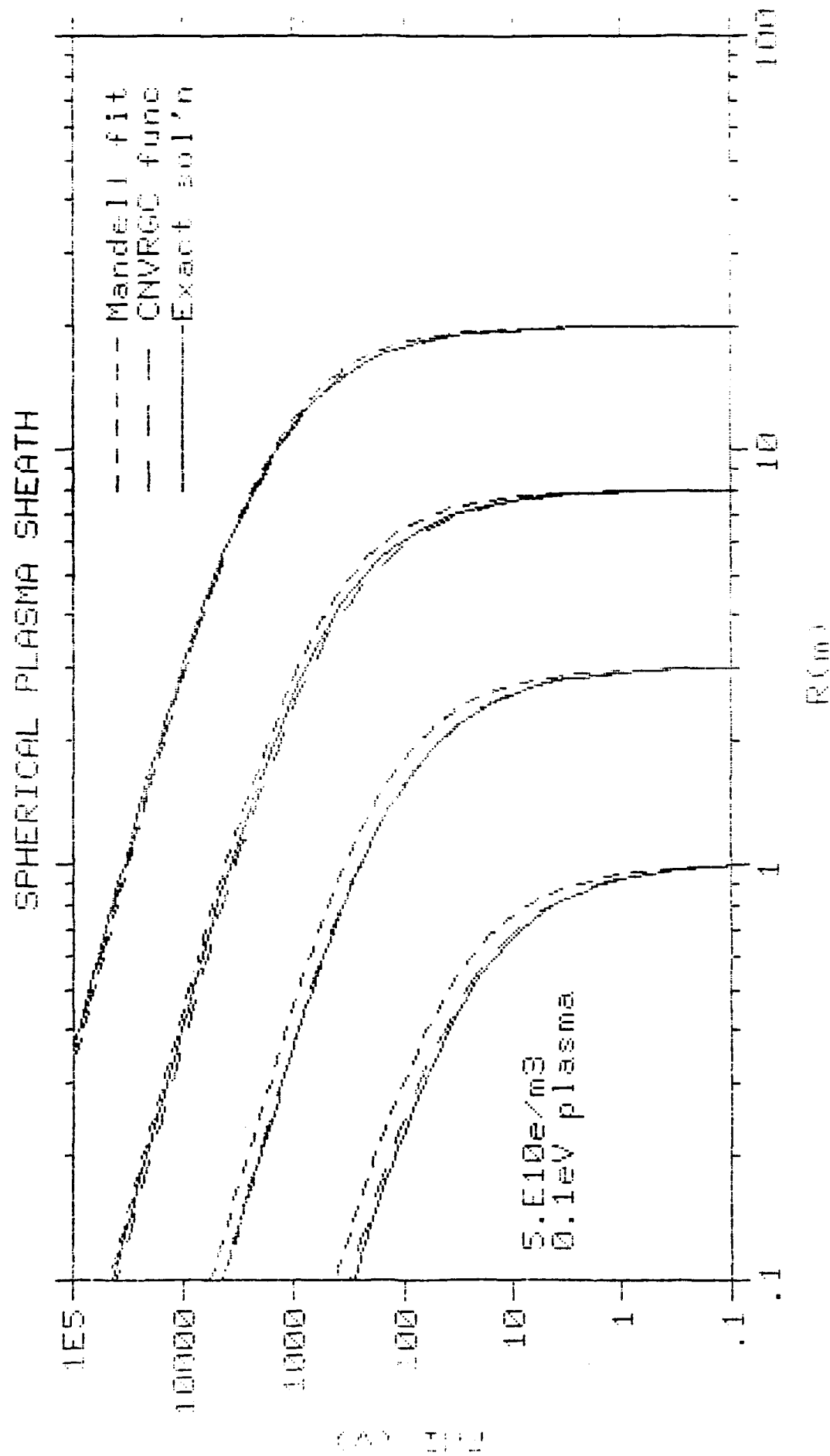
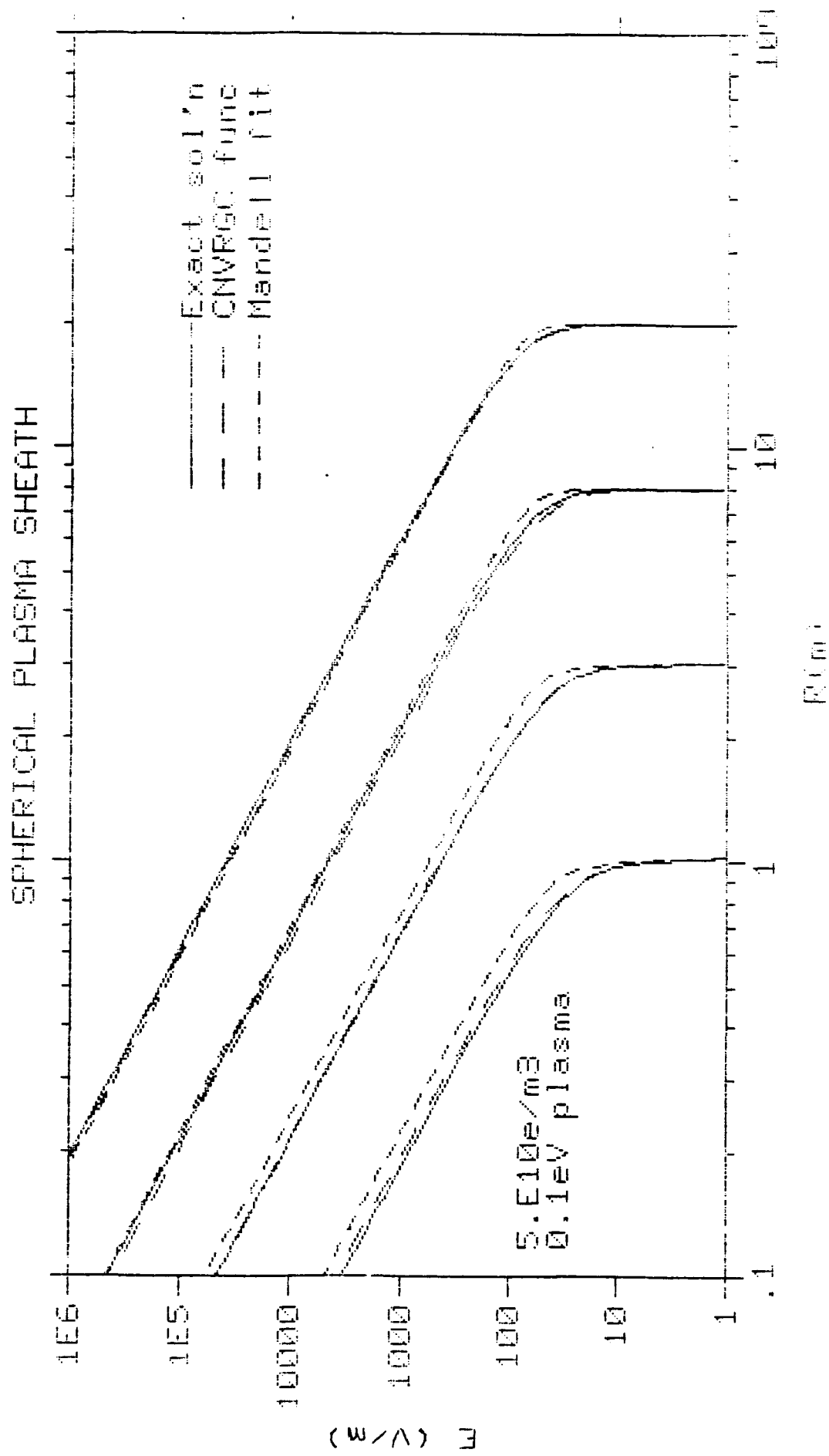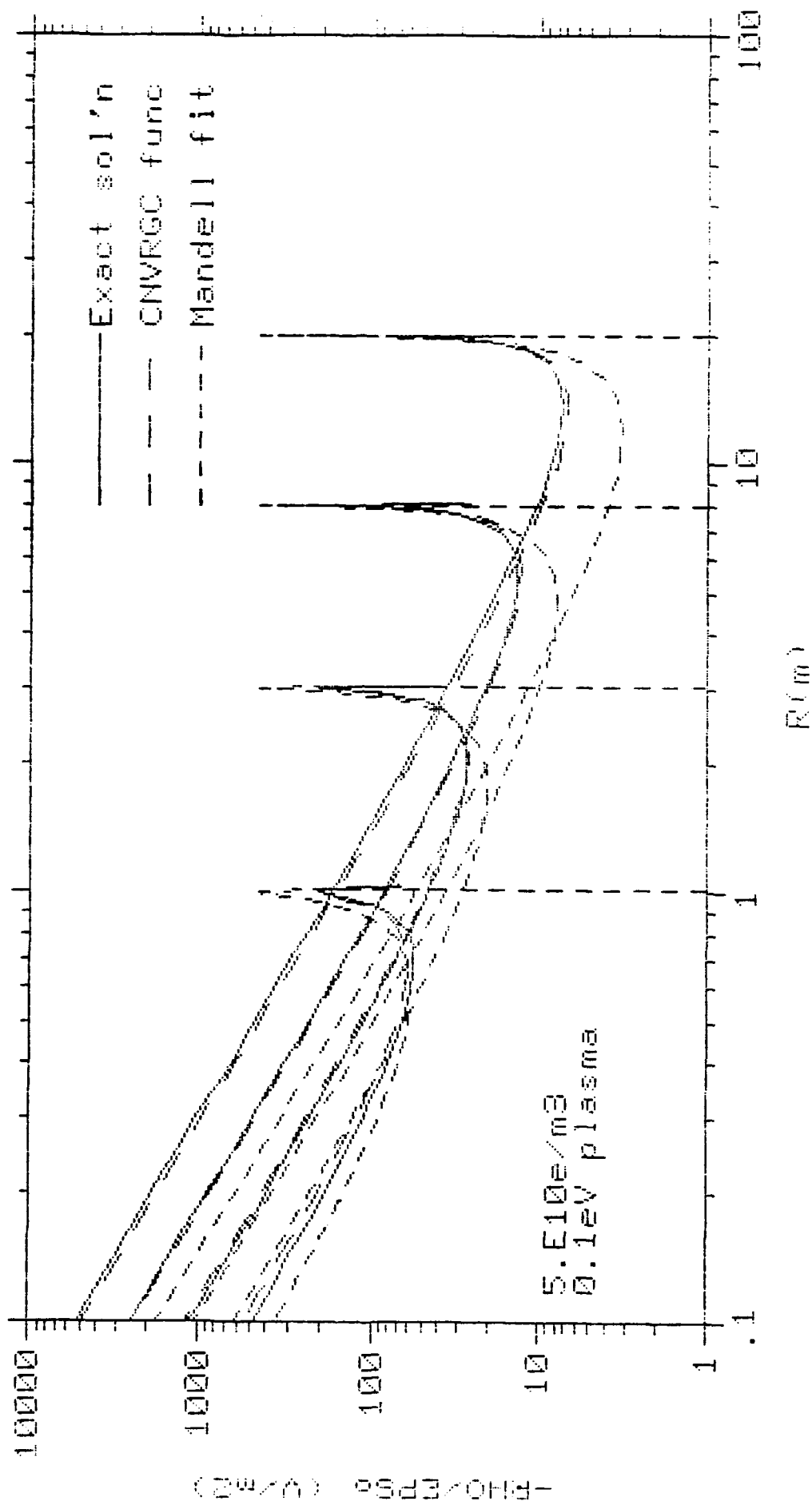Figure 35. Potential profiles by various methods.

Figure 36. E-field profiles by various methods.

Figure 37. Space-charge profiles by various methods for sheath radii.

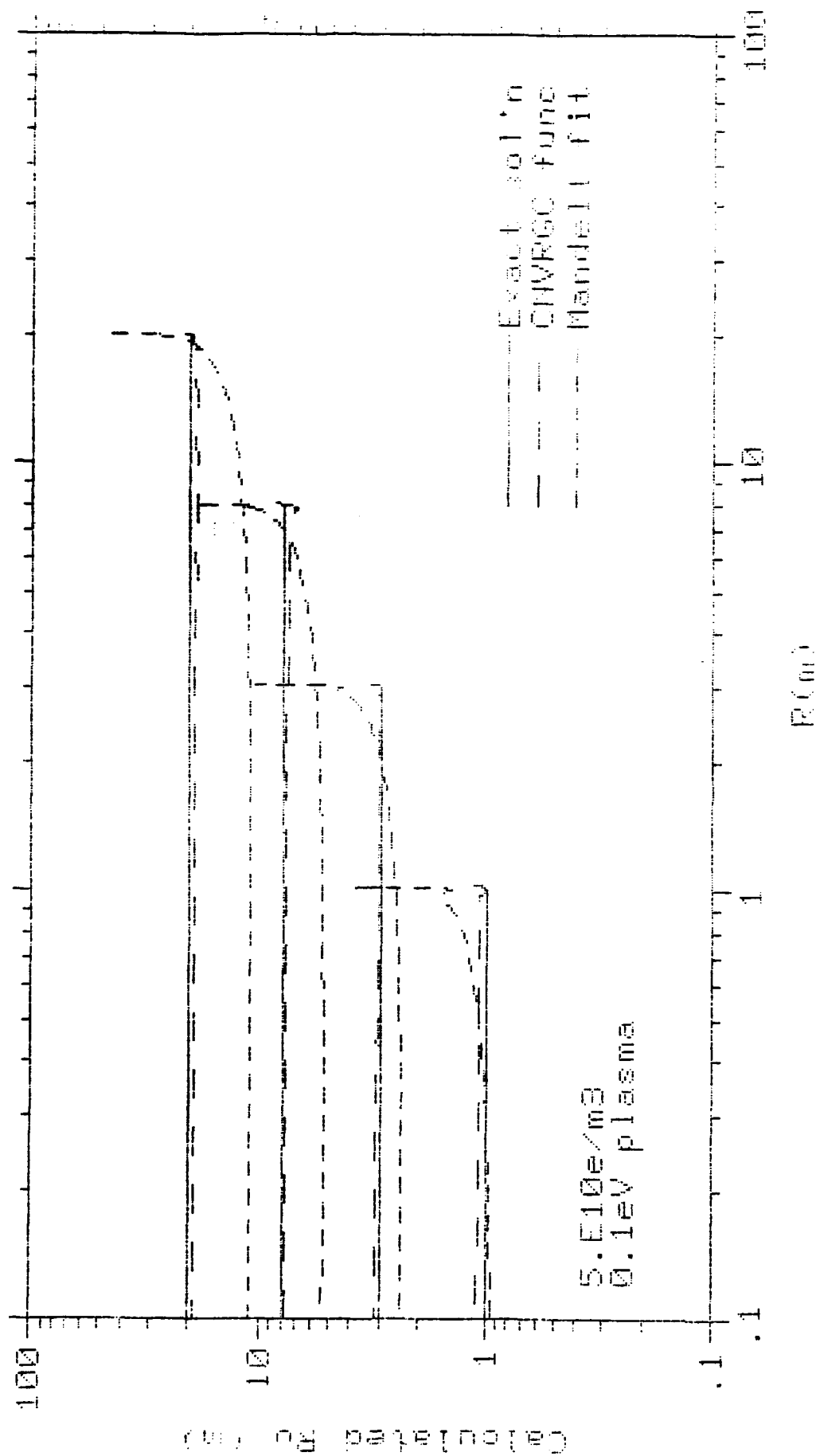Figure 38. Effective sheath radius by various methods.
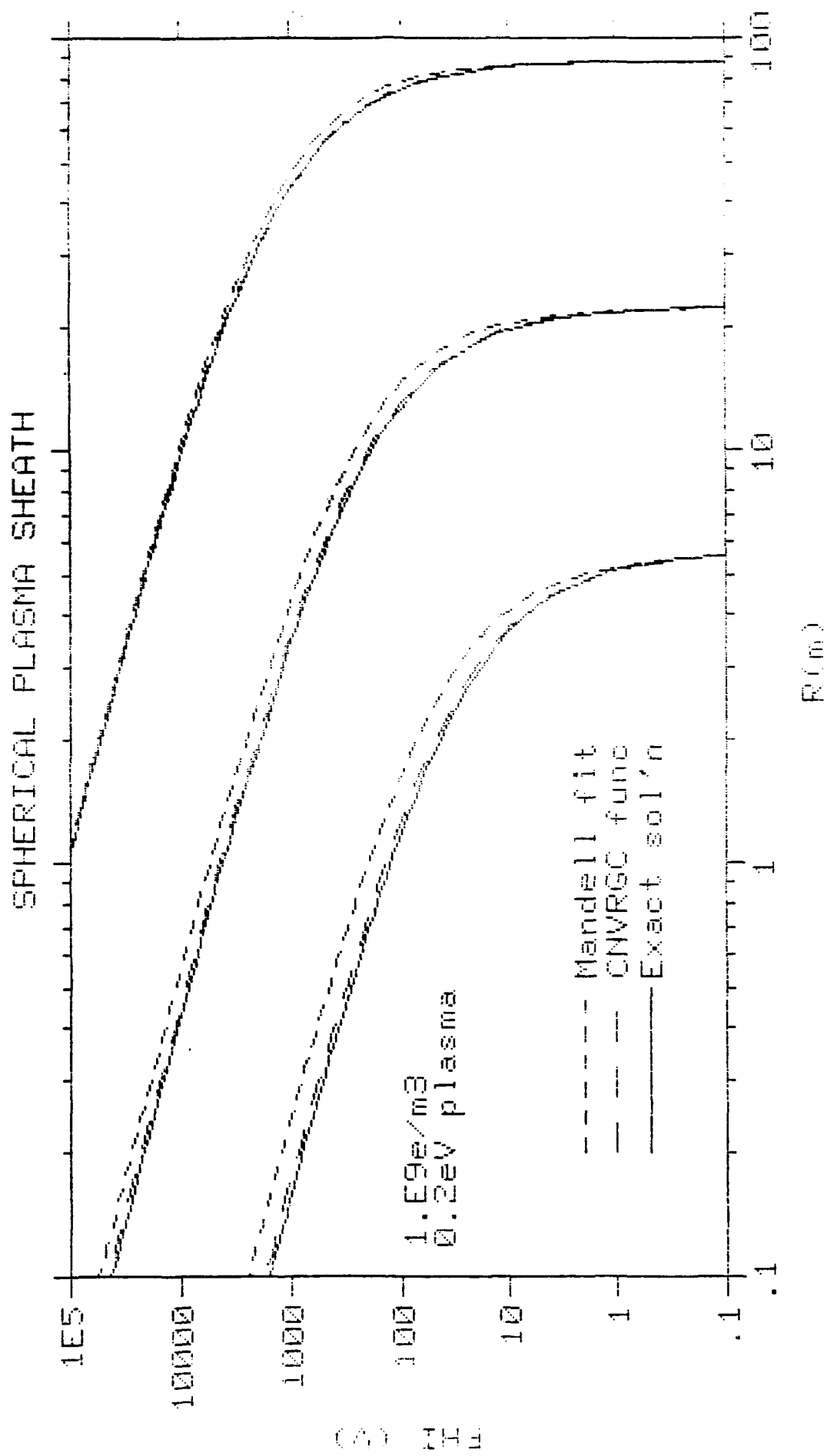
Figure 39. Potential profiles for various sheath radii.
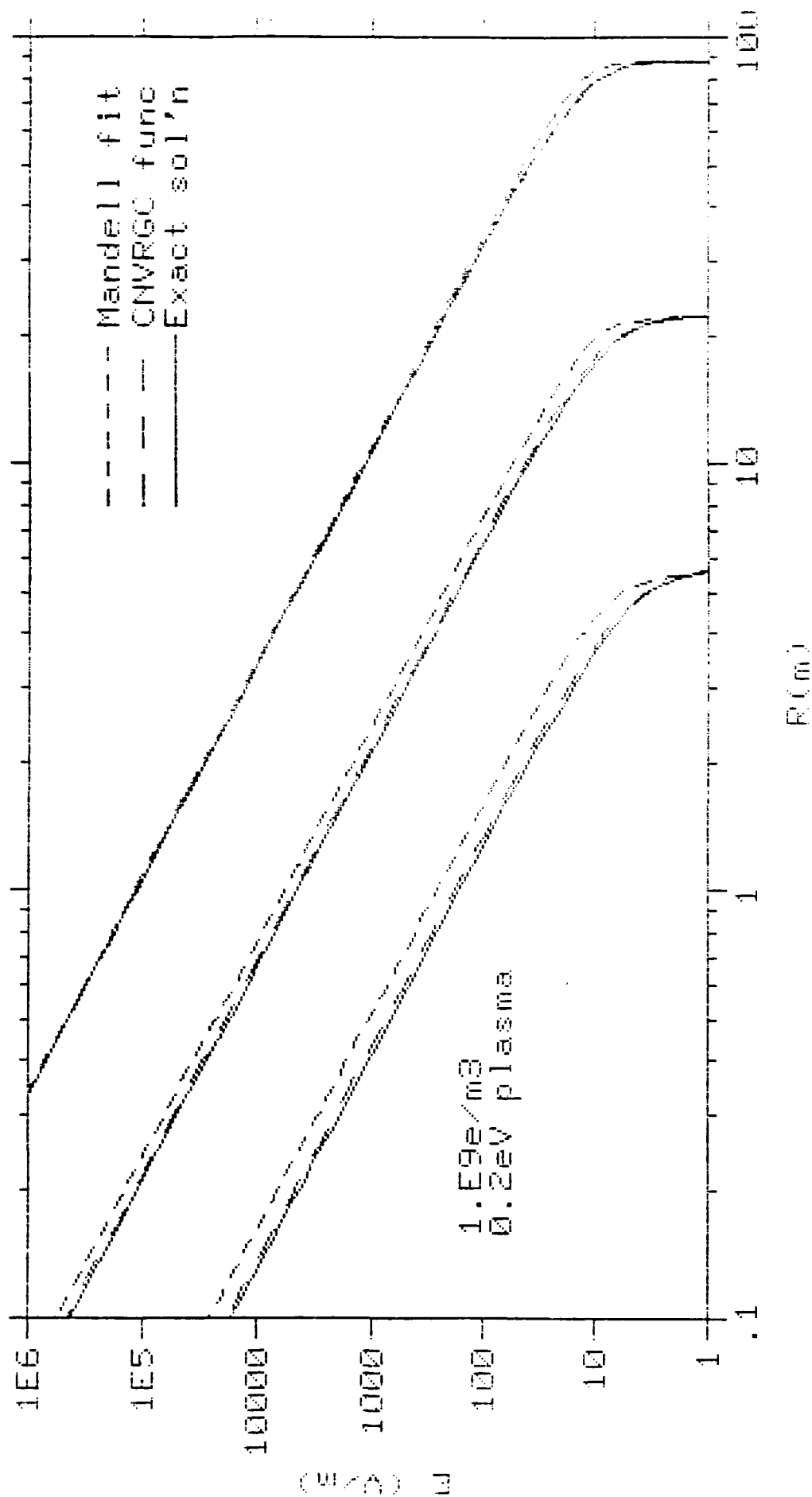
Figure 40. E-field profiles for various sheath radii.
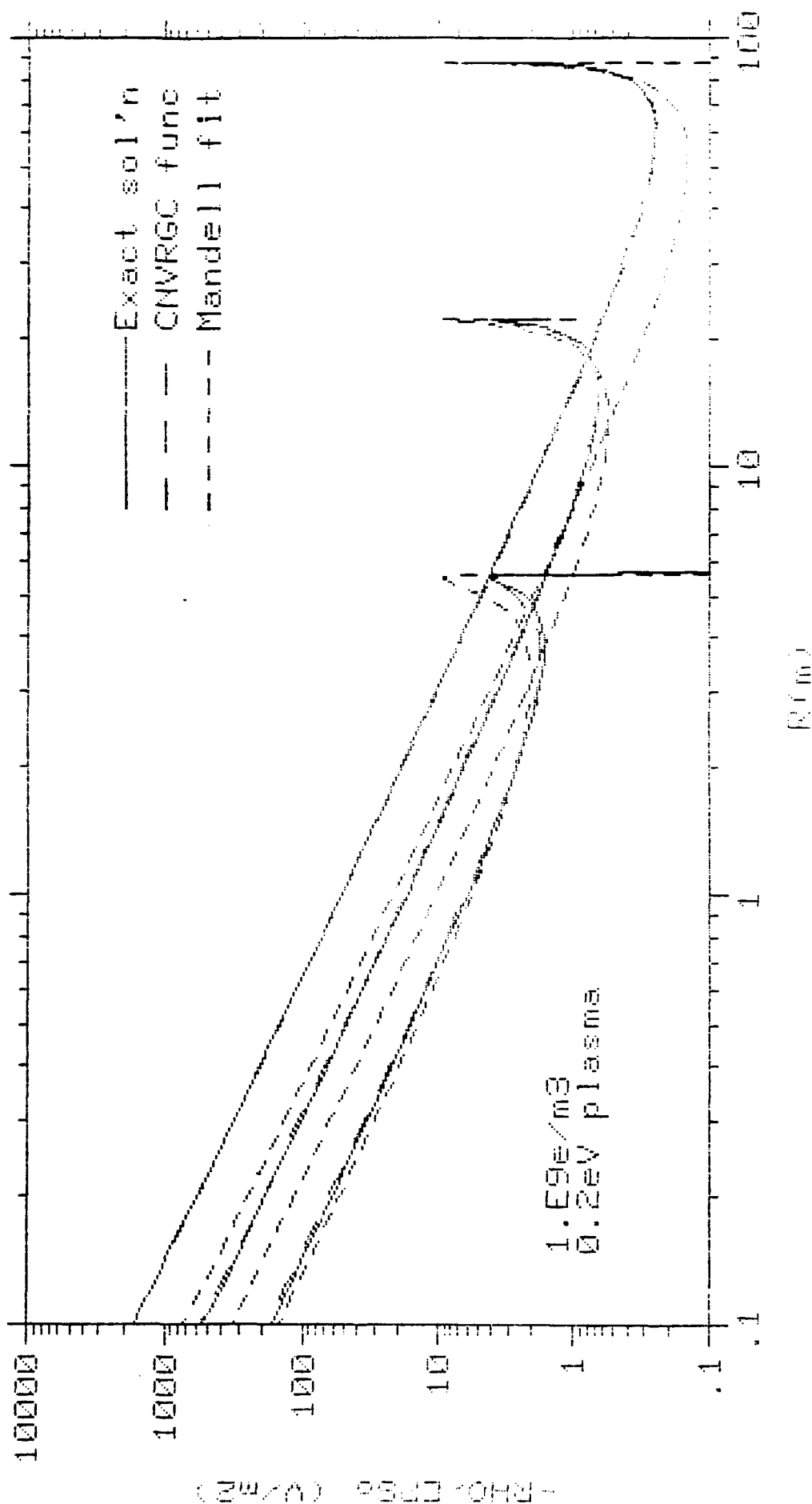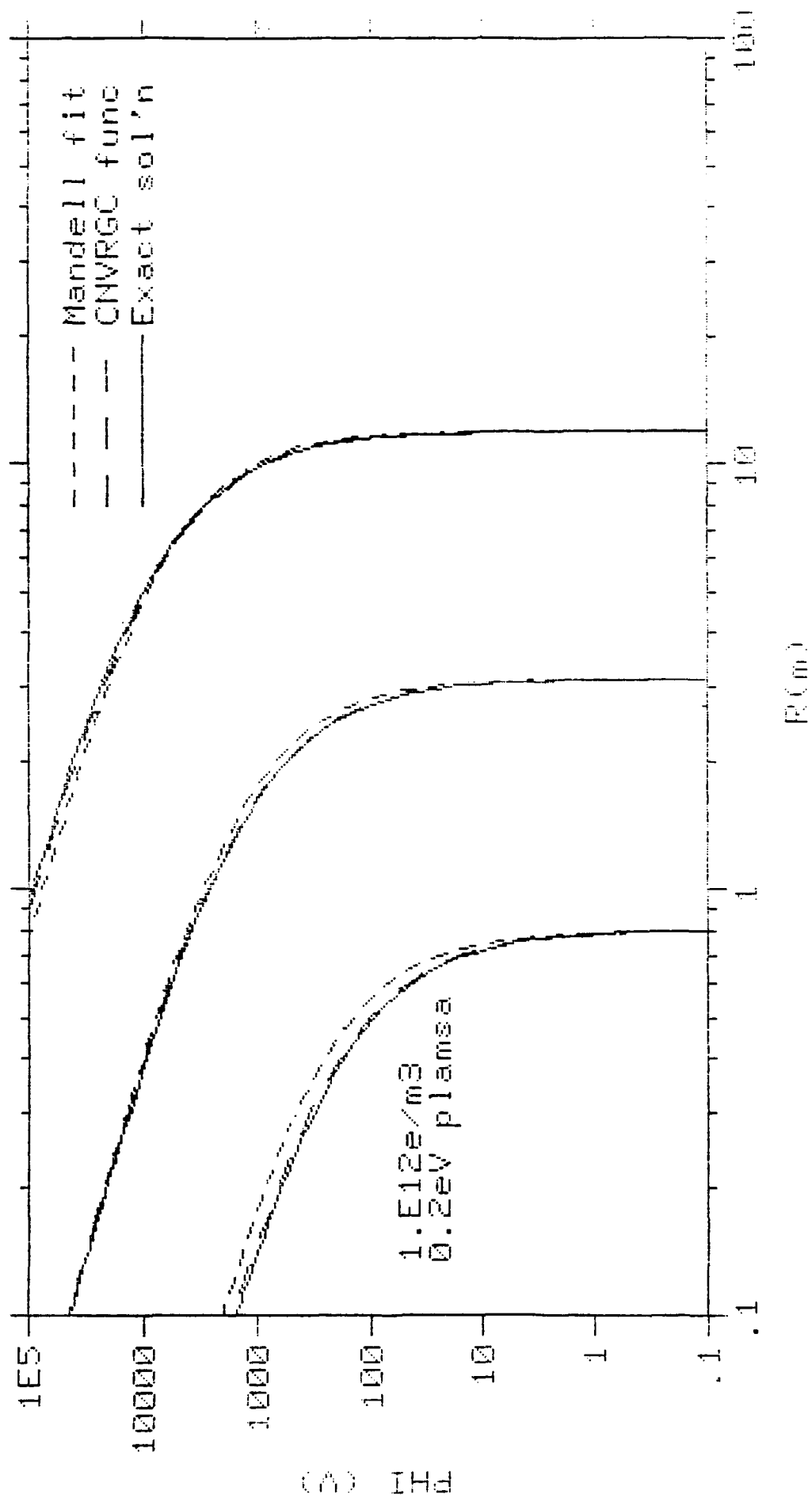
Figure 41. Space-charge profiles various sheath radii.
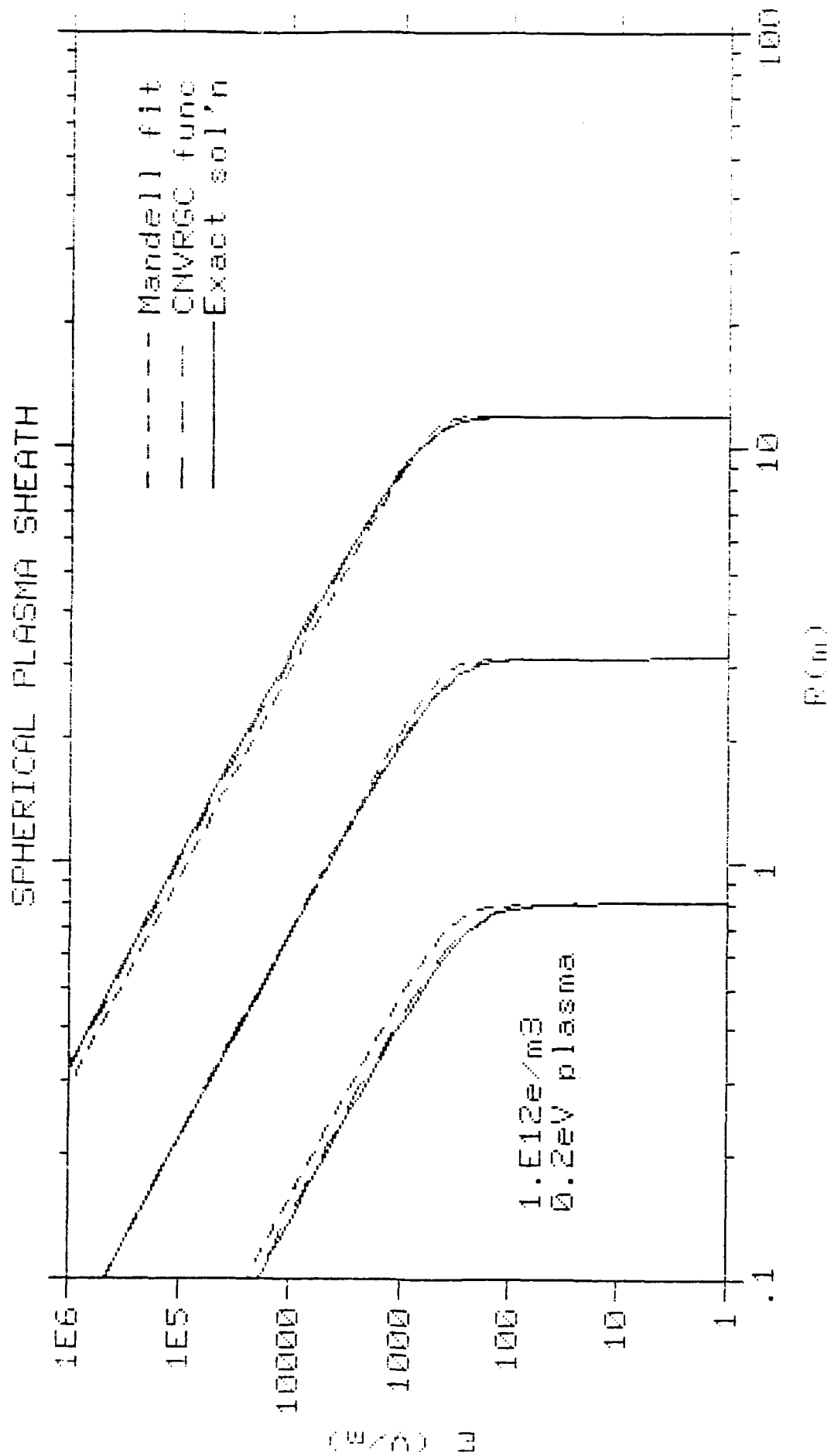
Figure 42. Potential profiles for various sheath radii.
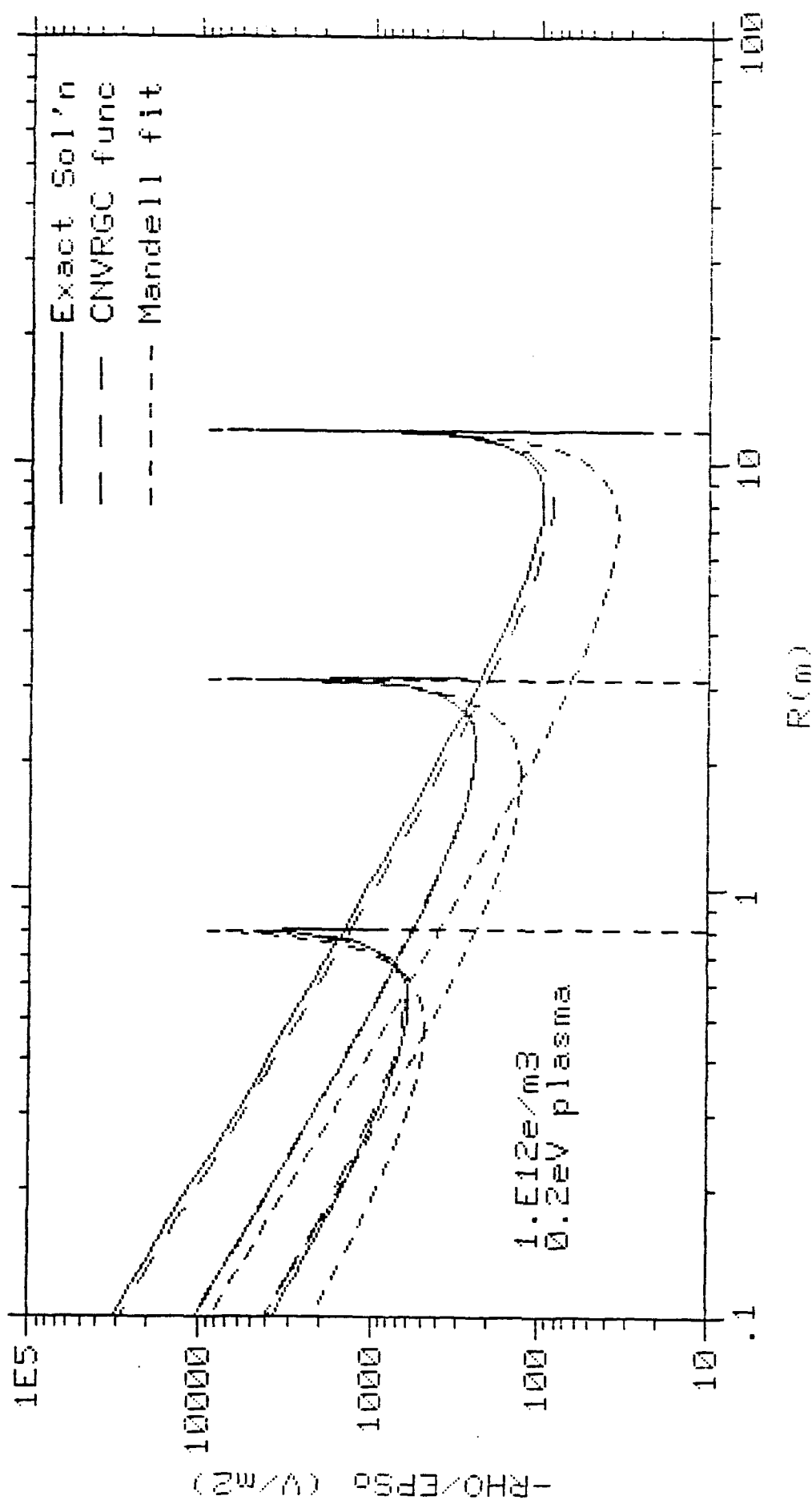
B-11

Figure 43. E-field profiles for various sheath radii.

Figure 44. Space-charge profiles for various sheath radii.

APPENDIX C

APPLICATION OF ELF2 TO SPEAR III PROBLEMS

C.1 PROBLEMS OF INTEREST.

Below we list SPEAR III design issues on which the Tetra electric field analysis capabilities can contribute, either within or as extensions of the ELF2 project.

C.1.1. The Umbrella Electrode.

The SPEAR I experiments flashed to the large vacuum test chamber walls during ground tests. The breakdown occurred at about +500V (no breakdown for negative polarity); the external circuit limited the current to about 10A. No such breakdown occurred in the actual space experiments. The best hypothesis so far is that trapped electrons had long enough paths (compared to mean free path between collisions) to produce avalanching in the thin neutral gas. If the ions colliding into the chamber walls sputter, say 10 electrons each, then the ionization mean free path need only exceed $1/10^{th}$ the average electron flight path length to get avalanching conditions.

The purpose of the umbrella electrode is to reproduce the effect of the ground test chamber walls in the SPEAR III experiment, which will use both polarities. Issues are as follows: 1) How big must the umbrella be? 2) What material should be used (considering secondary emission)? 3) What are the field distributions and what effect do they have? Outgassing can increase the ambient density by 2 to 3 orders of magnitude, as a function of position and time. Victoria Davis of Katz's group has done the outgassing contour computations.

C.1.2. Solar Array Experiments.

The first experiment uses traditional photovoltaic cells (as in the space station) near the cylindrical rocket body. The solar cells may be both folded and unfolded. The second experiment simulates a solar concentrator (SUPER, which is radiation hardened) and GaAs active elements. One concentration method is a

slot concept, using trough–like mirrors and cell assemblies. The other method uses a cassagranian geometry (lens, parabolic mirror, secondary, GaAs cells). The issue is finding the flashover thresholds, which will limit power production.

C.1.3. Passive Field Emission Structure(s).

There are four concepts under consideration to provide electrical contact with the plasma ground: a) A bi–polar hollow–cathode plasma contactor. b) Electron–emitting heated filaments. c) Attitude control produces N_2; Paschen minimum breakdown connects to plasma ground (NASA thinks this has happened to active satellites, where it has caused damage to electronics.) d) Passive discharge method, using sharp objects. (Field emission is a well understood mechanism.)

C.1.4. Placement of Diagnostics.

Field distributions will affect electron and ion trajectories. Where should the instrumentation be placed? How will they affect particle energy distributions? The instruments are mostly electrostatic analyzers.

Clearly, we can contribute in the analysis and calculation of electrostatic fields. Even vacuum solutions will be useful, since the space–charge effects are noticeable mostly near the sheath edge (meters away from the spacecraft surface). However, we would still need to couple in a particle–pushing code. (Ira Katz has offered to get us one, but we would have to work the interface.) The avalanche issue is fascinating physics, and we can make significant contributions given our kinetics work.

The following sections describe the physics of a viable approach to address the above four issues, the advantages of using the ELF codes, and the numerical techniques suitable for calculating the E–fields.

C.2 A LOW–IONIZATION, QUASI–COLLISIONLESS PLASMA SHEATH MODEL.

I. Katz, *et al*. (Ref. 1) suggest a first–order model which predicts breakdown of a low earth orbit sheath above a critical neutral density. Using average values of

electron and ion velocities and the ionization cross section, the model correctly predicts the approximate value of the critical neutral density ρ_c. We propose an improved model, based on the efficient, second–order accurate finite differences methods in boundary–fitted grids in our ELF codes, and an accurate treatment of the ionization process.

The ionization cross section is actually a function of electron energy $\mathcal{E} = e\phi$. At high energies, Eq. 3.3 of R. D. Evans (Ref. 2) gives an empirical fit for track length or mean range

$$R_m = 4.12 \text{ kg/m}^2 \; \mathcal{E}_{mev}^{(1.265 - .0954 \times \ln \mathcal{E}_{mev})} \qquad (C.1)$$

where $\mathcal{E}_{mev}$ is $\mathcal{E}$ in MeV. Notice at low energies the exponent is nearly constant. Differentiation gives the energy deposition rate, which is nearly constant per unit length. Assuming (Ref. 3) that 85 eV is lost per ionization (which virtually all collisions result in), the above formula implies an ionization cross section for a molecule the size of N_2 of $\sigma \approx 0.2 \times 10^{-16}$ cm^2 at 10 keV, which compares well with measured $\sigma = 0.13 \times 10^{-16}$ cm^2 (Ref. 4). We should expect the product σv_e to be proportional to $\mathcal{E}^{.265}$, so σ goes as $\mathcal{E}^{-.235}$. Of course, a more accurate analysis depends on chemical composition (Ref. 5).

Cross section data is available for N_2 and O_2 and many other chemical constituents of interest (Ref. 4). Of special interest are long–chain hydrocarbons, because they have low ionization potentials. They are likely to de–gas from organic compounds like pump oils and seals. If we can characterize the chemical composition of effluents de–gassing from a spacecraft, we can express the effective ionization cross section as a function of energy $\sigma(\mathcal{E})$. Thus, we can model the ionization source (e–ion pairs/cm^3/s) as:

$$S = N_n \; \sigma \; v_e \; N_e \qquad (C.2)$$

where N_n is the neutral number density, which may be a function of position and time.

The effect of the geomagnetic field may be argued to be negligible to first order

as follows. Although the magnetic turning will cause the average electron to dwell longer at a given position than if its path went straight to the collector, the first—order effect is to reduce the current; the space—charge profile ρ vs position remains nearly the same as calculated by ignoring the B—field. Thus, $N_e = \rho/e$ is unaffected by the geomagnetic field, and so also the ionization source term S.

Consider a positively biased spherical collector surrounded by a grounded concentric spherical umbrella electrode. As >10 keV ions bombard the umbrella electrode, they will generate 10 or more electrons per ion (Ref. 6). If we ignore edge effects, the problem is 1—dimensional. For a given material, the expected number of electrons per ion $F_u(\phi)$ and average electron energy $E_u(\phi)$ are functions of the ion energy, given by the potential at their point of birth $\phi(R)$. Thus, the plasma near the umbrella electrode will have an altered temperature

$$\theta' = 1.5 \, \frac{\int S(R) \, E_u(\phi) \, dR}{\int S(R) \, dR} \qquad (C.3)$$

and an altered density given by

$$\frac{\partial n_0'}{\partial t} = \int \left[\frac{R_u}{R}\right]^2 \, S(R) \, F_u(\phi) \, dR - n_0' \left[\frac{e/m}{4\pi \theta'}\right]^{.5} \qquad (C.4)$$

where the integrals are from the collector R_c to the umbrella R_u. The steady—state solution (if one exists) is

$$n_0' \approx \int \left[\frac{R_u}{R}\right]^2 \, S(R) \, F_u(\phi) \, dR \, / \, \left[\frac{e/m}{4\pi \theta'}\right]^{.5} \qquad (C.5)$$

If the average N_n is above critical, the sheath will be unstable, and no steady—state solution exists. If it is stable, a non—linear loop will be required to converge on the steady—state solution, starting from the sheath solution ignoring the ion contribution to ρ.

A time—dependent model can be built by integrating the ion equations of motion. Since the electrons are much faster, a quasi—steady—state treatment of the electron

C—4

sheath is acceptable. Thus, the ion source strength is known. Solution of the ion conservation and continuity equations will yield the time—dependent ion density. The space—charge is then

$$\rho = e \ (n_e - n_i) \qquad (C.6)$$

An analogous 2—D model is required to take into account the field enhancements at the edge of the umbrella electrode. That enhancement will concentrate the ion flow, which in turn will concentrate the return electron flow. Accuracy of the field calculations may be critical.

C.3 THE ELECTRIC FIELD (ELF) ANALYSIS CODES.

The ELF codes were originally developed as a tool to design field shaping electrodes for diffuse gas discharge devices. They are based on the generation of a boundary—fitted grid, on which the field continuity equations are transformed numerically. The transformed equations are then solved by second—order accurate finite difference methods, and the solution is transformed back to physical space. The result is high accuracy (<0.1% for modest grid sizes) with high speed (minutes interactive for a non—trivial geometry vacuum solution on a VAX 11—780—class machine). In contrast, finite—element codes typically require overnight batch operation on CRAY supercomputers, and still may produce -30% errors on conductor surfaces (Ref. 7).

We have been working on the development of the next—generation electric field (ELF2) analysis code under Contract DNA 001—89—C—0009. We have identified a feasible approach to solve Low Earth Orbit (LEO) plasma sheaths within ELF's boundary—fitted grid, finite—differences methods. In addition, the ELF field solving and plotting programs have been modified to handle cuts in the computational plane. This provides us with a powerful method to handle difficult geometries, especially those with highly re—entrant boundaries.

For example, a computational grid has been generated for the current—collecting sphere and first two voltage—grading bushing rings (SPEAR III). Figure 1 shows the sphere and bushing. It is apparent from this figure that part of the geometry is complex. Hence, standard grid generation methods would not apply. However,

these methods can be effective if the computational space is tailored to the geometry. Here, we have used the Thomas and Middlecoff method with some modification to the computational plane. Figure 2 presents computational and physical planes for this problem. The final form of the computational plane was among the five configurations which were tested. With this particular grid generation method, the boundary point distribution will determine the behavior of the interior grid lines. Sometimes additional control lines are necessary in the interior of the computational domain to improve the behavior of these grid lines. The dashed lines in computational space (Figure 2a) are control lines. These lines are essential in controlling the interior grid lines for this geometry, and without them the computed grid would fold. Figure 3 presents a grid (66×46) generated with this method, and Figure 4 shows an enlarged section of the grid around the bushing rings.

C.4 NUMERICAL METHODS FOR CALCULATION OF SPACE PROBE E–FIELD INCLUDING IONIZATION FROM BACKGROUND NEUTRALS.

It is now clear that the consistent solution of the sheath problem discussed above involves two numerical aspects: the Stefan problem, and a "particle pusher" code.

C.4.1. Stefan Problem.

The consistent solution of the sheath problem is a multidimensional Stefan problem, i.e. a boundary value problem in which the position of one boundary is not known. In a typical two–point boundary value problem in 1–D, one solves a second order elliptic equation for potential V over a specified domain $0 \leq x \leq L$, with L specified, and with boundary conditions

$$V(O) = V_o, \quad V(L) = V_1 \quad \underline{or} \quad dV/dx|_L = G_1. \qquad (C.7)$$

In a Stefan type of problem, one typically solves the fields with boundary conditions of

$$V(O) = V_o, \quad V(L) = V_1 \quad \underline{and} \quad dV/dx|_L = G_1, \qquad (C.8)$$

where one does not know in advance the position of the right boundary L. Note

that if L were known, (2) would over—specify the problem.

For a linear 1—D problem, L may be solved directly. For the nonlinear problem of present interest, L can only be solved iteratively. Also, the plasma sheath problem is 2—D or 3—D, so the analog of the 1—D variable L is now an outer boundary line (in 2—D) or surface (in 3—D).

The problem is made easier because we expect the sheath edge to appear far enough from the probe that the details of the probe geometry will be obscured; i.e., the sheath boundary is approaching a spherical shape. We will not have to assume a spherical shape, but we will be able to drive the iterations for the outer boundary by considering coordinate stretching in r only; i.e., we will solve iteratively for $L(\theta)$ using 1—D Newton—Raphson iteration in each $L(\theta)$ separately, with the θ effect lagged in the iteration (Picard iteration). Likewise, the essential nonlinear character of the solution is 1—D, and the details of the nonlinear iteration method will be developed and proven in 1—D. The Langmuir—Blodgett 1—D solutions for spherical symmetry would be reproduced from first principles.

The problem formulation will be a type of invariant embedding, in which the equations are transformed via a coordinate stretching with an undetermined stretching parameter; i.e., the radial coordinate r in physical space is transformed to R in logical space by $R = r/L(\theta)$ where $L(\theta)$ is unknown and is solved by a quasi—1—D Newton—Raphson iteration. The Dirichlet boundary conditions

$$V(0) = V_o, \quad V(L) = V_1 \qquad (C.9)$$

will be applied directly in every nonlinear iteration, and the error term

$$ERR = dV/dx|_L - G_1 \qquad (C.10)$$

will drive the nonlinear iteration correction.

In order to achieve convergence, it generally will be required that the initial guess be good enough to be within the neighborhood of monotonic behavior of the solution. Experience with the 1—D solution will be important to assure this. Given this reasonable initial guess, experience with similar nonlinear problems

C—7

suggests that 5–10 nonlinear iterations, each involving a solution of the linearized elliptic boundary value problem, will be sufficient for unequivocal convergence. The 3–D problem is not expected to be any more difficult than the 2–D or 1–D problems as far as this nonlinear iteration is concerned. the primary difference being in the operation count for the inner (linear) problem. We propose to use a semicoarsening multigrid method, which is very efficient for high resolution problems, for the inner (linear) solver (about one order of magnitude faster than SOR methods for 100×100–sized grids).

C.4.2. Particle Pusher Code.

In order to self–consistently calculate the ionization effect of the background neutrals, we assume that the electrons are at a steady state, but that the more massive ions are treated as transient particles moved in a self–consistent E–field by a particle pusher code. This procedure again involves a nonlinear iteration. However, our experience on similar problems suggests that an outer (nonlinear) Picard iteration will be adequate, and much cheaper than a multi–dimensional Newton–Raphson iteration, both in computer time and in development time.

The particles are accelerated according to Newton's law $F = ma$, wherein the force F is directly proportional to the particle charge and to the local electric field. Since the particle positions will be described in a stretched (non–orthogonal) 2–D or 3–D non–orthogonal coordinate system, one must be able to accurately interpolate the E–field in the 2–D or 3–D non–orthogonal grid, and to move the particles accurately in an unsteady force field.

Our subcontractor, Ecodynamics, has already developed massless particle tracker codes in general non–orthogonal 2–D and 3–D coordinates (for tracing of radioactive particles in unsteady fluid flows). The codes have been verified to be fully second order accurate in space and fifth order accurate in time. Some development is still required to convert this to a massive particle tracker.

C.5 RELATIONSHIP TO SPEAR III NEEDS.

The application of the proposed model to the umbrella electrode is clear. The modified ELF2 code will provide accurate, detailed, 2–D field distributions near the

edge of the umbrella electrode, self—consistently computing the ion currents and densities. Different electrode materials can be tried by using their electron yield parameters.

The breakdown of solar arrays has been adequately modeled by I. Katz, *et al*. (Ref. 1) in terms of the field stress at the surface E_0. The modified 3—D ELF2 codes could provide accurate E_0 values for various geometries relative to the rocket body and plasma ground. (It is doubtful that 2—D analyses will be adequate if the array is deployed in the traditional position beside the main cylindrical body.) We expect the modified ELF2 codes to maintain a significant speed advantage over finite element codes while improving accuracy, especially at computational boundaries.

The field distributions in the plasma contactor sheaths will probably be affected by the physics of the background neutral ionization for all proposed mechanisms. 2—D analyses may suffice if the contactors are deployed near the rocket body axis, as in SPEAR I. More accurate field calculations will provide confidence in performance predictions for the various concepts under consideration, especially passive field emission.

Finally, the combination of accurate field distributions and self—consistent ion trajectories will provide guidance for placement of electro—static charged particle analyzers and other plasma diagnostics, in addition to aiding in data analysis.
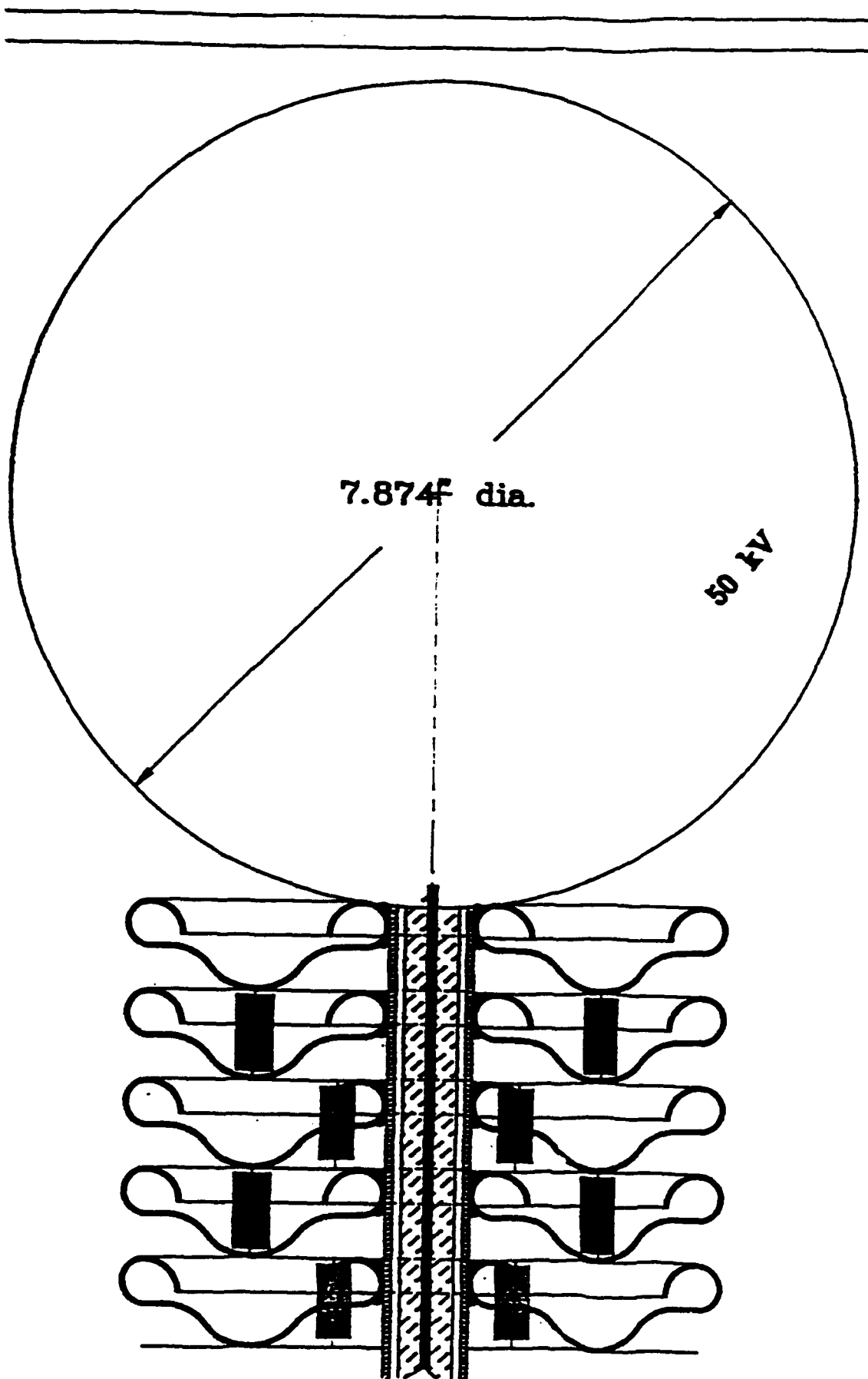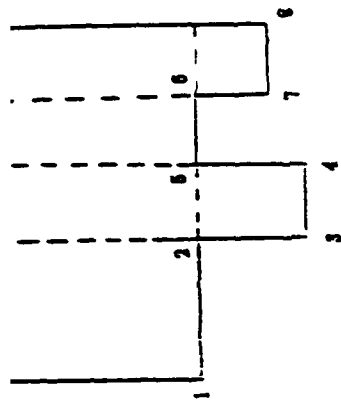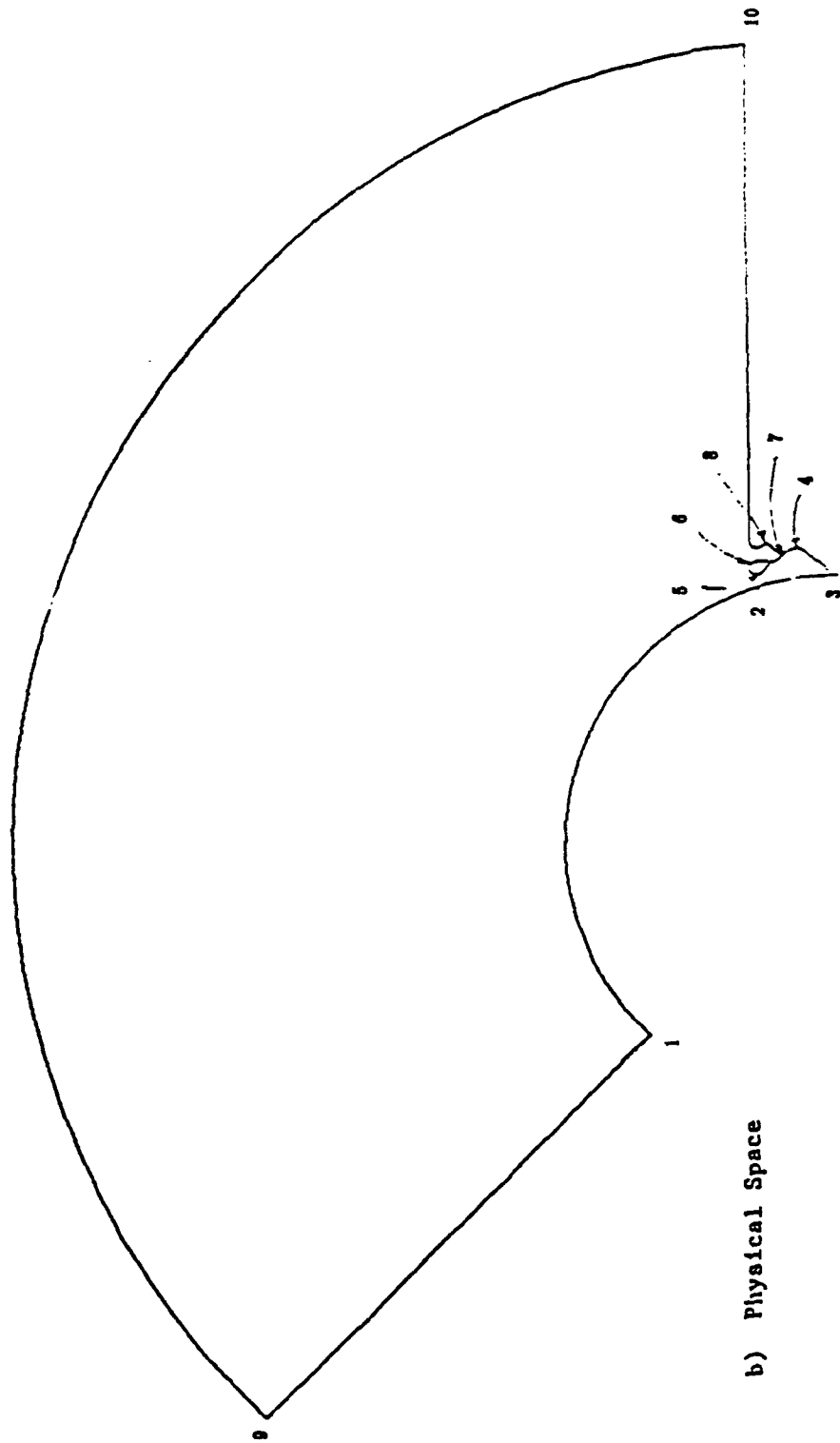
7.874" dia.

50 kV

Figure 45. SPEAR current collector.

a) Computational Space

b) Physical Space

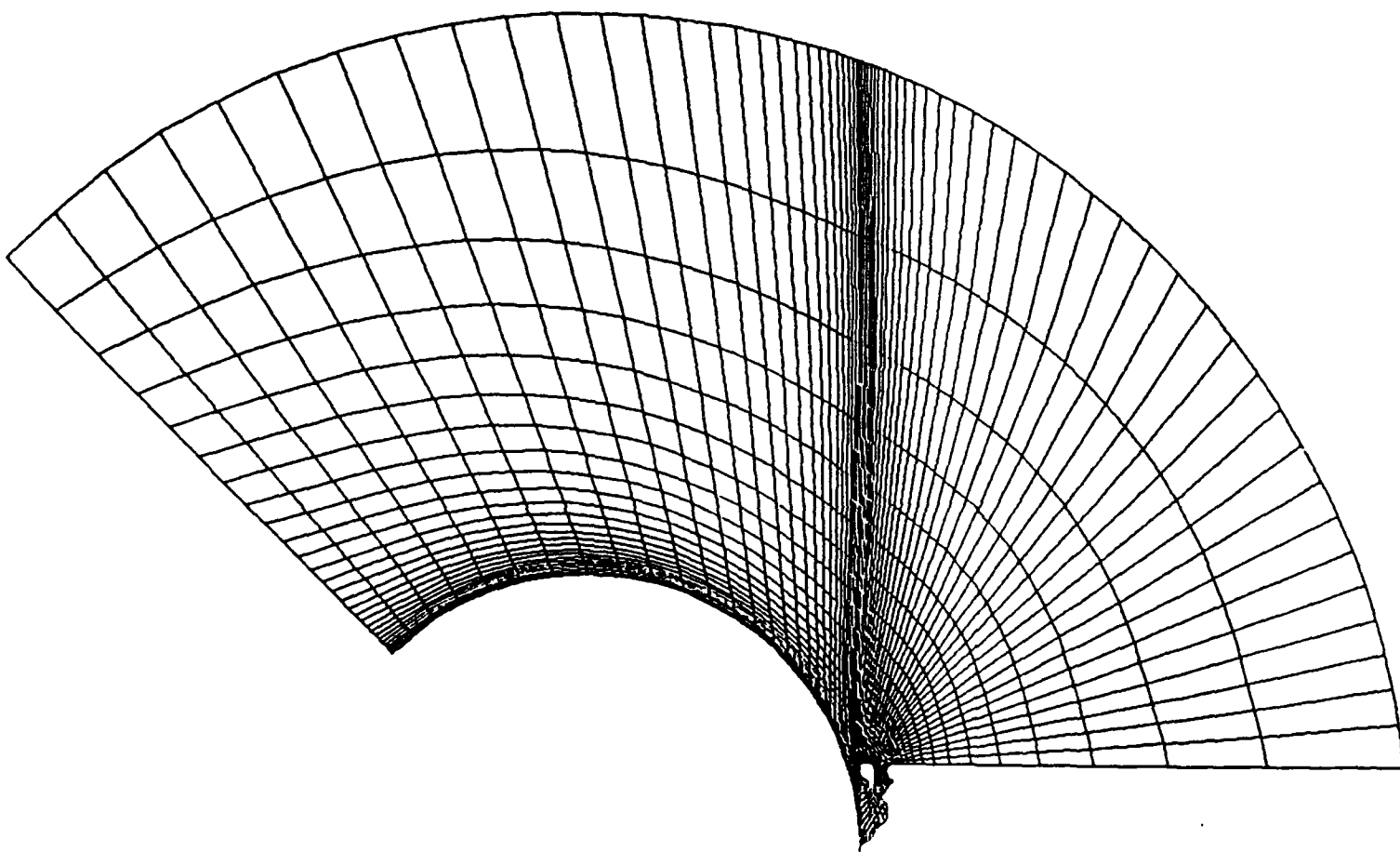Figure 46. Schematic mapping of physical space onto computational space.
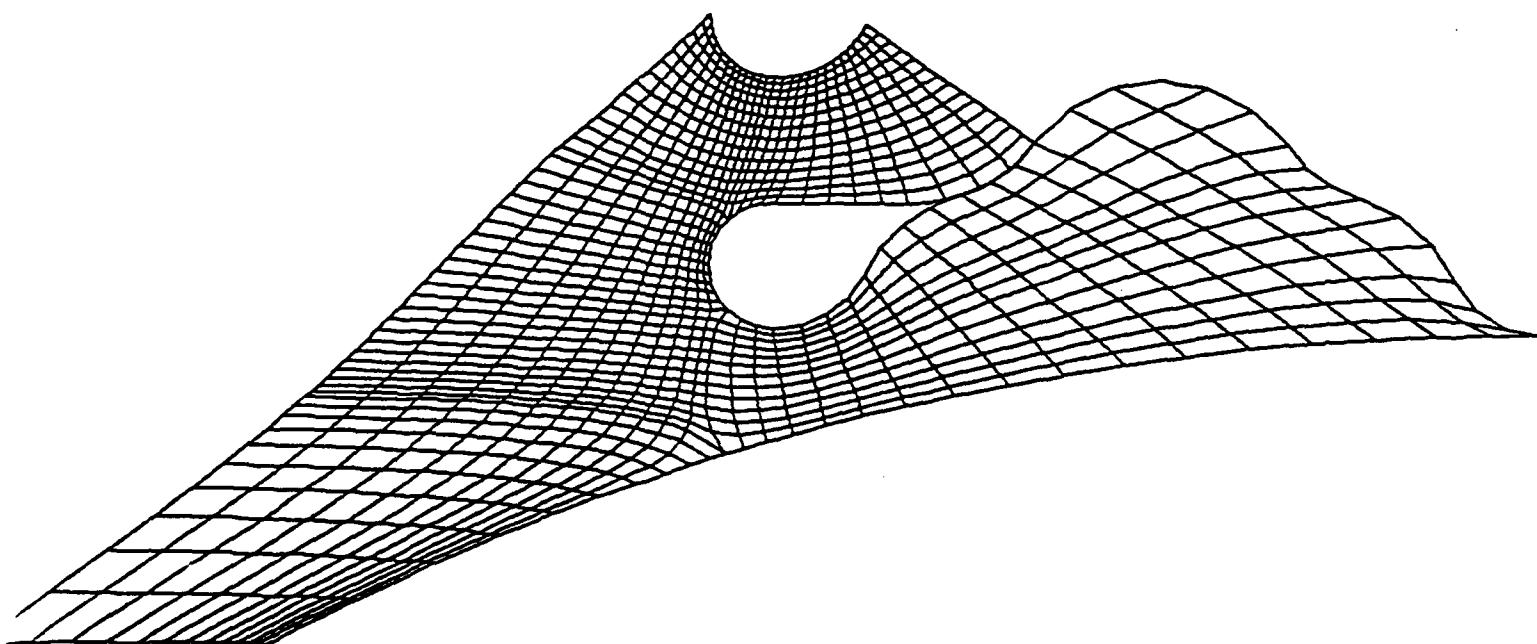
Figure 47. Computational grid.

Figure 48. Enlarged section of figure 47.

APPENDIX D

ELEMENTARY SHAPES FOR BUILDING GEOMETRIES

The instructions–driven input technique relies on four elements or "tools". This appendix describes in detail what each does and how to use it. For each, we define the input parameters required, and the effect, including the effect on node spacing, since that can be important for control lines.

All options require definition of the grid segment in the form:

$$I(or\ J) = \#fix, other = \#\ to\ \# \qquad (D.1)$$

That is, one index (I or J) must be fixed, and the other must have a range. These specifications may be given as fractions of the logical space unit square, rather than index integer number. This option facilitates changing the grid array dimensions without changing the instructions file, but care must be exercised to insure that the instructions make sense regardless of number of nodes. The purpose of the tools is to calculate the coordinates of each node in the specified range.

LOCATE allows the user to specify each node location individually. (It makes little sense to use relative range limits with this option.)

STRGHT creates a straight line. The input parameters are the end–point coordinates Xfm, Yfm and Xto,Yto. The nodes are equally spaced. (Notice this makes STRGHT useless to define a control line, since the purpose of a control line is to pull grid lines toward some region at the expense of others.) The length units are arbitrary, but must be the same for X and Y, and must be compatible with other calculations throughout the ELF run.

ELIPSE makes a segment of an ellipse. Input parameters are the ellipse origin Xo, Yo, horizontal/vertical radii Xr, Yr and angle limits FM, TO. (Subroutine ELIPSE uses radians, but the instruction–driven input code translates from degrees for the user's convenience.) Points are equi–distributed in angle on a unit square, which is then stretched to the actual aspect ratio Xr/Yr. Notice this means

angles are not physical angle, unless Xr = Yr. For example, 45° is the point where $\Delta X = Xr/\sqrt{2}$ and $\Delta Y = Yr/\sqrt{2}$; if Yr << Xr, that point is close to a physical angle of 90°.

SELIPS makes a segment of a superellipse. Input parameters are the same as for ELIPSE with one addition: The power of the superellipse PWR. A superellipse is defined by the relationship

$$
\left[\frac{\Delta X}{Xr} \right]^{PWR} + \left[\frac{\Delta Y}{Yr} \right]^{PWR} = 1 \qquad (D.2)
$$

Notice if PWR = 2.0, you get a regular ellipse. PWR = 1.0 gives a straight diagonal line for each quadrant. As PWR → ∞, the superellipse tends toward a square corner in each quadrant. For both ELIPSE and SELIPS options, the user is responsible to insure that the end—points come out where he needs them.

QADRNT makes a quadrant of a superellipse, and distorts it as needed to fit a parallelogram defined by three points. The input parameters are the three points' coordinates Xfm, Yfm, Xc, Yc and Xto, Yto, and the superellipse power PWR. The unit square point (1,0) maps to (Xfm, Yfm), (1,1) maps to (Xc, Yc) and (0,1) maps to (Xto, Yto). In essence, QADRNT "rounds off" a sharp corner of arbitrary angle, orientation and aspect. This gives the user positive control over end—point positions and tangent directions, facilitating smooth "butts" between segments. Another possible use is to create control lines, since placing the corner Xc, Yc nearer one end insures half the points will be on that leg. (The corner Xc, Yc may be in a straight line between Xfm, Yfm and Xto, Yto.)

These shape elements are not exhaustive. Many other analytical classes may be useful, much as the Rogowski electrode shape. The user may always modify the Fortran coding to create a geometry for a specific need. However, these elementary shapes have been adequate for most geometries, and represent greater flexibility than any CAD program we are aware of (which cannot generate superellipses).

The user should be cautioned to allow ample time to sketch out the geometrical concept and debug his instructions file set. A working level of competence in analytical geometry is a user prerequisite regardless of input technique.

APPENDIX E
BIBLIOGRAPHY

Janni, J. F., R. Berry, J. Burgio, G. Cable, R. Conley, H. Happ, D. Janni, L. Lutz, H. Murphy, N. Philliber, G. Radke, and J. Spear, *FORTRAN-77 Computer Program Structure and Internal Documentation Standards for Scientific Applications*, AFWL-TR-85-26, June 1986.

Reiman, K. U., "The Technological Potential of Plasma Physics", 1987 IEEE International Conference on Plasma Science, Arlington, VA, June 1-3, 1987.

Allshouse, R., and J. Glicken, "A Marketing Plan for Tetra Corporation's tetraELF", Allshouse & Glicken, Inc., Marketing Services, 10 June 1987.

American National Standard Programming Language FORTRAN, ANSI x3.9-1978, April 1978.

Steinberg, S. and P. J. Roache, "Symbolic Manipulation of Computational Fluid Dynamics," **Jour. Computational Physics**, Vol. 57, No. 2, January 1985, pp. 251-284.

Steppel, S., T. L. Clark, P. C. Belford, W.D. Bumgarner, A. M. Federoff, N. S. Frankle, J.A. Torrule, and J. A. Zuccaro, *Digital System Development Methodology (DSDM^{TM}) Version 2.0*, Computer Sciences Corporation, March 1984.

Roach, P. J., S. Steinberg, and W. M. Moeny, "Interactive Electric Field Calculations for Lasers," AIAA 17th Fluid Dynamics, Plasma Dynamics, and Lasers Conference, Snowmass, Colorado, June 25-27, 1984.

Roache, P. J., H. J. Happ, and W. M. Moeny, "Unsteady 2D Electric Field Modeling With High Accuracy on Conductor Surfaces," 4th IEEE Pulsed Power Conference, Albuquerque, New Mexico, 1983.

Roache, P. J., S. Steinberg, J. H. Happ, and W. M. Moeny, "3D Electric Field Solutions in Boundary-Fitted Coordinates," 4th IEEE Pulsed Power Conference, Albuquerque, New Mexico, 1983.

Happ, H. J. and W. M. Moeny, "Development and Accuracy Testing of the 2D Steady-State NLPBF E-field Code," Tetra Technical Note, February, 1983.

Roache, P. J. and S. Steinberg, "Symbolic Manipulation and Computational Fluid Dynamics," **AIAA Journal**, Vol. 22, October 1984, pp. 1390-1394. Also, AIAA Paper No. 83-1952.

Roache, P. J., "The ELF codes: Electrode Design for Lasers and Switches," Invited Paper, **Proc. CTAC-85 Conference**, Melbourne, Australia, August 25-28, 1985.

Moeny, W. M., M. von Dadelszen and P. J. Roache, *The ELF Electric Field Analysis Computer Codes, Vol. 1. Code Description and Specific Applications.* **Tetra TR–85–016**, Tetra Corporation, Albuquerque, New Mexico, August 1985.

Roache, J. P., Moeny, W. M. and M. von Dadelszen, *The ELF Electric Field Analysis Computer Codes, Vol. 2, Users Manual,* **Tetra TR–85–016**, Tetra Corporation, Albuquerque, New Mexico, August 1985.

DISTRIBUTION LIST

DNA-TR-91-145

DEPARTMENT OF DEFENSE

DEFENSE INTELLIGENCE AGENCY
    ATTN: DB-6

DEFENSE NUCLEAR AGENCY
  2 CYS ATTN: TITL

DEFENSE TECHNICAL INFORMATION CENTER
  2 CYS ATTN: DTIC/FDAB

DEPARTMENT OF THE ARMY

ELECTRONICS TECH & DEVICES LAB
    ATTN: PULSE POWER CTR H RHINEHART
    ATTN: SLCET-D C THORNTON

HARRY DIAMOND LABORATORIES
    ATTN: F AGEE
    ATTN: SLCHD-NW-HPM S GRAYBILL
    ATTN: SLCHD-NW-RS G KERRIS
    ATTN: SLCHD-NW-RS G HUTTLIN
    ATTN: SLCHD-NW-RS M BUSHELL

DEPARTMENT OF THE NAVY

NAVAL POSTGRADUATE SCHOOL
    ATTN: CODE 61SW F SCHWIRZKE

NAVAL RESEARCH LABORATORY
    ATTN: CODE 4700 S OSSAKOW
    ATTN: CODE 4720 J DAVIS
    ATTN: CODE 4770 G COOPERSTEIN
    ATTN: CODE 4770 R COMMISSO

NAVAL STUDIES BOARD
    ATTN: CAPT J WILSON USN RET

NAVAL SURFACE WARFARE CENTER
    ATTN: V L KENYON H23

NAVAL SURFACE WARFARE CENTER
    ATTN: CODE F-12

DEPARTMENT OF THE AIR FORCE

AIR FORCE OFFICE OF SCIENTIFIC RSCH
    ATTN: DR. R. BARKER

AIR WEATHER SERVICE, MAC
    ATTN: AWS TECH LIBRARY

PHILLIPS LABORATORY, WEAPONS DIVISION
    ATTN: AWP J DEGNAN
    ATTN: LIBRARY
    ATTN: WL/AWP WILLIAM L BAKER

DEPARTMENT OF ENERGY

LOS ALAMOS NATIONAL LABORATORY
    ATTN: J BROWNELL
    ATTN: I LINDEMUTH
    ATTN: CHARLES FENSTERMACHER
    ATTN: R REINOVSKY

SANDIA NATIONAL LABORATORIES
    ATTN: DIV 2566 J HARRIS
    ATTN: DIV 9341 J LEE
    ATTN: M BUTTRAM DIV 1248
    ATTN: ORG 9300 J E POWELL
    ATTN: ORG 9340 W BEEZHOLD

OTHER GOVERNMENT

CENTRAL INTELLIGENCE AGENCY
    ATTN: OSWR J PINA

NASA
    ATTN: J LEE

NATIONAL INSTITUTE OF STANDARDS & TECHNOLOGY
    ATTN: R HEBNER

DEPARTMENT OF DEFENSE CONTRACTORS

APPLIED PHYSICAL ELECTRONICS RESEARCH CENTER
    ATTN: DR W NUNNALLY

BERKELEY RSCH ASSOCIATES, INC
    ATTN: R KARES
    ATTN: S BRECHT

BERKELEY RSCH ASSOCIATES, INC
    ATTN: N PEREIRA

ENERGY COMPRESSION RESEARCH CORP
    ATTN: D S WEIN

FORD MOTOR COMPANY CORPORATION
    ATTN: M MOSBROOKER

FORD MOTOR COMPANY CORPORATION
    ATTN: C NAKAYAMA

GA TECHNOLOGIES, INC
    ATTN: DOCUMENT CONTROL

JAYCOR
    ATTN: B SEIDLER

KAMAN SCIENCES CORP
    ATTN: D MOFFETT
    ATTN: DASIAC

KAMAN SCIENCES CORPORATION
    ATTN: DASIAC

LTV AEROSPACE & DEFENSE COMPANY
    ATTN: LIBRARY EM-08

MAXWELL LABS, INC
    ATTN: J SEVIGNY
    ATTN: K WARE
    ATTN: W RIX

MISSION RESEARCH CORP
    ATTN: B GOPLEN

PHYSICS INTERNATIONAL CO
    ATTN: C STALLINGS
    ATTN: P SINCERNY

PULSE SCIENCES, INC
     ATTN: P W SPENCE

R & D ASSOCIATES
     ATTN: I VITKOVITSKY

TETRA CORP
 2 CYS ATTN: A E RODRIGUEZ
 2 CYS ATTN: K J TOURYAN
 2 CYS ATTN: K SALARI
 2 CYS ATTN: P J ROACHE
     ATTN: W MOOENY

TEXAS TECH UNIVERSITY
     ATTN: DR M KRISTIANSEN

UNIVERSAL VOLTRONICS CORP
     ATTN: W CREWSON

W J SCHAFER ASSOCIATES, INC
     ATTN: E ALCARAZ

WESTINGHOUSE ELECTRIC CORP
     ATTN: J S FLETCHER

WESTINGHOUSE STC
     ATTN: DR A H COOKSON

3M CENTER
     ATTN: D REDMOND
     ATTN: E HAMPL

DIRECTORY OF OTHER

AUBURN UNIVERSITY
     ATTN: M ROSE

UN IVERSITY OF NEW YORK-BUFFALO
     ATTN: R DOLLINGER

UNIVERSITY OF CALIFORNIA-DAVIS
     ATTN: J S DEGROOT